UNIVERSIDAD DE CHILE
FACULTAD DE CIENCIAS FÍSICAS Y MATEMÁTICAS
DEPARTAMENTO DE ASTRONOMÍA

ACTIVE GALACTIC NUCLEI IN THE ZWICKY TRANSIENT FACILITY

STUDYING THE VARIABILITY OF QUASARS AS A FUNCTION OF REST-FRAME WAVELENGTH

TESIS PARA OPTAR AL GRADO DE
DOCTORA EN CIENCIAS, MENCIÓN ASTRONOMÍA

PRIYANJALI PATEL

PROFESORA GUíA:
PAULINA LIRA TEILLERY
PROFESORA CO-GUíA:
PATRICIA ARÉVALO NOORDAM

MIEMBROS DE LA COMISIÓN:
RENÉ MÉNDEZ BUSSARD
WALTER MAX-MOERBECK ASTUDILLO
MOUYUAN SUN

Este trabajo ha sido parcialmente financiado por ANID Beca Doctorado Nacional-2022 21222298 Chile.

SANTIAGO DE CHILE
2024

RESUMEN DE LA TESIS PARA OPTAR
AL GRADO DE DOCTORA EN CIENCIAS, MENCIÓN ASTRONOMÍA
POR: PRIYANJALI PATEL
FECHA: 2024
PROF. GUÍA: PAULINA LIRA TEILLERY

NÚCLEOS GALÁCTICOS ACTIVOS EN EL ZWICKY TRANSIENT FACILITY

Las luminosidades de un cuásar, junto con las de otros Núcleos Activos de Galaxias (AGNs), muestran fluctuaciones en su brillo a través de un amplio espectro, desde rayos X a frecuencias de radio, y en diversas escalas de tiempo, en un rango de unas horas a varios años. Por lo general, los cuásares cambian su emisión óptica y UV proveniente del disco de acreción en alrededor de 10%-20% a lo largo de periodos que van desde varios meses a años. Aunque la exploración de la variabilidad ha sido crucial para la comprensión del centro compacto de los AGNs, la causa de estas fluctuaciones es incierta. El propósito principal de investigaciones previas ha sido la caracterización de los cambios de luminosidad de los cuásares e indagar acerca de su relación con propiedades fundamentales, tales como la masa de agujero negro, la tasa de acreción en relación al límite de Eddington y la longitud de onda en reposo (rest-frame). Sin embargo, la falta de muestras lo suficientemente grandes para obtener resultados estadísticamente robustos no ha permitido encontrar respuestas coherentes. Modelos estadísticos populares, tales como el Camino Aleatorio (o Damped Random Walk, DRW) han demostrado ser insuficientes para describir las características emergentes de la variabilidad observada, enfatizando la necesidad de modelos más complejos. Gracias al nuevo énfasis en el estudio temporal de fuentes astrofísicas, finalmente se ha vuelto posible determinar la dependencia de estos modelos de parámetros físicos, tales como la masa de agujero negro, tasas de acreción y longitud de onda.

Abordar la brecha de estudios anteriores requiere un análisis robusto en diferentes escalas de tiempo y una evaluación rigurosa de los modelos teóricos con grandes conjuntos de datos. Solo de esta manera profundizaremos nuestra comprensión de la variabilidad de los AGNs y los mecanismos subyacentes. Esta tesis contribuye a esta exploración con el análisis de la variabilidad de los AGNs encontrados con el Zwicky Transient Facility (ZTF, Masci et al. 2019), y se enfoca en cómo esta depende de la longitud de onda en reposo (restframe wavelength).

El Capítulo 2 presenta técnicas y enfoques para examinar la variabilidad de los AGNs, centrándose específicamente en las dificultades causadas por muestreos irregulares, ruido estadístico y la naturaleza estocástica de las curvas de luz óptica de los AGN. Este capítulo explora métodos para la extracción de información esencial desde una serie temporal de AGNs, usando el Filtro de Sombrero Mexicano para calcular desviación y generando curvas de luz sintéticas. Estos enfoques son la base para los análisis de los capítulos siguientes.

El Capítulo 3 explora la diferencia entre la variabilidad de los AGNs y longitud de onda en reposo usando la base de datos de la Zwicky Transient Facility. Este análisis examina curvas de luz de las bandas g y r de casi 5.000 cuásares, revelando una marcada relación inversa entre la varianza y la longitud de onda en reposo, la cual es más pronunciada en escalas de tiempo más cortas. Al introducir un análisis espectral incluimos no solo la contribución de la emisión de continuo a nuestras estimaciones de la varianza, pero también del pseudo-continuo de Balmer y Fe II y líneas de emisión.

El Capítulo 4 se centra en la aplicación del modelo CHAR (Corona-Heated Accretion Disk) para interpretar la relación varianza–longitud de onda observada. A través de la comparación de datos empíricos con las predicciones del modelo CHAR, evaluamos la capacidad del modelo para replicar el espectro de varianza en diferentes escalas de tiempo. Este estudio comparativo demuestra que el modelo CHAR se acerca en gran medida a los patrones observados, particularmente en la predicción de cómo la varianza varía junto con la longitud de onda. Este capítulo destaca el potencial del modelo CHAR para explicar las variaciones de temperatura dentro del disco de acreción.

RESUMEN DE LA TESIS PARA OPTAR
AL GRADO DE DOCTORA EN CIENCIAS, MENCIÓN ASTRONOMÍA
POR: PRIYANJALI PATEL
FECHA: 2024
PROF. GUÍA: PAULINA LIRA TEILLERY

ACTIVE GALACTIC NUCLEI IN THE ZWICKY TRANSIENT FACILITY

Quasar luminosities, along with those of other Active Galactic Nuclei (AGNs), show brightness fluctuations across a broad spectrum, from X-ray to radio frequencies, and over diverse time scales, ranging from a few hours to multiple years. Typically, quasars change in their UV-optical continuum emission from the accretion disk by about 10%-20% over periods spanning from several months to years. While exploring variability has proven crucial for understanding the compact core in AGNs, the precise cause of these fluctuations remains uncertain. Prior research largely aimed to characterize changes in quasar luminosity and look for its link to fundamental properties, including black hole mass, the rate of accretion relative to the Eddington limit, and the rest-frame wavelength. However, the lack of samples large enough to obtain statistically robust results had prevented in the past the finding of full and coherent answers. Popular existing statistical model descriptions, such as the Damped Random Walk (DRW), are now shown to fall short of fully describing the emerging characteristics of the observed variability, underscoring the need for more complex models. Besides, determining the dependency of these models on physical parameters such as black hole mass, accretion rates and wavelength is finally becoming possible thanks to the advent of a time-domain approach to the study of sources.

Addressing the gaps of previous studies requires a robust analysis across different timescales and rigorously testing theoretical models against large datasets. Only in this way we will deepen our understanding of AGN variability and the underlying mechanisms. In this thesis, I contribute to this exploration with the analysis of variability for AGN found in the Zwicky Transient Facility (ZTF, Masci et al. 2019), focusing on how it depends on rest-frame wavelength.

In Chapter 2, I present techniques and approaches for examining AGN variability, specifically focusing on the difficulties caused by irregular sampling, noise, and the stochastic nature of AGN optical light curves. The chapter explores methods for extracting essential information from AGN time series, using the Mexican Hat filter method to calculate variance, and generating synthetic light curves. These approaches serve as the foundation for the analyses in the following chapters.

In the Chapter 3, we explore the relationship between AGN variability and rest-frame wavelength using the Zwicky Transient Facility data set. This analysis examines light curves from the g and r bands of nearly 5000 quasars, revealing a pronounced inverse relationship between variance and rest-frame wavelength, an effect that becomes more pronounced at shorter timescales. By introducing a spectral analysis we include not only the contribution of the continuum emission to our variance estimations but also Balmer and Fe II pseudo-continuum, and emission lines.

In the Chapter 4, we focus on the application of the Corona-heated Accretion-disk (CHAR) model to interpret the observed variance-wavelength relationship of AGNs. By comparing the empirical data with predictions from the CHAR model, we assess the model capacity to replicate the variance spectrum across different timescales. This comparative study demonstrates that the CHAR model closely matches the observed patterns, particularly in predicting how variance changes with wavelength. This chapter underscores the potential of the CHAR model in explaining temperature variations within the accretion disk.

It is important not to worship what is known, but to question it. — Jacob Bronowski

Acknowledgements

I would like to thank Prof. Paulina for her support, guidance, and invaluable advice throughout these years. Her mentorship has been instrumental in shaping my academic journey and refining my research approach. A big thank you to Prof. Patricia for her expertise and exceptional supervision. Her insightful feedback and support have been crucial in refining my thesis and advancing in my research. I am deeply thankful to the members of my thesis committee Prof. René A. Méndez, Prof. Walter Max-Moerbeck, and Prof. Mouyuan Sun, for their critical feedback and support during the course of my PhD. I am also grateful to Prof. Mouyuan Sun for simulating the CHAR model light curves, which were essential to my work.

Special thanks to my colleagues, S. Bernal, for providing the pPXF code used to fit the quasar spectrum, which was crucial for my analysis, and M. L. Martínez-Aldama, for discussing her expertise on the spectrum. I would also like to thank Prof. N. K. Chakradhari, Prof. Hum Chand, and Prof. S. K. Pandey, who guided me during my master's and laid the foundation for my academic career. Special thanks to Prof. Chakradhari for his unwavering encouragement and mentorship. His support during my master's studies and throughout my journey has been crucial in guiding my research interests and motivating me. Thanks to Prof. Valentino for providing me a new desktop computer when I did not have a laptop in the beginning.

My deepest gratitude goes to my family—my grandmothers, my mother Vaishnavi, my father K. R. Patel, my brother Piyush, my sister-in-law Renu, my nephew Harshil, as well as my tío and tía—whose love and support have been my greatest strength.

To my friends, thank you for always being there, encouraging me, and helping me through the challenges of this journey. I am deeply grateful to my friends Oindabi, Shruti, Kuleshwari, Neelima, Roshan, Shubham, Yashwant, Mamta and Praveen for their support before I joined the PhD and for being there when I had no financial means to come to Chile. To Antonia, Juanita and her family, Paula, Melissa, Paulina, and Alejandra thank you for the laughs, tears, foods, and adventures. I would also like to thank Amrita, Hemanth, and Bhoomika, Ravinder Aunty for sharing their space with me, supporting me through difficult times, and sharing meals with me. I am also thankful for the friendship and support of Alka, Shraddha, Sanjana, Mitesh, Payal, Akriti, and Yogendra, David. Lastly, a big thank you to Yus, Andrés, Luis, Carolina, and Patricio for being there when I needed help and for showing me new ways to look at life beyond my academic focus. Your support and friendship have truly made a difference.

A special thanks to the administrative staff at DAS, particularly Marta, and Hernan, for their help in making this experience smoother.

Table of Content

List of Tables

List of Figures

Chapter 1

Introduction

1.1 Active Galactic Nuclei

The terms "active galaxies" and "active galactic nuclei" (AGNs) refer to the key characteristic that differentiates these objects from inactive (normal or regular) galaxies: the presence of supermassive accreting black holes (BHs) at their centers.

The following definition is entirely observational: an object is characterized as an AGN if it meets at least one of the following criteria:

- It has a compact nucleus that emits much more energy than stellar emission coming from the same size region.
- Its center has the unique characteristic of a non-stellar continuum emission which is particularly unaffected by host contamination at X-ray and radio wavelengths.
- It has strong emission lines with line ratios typical of excitation by a non-stellar radiation field in its spectra/spectrum.
- It exhibits line and continuum fluctuations.

Based on the shape and width of the strong emission lines the AGN spectra can be separated into high-ionization type-I and type-II. In Type-II AGNs, only very narrow emission lines with typical full-width-at-half-maximum (FWHM) values of 400–800 km s^{-1} are observed. In type-I spectra, all permitted line profiles and a few semi-forbidden line profiles suggest high gas velocities, up to 5000-10,000 km s^{-1} when Doppler shift is taken into consideration.

Figure 1.1 shows the widely accepted unified model (Antonucci et al. 1993, Urry and Padovani 1995), representing the different AGN structures and depicting how the AGN appears from different viewing angles. Among the diverse family of AGNs, quasars represent some of the most luminous and distant objects in the universe. Quasars, or quasi-stellar objects (QSOs), are a subclass of AGNs characterized by their exceptionally bright nuclei, which can outshine their host galaxies. These powerful sources of energy are thought to be fueled by

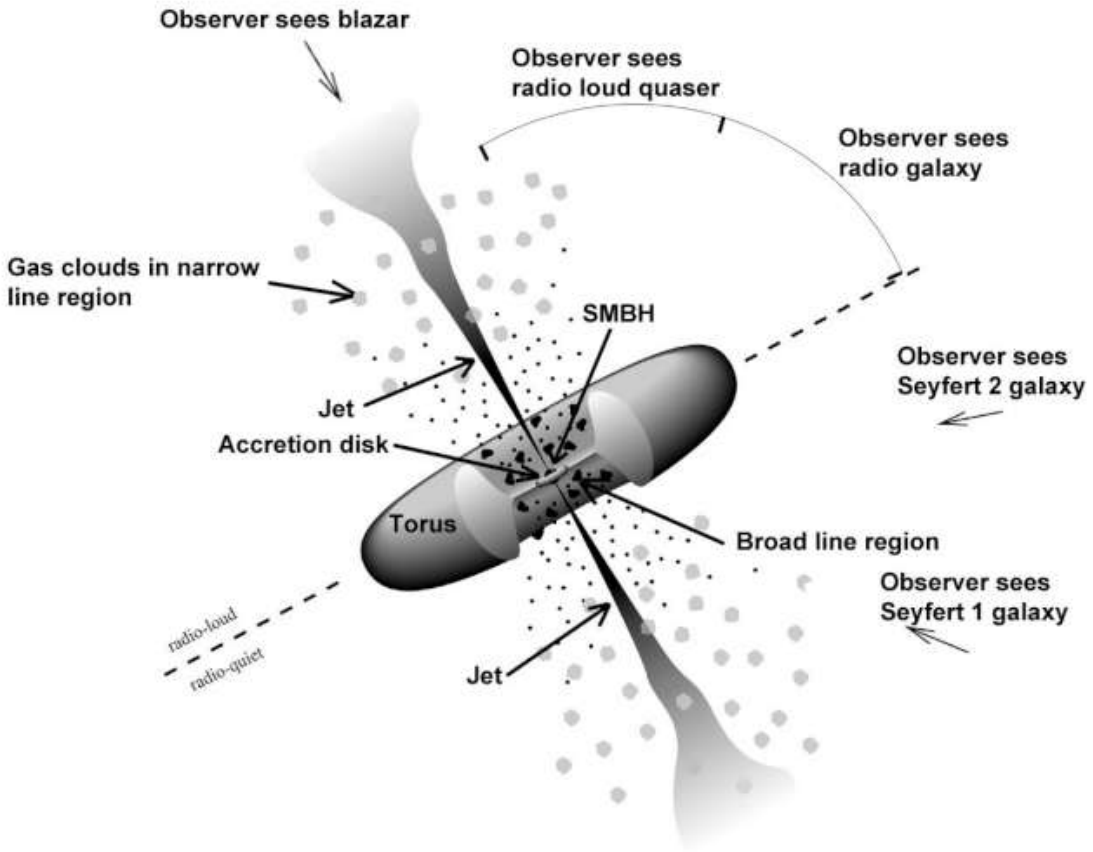

Figure 1.1: Active galactic nuclei, powered by the supermassive black holes in the center of galaxies. All AGNs have the same basic structure: accretion disk, broad-line region (BLR), the dusty torus, and narrow-line region (NLR), but they appear different depending on orientation of the observer. Image adapted from: Astronomical Society of the Pacific (Urry & Padovani, 1995, PASP, 107, 803).

accretion onto supermassive black holes (SMBHs) at the centers of galaxies. Quasars share many of the same observational characteristics as other AGNs, including strong emission lines and non-stellar continuum emission, but are distinguished by their intense luminosity and often, significant redshift, indicating their presence in the early universe. Studying quasars provides insights into the early stages of galaxy evolution and the role of supermassive black holes in shaping their host galaxies.

The corona of AGN is a highly energetic and poorly understood region that is thought to be responsible for producing the X-ray emission observed in most AGN. The corona is believed to be a region of hot plasma that is located above the accretion disk surrounding the central SMBH, producing high-energy radiation. As depicted in Figure 1.2, the accretion disk and corona, the BLR, the torus, and the NLR are the basic AGN structures from the very center to host-galaxy scales (Ramos Almeida & Ricci 2017).

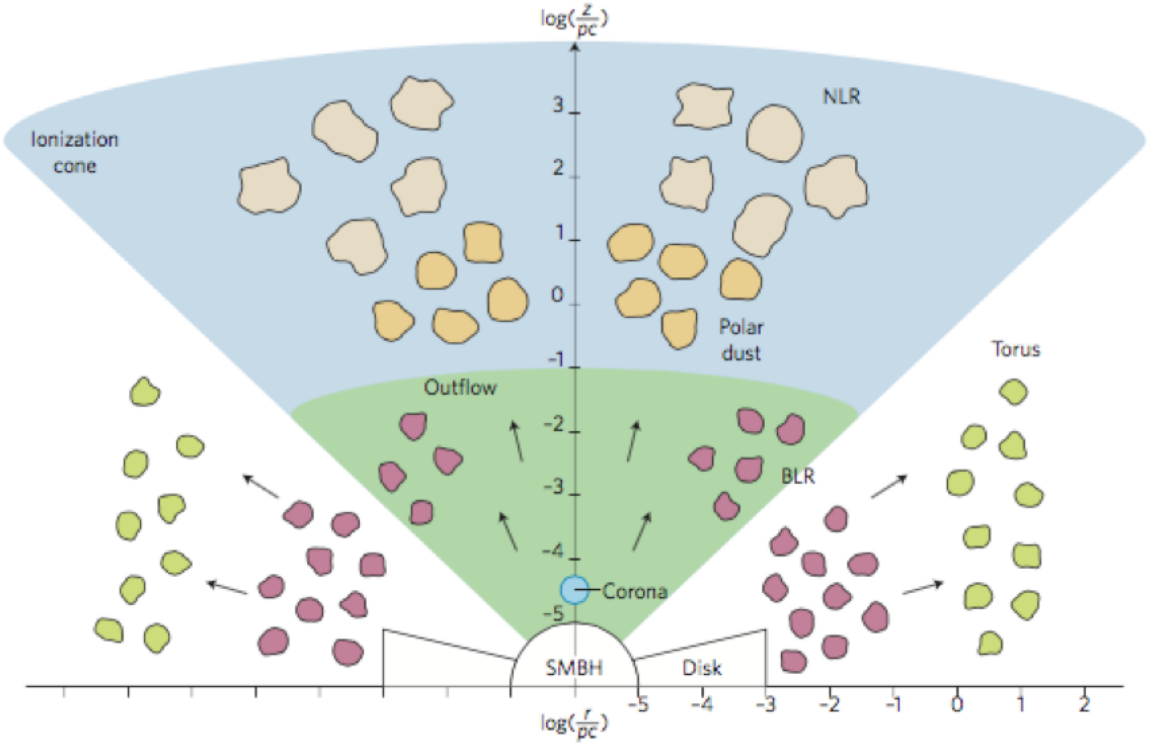

Figure 1.2: Sketch of the primary structures of an AGN as seen from both the equatorial and polar directions. Starting from the center and moving outwards towards the host galaxy, the components shown are the supermassive black hole (SMBH), the accretion disk and corona, the broad-line region (BLR), the torus, and the narrow-line region (NLR). Different colors in the figure represent different compositions or densities. (Ramos Almeida & Ricci 2017)

1.2 AGN variability

The Spectral Energy Distribution (SED) of AGN is a unique characteristic that sets them apart from other astronomical sources. This distribution shows the amount of electromagnetic radiation across a very wide range of frequencies, from radio to X-rays. The SED of the AGN accretion disk is particularly useful for identification purposes and can be differentiated from other sources, such as star-forming galaxies, as demonstrated in Figure 1.3. Despite being small in size, even for the closest and brightest AGN, the accretion disk is still easily distinguishable. When gas is accreted onto a supermassive black hole, the process is highly efficient, turning up to $5 - 42\%$ of the gravitational potential energy into radiation (which depends on the spin of the SMBH; e.g., Kerr 1963, Shapiro & Teukolsky 1983) and resulting in large luminosities for a minimal amount of accretion, which allows AGN to be detected at high redshifts.

Figure 1.3 below shows that the SED of AGN results from the superposition of radiation emitted by different components. The most luminous components are the "big blue bump" and the "IR bump". The big blue bump is the most prominent feature, and it is considered to be thermal radiation from the accretion disc. The IR bump is the thermal radiation emitted from the dusty torus, a possibly axisymmetric structure of high temperature dust heated by

accretion disk emission. The corona is responsible for the X-ray emission.

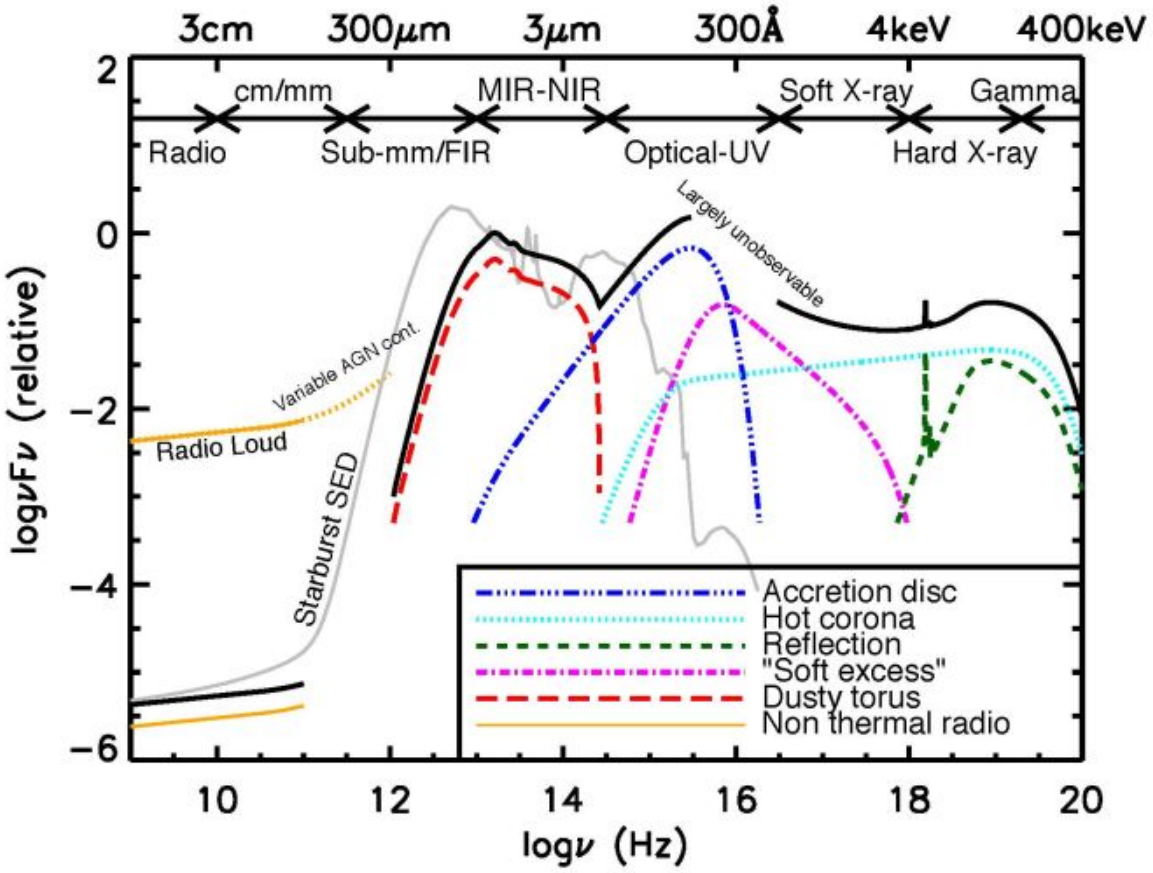

Figure 1.3: SED of the unobscured AGN is shown schematically in a black curve that has been divided into its primary physical components and contrasted with the SED of a galaxy that is generating stars (light grey curve). Credits: Harrison (2014).

The SED represents the average flux as a function of wavelength, and in AGNs, this flux exhibits time-varying emissions across all wavelength bands, spanning from hours to years, with faster fluctuations occurring at shorter wavelengths. This time variability across different wavelengths is one of the most ubiquitous properties of AGNs. Previous studies have aimed at understanding the mechanisms that account for such variations. The main results show that while the correlation between X-ray and UV/optical emission can be present (albeit with many complexities), strong correlation is seen at all other wavelengths from the far-UV to near-IR, particularly at timescales of weeks to months. This behavior already points to a different origin for the X-ray and UV/optical emitting regions, the X-ray corona, and the accretion disk, as already pointed out.

A significant degree of correlation between X-ray and UV/optical emission can be seen in the many studies (Arévalo et al. 2008, 2009; McHardy et al. 2016; Cameron et al. 2012; Pal & Naik 2018; Breedt et al. 2009, 2010; Shappee et al. 2014; Fausnaugh et al. 2018; Troyer et al. 2016; Kumari et al. 2021), other sources exhibit a good correlation during one campaign but become uncorrelated during another (McHardy et al. 2014; Starkey et al. 2017; Pal et

al. 2017; Lohfink et al. 2014), and many others completely lack a correlation between X-ray and UV/optical emissions (Behar et al. 2020; Gallo et al. 2018; Gliozzi et al. 2013, 2017; Morales et al. 2019). The correlation between X-ray and UV emissions is significantly weaker compared to the correlation observed within the UV/optical emissions (Edelson et al. 2019, Kumari et al. 2021).

Reverberation mapping (RM) observations seek to quantify these trends. They show small lags, few days at most, between optical and X-ray bands (Arévalo et al. 2008; Edelson et al. 2015; Edelson et al. 2019; Hernandez Santisteban et al. 2020; Lira et al. 2015). The Swift continuum reverberation campaigns have demonstrated that the relationship between X-ray and UV/optical variability in AGNs is intricate (see Figure 1.4). Specifically, Edelson et al. 2019 observed that the peak cross-correlation coefficients are generally much lower between the X-rays and UVW2 than between UVW2 and other UV/optical light curves. The correlation between X-ray and UVW2 light curves is consistently weaker compared to the correlation between UVW2 and other UV/optical light curves. For each object, X-ray fluctuations are faster compared to those in the UV/optical bands. Additionally, in three instances (NGC 4151, NGC 5548, NGC 4593), hard X-rays (HX) lead the UV (W2) by at least 1 σ uncertainties, while in another case (Mrk 509), HX seems to lag behind W2. However, due to the low cross-correlation coefficients (r_{max}) values, the reality of this observation is uncertain because of the dissimilarity between the X-ray and UV light curves.

As a consequence, the total AGN variability in UV/optical wavelengths has been proposed to corresponds to at least two components, the intrinsic variability caused by (local or global) changes to the accretion disk flow and the *reprocessing* of X-rays by the same disk. When X-rays from the corona illuminate the accretion disk, the incident flux heats up its surface and thermalizes to the local temperature, which decreases with disk radius as $T \propto r^{-3/4}$ in the standard disk prescription. This reprocessing of X-rays can explain the short-term fluctuations seen from the UV to the near-IR, their (partial) correlation with the X-rays and their strong observed interband correlations with day-long lags, which corresponds to the light travel time from the central corona to different locations in the disk.

However, long-term variations, which are likely to be dominated by intrinsic disk changes, dominate the optical variability at timescales of months to years. These long-term variations might propagate at different timescales, depending on the processes driving them. Understanding these long-term variations is crucial, as they originate from changes within the disk and can help to understand the physics mechanisms behind these accretion flows. In a simplistic scenario, if the UV/optical photons are the seed photons for the X-ray emission, being Compton up-scattered in the central corona, the X-ray emission will lag behind the UV/optical variations by the light travel time between the two emission regions, typically a few hours. Alternatively, if the UV/optical variations are caused by inwardly propagating accretion rate variations (Arévalo & Uttley 2006), these variations will eventually propagate inward at the viscous timescale and will affect the X-ray emission region. In this case, the X-ray variations will lag the UV/optical variations by approximately a few years.

Many AGN multiband light curves show variable time scales and amplitudes that appear

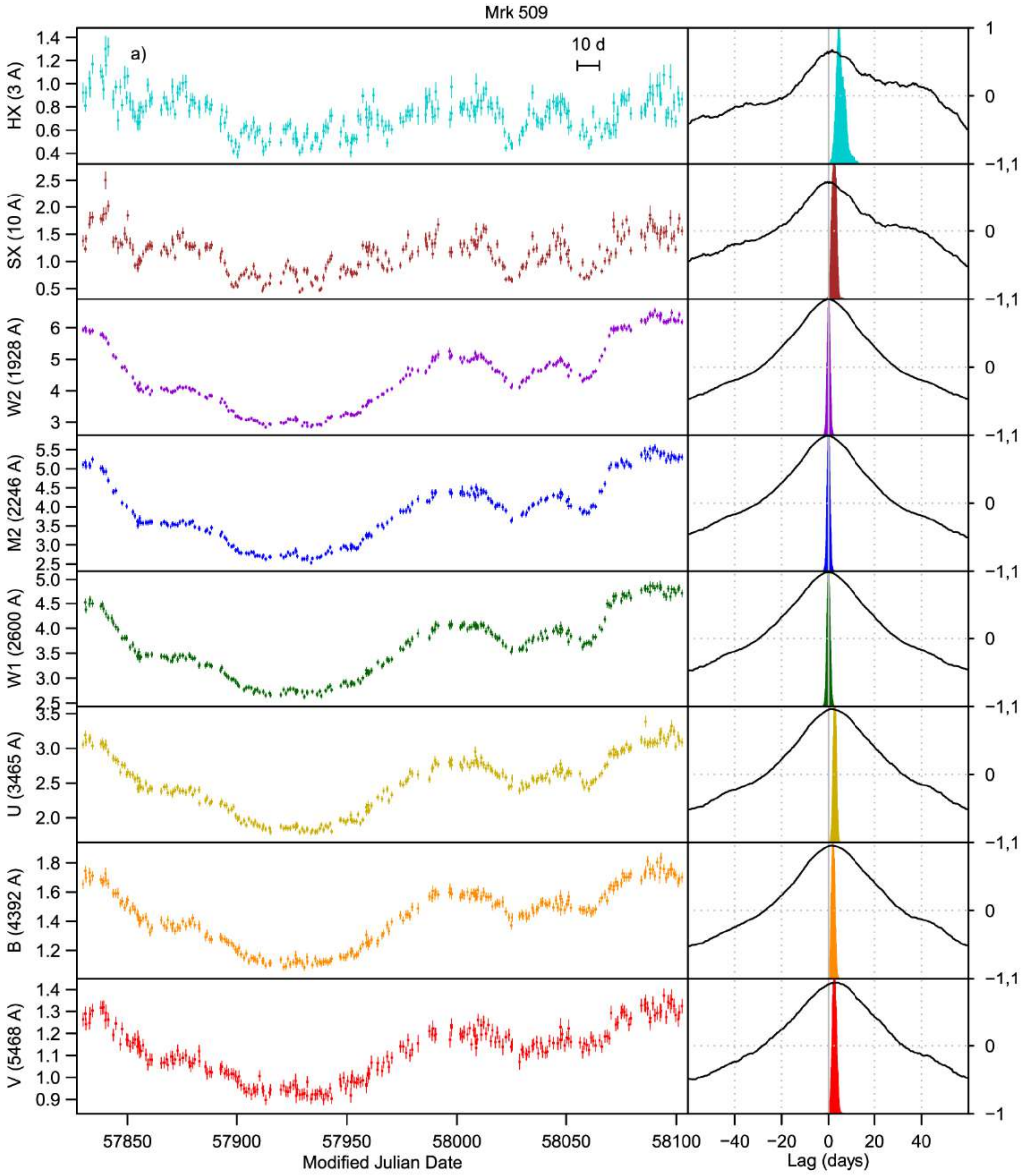

Figure 1.4: Left: Swift intensive disk reverberation mapping (IDRM) light curves for Mrk 509 ordered by wavelength. The top two panels in each subfigure show XRT data (HX covering 1.5–10 keV and SX covering 0.3–1.5 keV), and the bottom six show UVOT data. The X-ray data are in units of ct s^{-1} and the UVOT data are in units of 10^{-14} erg cm^{-2} s^{-1} $Å^{-1}$. Right: Interpolated cross-correlation function (ICCFs) (black lines; scale on the right) and "flux randomization/random subset selection" (FR/RSS) centroid distributions (same color as the light curves) for each band relative to the W2 band. Positive values mean the comparison band lags behind W2. The x-axes cover the full range of lags over which each ICCF is measured, and the y-axes cover the full range of r from -1 to $+1$. Vertical gray lines indicate lags in round numbers of days (solid at zero). The horizontal dashed gray line shows $r = 0$. The horizontal error bar in the upper right of the top (HX) panel represents 10 days for scale. Mrk 509 (a) was observed by Swift IDRM from March to December 2017, marking the first presentation of Swift data for this AGN, which has the highest mass ($\sim 1.1 \times 10^8\, M_\odot$) of any IDRM target observed to date. (b) This figure is similar to Figure 1.4 (a) but depicts data for NGC 4151, the second AGN examined using Swift IDRM. As NGC 4151 is usually the brightest or one of the brightest AGN across most observable wavelengths, its light curves are exceptionally well-defined, providing highly constrained interband lags.

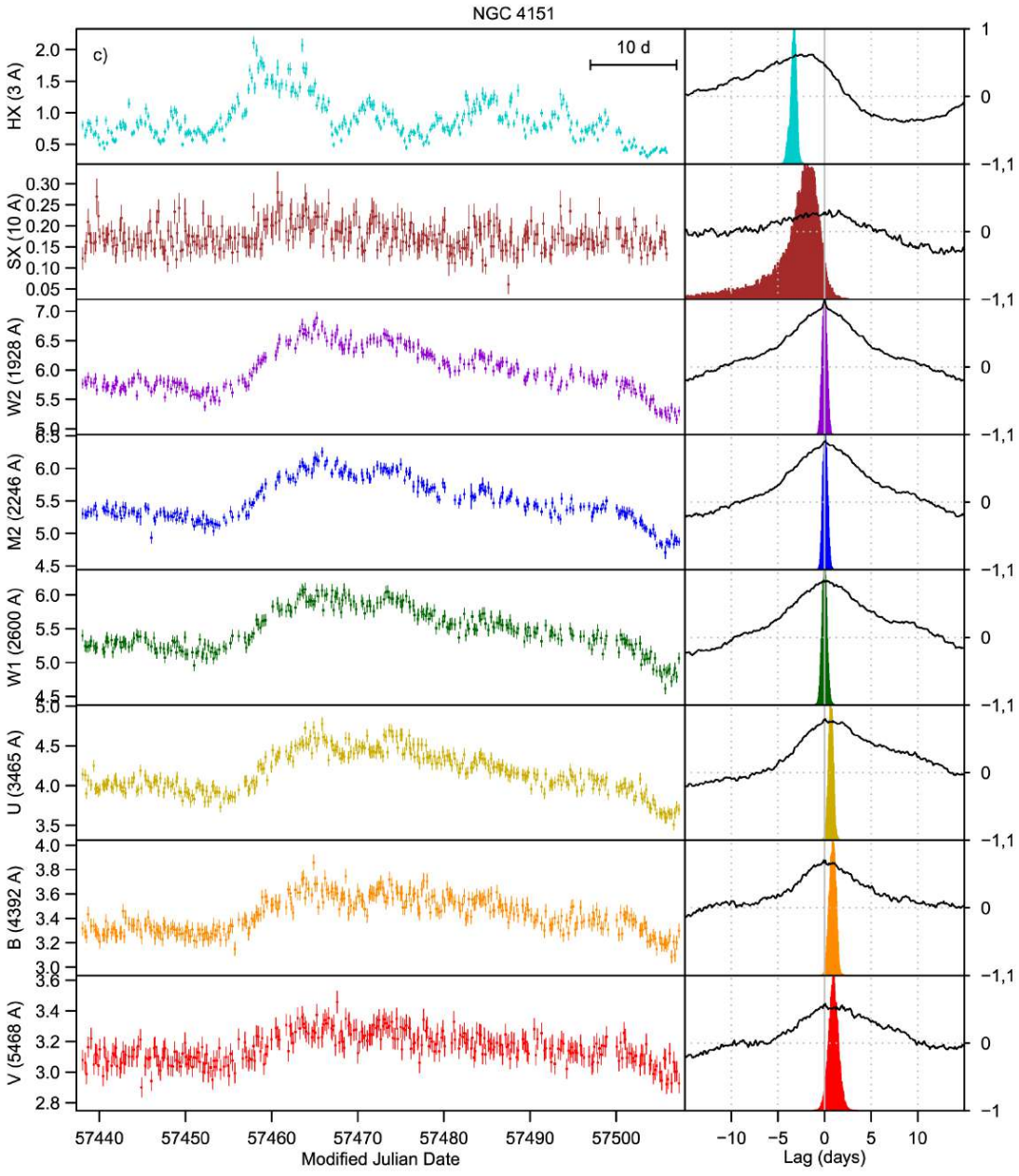

Figure 1.4 (b) (Continued): Swift IDRM light curve for NGC 4151

to be inversely proportional to the source luminosity. A clear anti-correlation between luminosity (L_{bol}) and variance in the brightness of quasars was reported in early investigations (Angione et al. 1972, Hook et al. 1994, Cristiani et al. 1997, Vanden Berk et al. 2004a). Some evidence suggests that the BH mass (M_{BH}) is the driving force behind the fluctuation amplitude. In fact, as compared to objects with larger BHs, AGNs with low-mass BHs have higher amplitude variations at all wavelengths (Kelly et al. 2009; Kelly et al. 2013). Because L_{bol} and M_{BH} are tightly correlated, it is difficult to distinguish the BH mass dependency from the luminosity dependence, as with several other claims.

In this thesis, we focus on quasars, exploring their variability and its dependence on rest-frame wavelength, to shed light on the mechanisms driving their emission. The advent of large-scale optical time-domain imaging surveys has significantly advanced our understanding of AGN optical variability. This surge in data, characterized by extensive light curve analyses, has been instrumental for AGN detection and selection, as explored in research by Kelly et al. (2009), Kozłowski et al. (2010), MacLeod et al. (2010, 2011), Schmidt et al. (2010), Butler & Bloom (2011), Kim et al. (2011), Ruan et al. (2012), Andrae et al. (2013), and Zu et al. (2013). These studies consistently demonstrate that AGN exhibit stochastic variations, typically around 10%-20% in flux over extended periods.

1.3 AGN variability and Accretion disks

The standard thin accretion disk theory, as proposed by Shakura & Sunyaev 1973, provides a foundational understanding of how an accretion disk operates by transferring matter inwards and angular momentum outward through viscosity. This mechanism is fundamental in driving the accretion process itself. According to this model, the azimuthal velocity within the disk approximately follows a Keplerian pattern at most radii, except the innermost region proximate to the Innermost Stable Circular Orbit (ISCO). Additionally, the temperature distribution across the disk is determined by a balance between the gravitational energy released during accretion and the cooling effect caused by black-body radiation, which subsequently establishes the radial temperature profile (where T is proportional to $r^{-3/4}$). Consequently, the gravitational energy of the gaseous matter within the disk is transformed into heat. Subsequently, a portion of this heat is converted into radiation, contributing to the partial escape of radiation from the accretion disk, and facilitating its cooling.

The characteristic timescales in AGN are closely related to the physical processes involved in the accretion of matter onto the SMBH. These timescales encompass the light crossing time (t_{lc}), the orbital time-scale (t_{orb}), the thermal time scale (t_{th}), the accretion disk front time scale (t_{front}), and the viscous time scale (t_{ν}).

The light crossing time describes the time scale for the irradiation of the disk by a source located at its axis and provides a maximum size limit for the region where the variations could have originated from (Peterson 1997). The orbital time-scale is the time it takes for the gas in the accretion disk to complete one orbit. The thermal time scale is the time scale required to establish thermal equilibrium, caused by fluctuations in the energy dissipation rate in a specific region of the accretion disk. The accretion disk front time scale (t_{front})

is the time it takes for thermal instabilities to spread or for cooling and heating fronts to propagate. Finally, the viscous time scale (t_ν) represents the time it takes for changes in the accretion rate to propagate through the entire disk due to the matter flux in the radial direction (e.g., Edelson & Nandra 1999; Peterson 2001; Kelly et al. 2009; Kasliwal et al. 2017, Stern et al. 2018; Ross et al. 2018). The definitions of these time scales are as follows:

$$t_{lc} = 1.1 \times \left(\frac{M_{BH}}{10^8 M_\odot}\right)\left(\frac{R}{100 R_S}\right) days, \tag{1.1}$$

$$t_{orb} = 104 \times \left(\frac{M_{BH}}{10^8 M_\odot}\right)\left(\frac{R}{100 R_S}\right)^{\frac{3}{2}} days, \tag{1.2}$$

$$t_{th} = 4.6 \times \left(\frac{\alpha}{0.01}\right)^{-1}\left(\frac{M_{BH}}{10^8 M_\odot}\right)\left(\frac{R}{100 R_S}\right)^{\frac{3}{2}} years, \tag{1.3}$$

$$t_{front} = 20 \times \left(\frac{h/R}{0.05}\right)^{-1}\left(\frac{\alpha}{0.03}\right)^{-1}\left(\frac{M_{BH}}{10^8 M_\odot}\right)\left(\frac{R}{150 R_S}\right)^{\frac{3}{2}} years, \tag{1.4}$$

$$t_{\nu} = 400 \times \left(\frac{h/R}{0.05}\right)^{-2}\left(\frac{\alpha}{0.03}\right)^{-1}\left(\frac{M_{BH}}{10^8 M_\odot}\right)\left(\frac{R}{150 R_S}\right)^{\frac{3}{2}} years, \tag{1.5}$$

R represents the radial distance from the central black hole, M_{BH} is the black hole mass and the Schwarzschild radius ($R_S = 2GM_{BH}/c^2$) defines the black hole horizon for a non-rotating BH. The standard disk viscosity parameter (α), and the accretion disk height (h) determine t_{th}, t_{front} and t_ν, as they are set by the accretion process itself.

According to these equations, for a black hole with a mass of about $10^8 M_\odot$, the time-scale for t_{lc} must be associated with very fast variability, with a typical duration of hours to a few days, as seen in Reverberation Mapping campaigns. On the other hand, t_{orb} and t_{th} are related to variability with time scales of a few months or a few years. t_{front} and t_ν are linked to long-term timescale AGN variability, which can last for tens or hundreds of years. Additionally, these equations suggest a strong correlation among the time-scale of AGN variability, the black hole mass, and the radius of the accretion disk, which has been confirmed by previous studies (e.g. McHardy et al. 2006; Kelly et al. 2009; MacLeod et al. 2010).

1.4 AGN optical variability and its dependence on physical properties of AGN

Understanding the variability properties of AGN is crucial for exploring the physical properties of supermassive black holes. Prior studies have found that the observed variability in multiband light curves of type-I AGNs inversely correlates with the source luminosity, with this relationship being especially prominent in the X-ray and optical bands (Angione & Smith 1972; Hook et al. 1994; Cristiani et al. 1997; Vanden Berk et al. 2004b). However, standard accretion theory shows that luminosity corresponds to the product of black hole mass and accretion rate. Hence, it is not straightforward to know which of these two properties drives the observed variability.

Many works have determined a statistically significant anti-correlation between variance and Eddington ratio (Kelly et al. 2009, 2013; MacLeod et al. 2010; Zuo et al. 2012; Simm et al. 2016; Rakshit & Stalin 2017; Sánchez-Sáez et al. 2018; Lu et al. 2019)). Although extensive research has been carried out to try to identify a correlation between variability and black hole mass, past studies found conflicting results. For instance, several researchers have discovered a direct correlation between variability and black hole mass (Wold et al. 2007; Wilhite et al. 2008; MacLeod et al. 2010; Lu et al. 2019), while others have found either an inverse relationship (Kelly et al. 2009, 2013) or no clear link at all (Zuo et al. 2012; Simm et al. 2016; Rakshit & Stalin 2017; Li et al. 2018). This contradictory result can be attributed to the timescale at which the variability has been estimated.

1.5 Theoretical modelling

As already pointed out, numerous works have highlighted the absence of anticipated robust correlations between X-ray and UV/optical emission that would be expected in the reprocesing scenario (see Figure 1.5) (Edelson et al. 2019; Zhu et al. 2018; Morales et al. 2019; Hagen et al. 2022). There is also a discrepancy in the energy budget, as the X-ray luminosity needed to account for the observed variability in UV/optical emissions seems to be unreasonably high (Clavel et al. 1992; Dexter et al. 2019; Just et al. 2007; Strateva et al. 2005; Lusso et al. 2010). The problem becomes especially important in AGNs that exhibit strong variability (Dexter et al. 2019). This makes it difficult to provide a complete explanation of disk variability using the X-ray reprocessing model only (Gaskell 2007). However, distinct spectral features observed in the X-ray spectra of AGN support the idea of X-ray reprocessing. These features include the 6.4 keV Fe $K\alpha$ emission and the Compton hump, which can be observed in hard X-rays beyond 10 keV. These features are commonly associated with X-ray reflection caused by the accretion disk. It has been firmly established in a few AGN that the variability of these emissions lags shortly behind changes in the X-ray continuum. This has been demonstrated by studies such as Zoghbi et al. (2014) and Kara et al. (2015).

In the research conducted by Kang et al. (2018), a direct connection was observed between X-ray loudness and UV/optical variability, which strengthens over timescales up to 10 years, but diminishes on timescales shorter than 100 days. This trend suggests the influence of a

slow, long-term physical process, and suggests a strong connection between X-ray coronal heating, UV/optical variation in quasars, and the dynamics of magnetic disk turbulence.

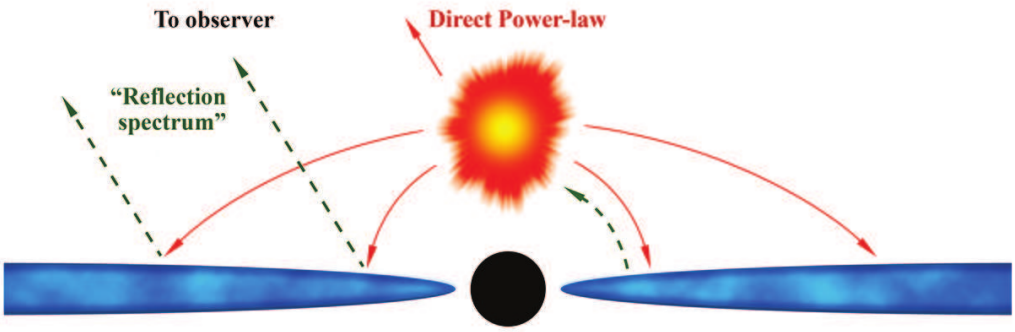

Figure 1.5: Illustrative figure displays an emitting corona (in orange) positioned above the accretion disk (in blue), both revolving around a central black hole. Observers can detect both the direct emission from the corona and its reflected or back-scattered spectrum. Close to the black hole, the intense gravitational field bends the light significantly. The delay observed, known as the reverberation signal, arises due to the difference in light-travel time between the direct emission changes and those seen in the reflection spectrum. Credits: Uttley et al. 2014.

Sun et al. 2020a developed a Corona-heated Accretion-disk Reprocessing model (CHAR), which assumes that the magnetic field tightly couples the accretion disk ($\gtrsim 10$ Schwarzschild radius) and the corona (see Figure 1.6). According to this theory, magnetic turbulence in the corona produces X-ray fluctuations. This process magnetically drives the variations in the heating rate of the accretion disk and results in temperature fluctuations, effectively replacing the X-ray radiative heating as the mechanism to drive the observed variability. Still, a strong connection between X-ray and UV/optical emission should be present in the CHAR model too. However, the significant advective cooling and the variations in the corona surface density can make the relationship between the magnetic fluctuations (with the power of Q^{+}_{mc}) and X-ray emission challenging to understand. This effect could cause the reported weak correlations between X-ray and UV/optical emission. In addition, the corona is possibly optically thin and made up of low-density plasma. Since protons and electrons are decoupled, the magnetic turbulence gets dissipated to increase the internal energy of protons (Di Matteo 1998; Różańska & Czerny 2000; Yuan & Narayan 2014). Thus, only a small portion of the magnetic instability drives the X-ray in the corona, and the rest of the energy causes the change in the accretion disk structure and results in UV/optical fluctuations, which solves the energy-budget problem of the X-ray reprocessing model. Moreover, the CHAR model is able to describe observed larger-than-expected time lags in some AGNs. The model can also explain a broad scope of quasar UV/optical variability and its connection to quasar physical properties.

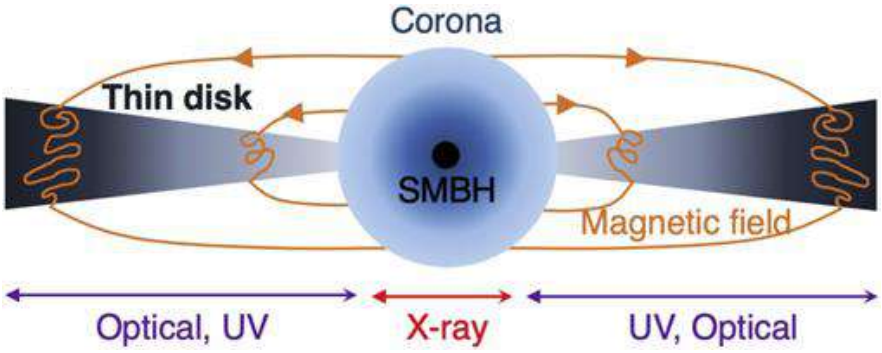

Figure 1.6: CHAR model, describes the interaction between the accretion disk, depicted in gray, and the corona, shown in light blue, as being intricately connected through magnetic fields, represented by orange lines. It is important to note that the accretion disk may reach up to the innermost stable orbit, but the contributions of these inner parts to the UV/optical variability we are focusing on are minimal. Magnetohydrodynamic (MHD) activities, such as flares within the corona, have the potential to influence MHD turbulence in the accretion disk, leading to variations in the disk heating rate. Consequently, the disk temperature varies in accordance with the changing heating rate. These temperature fluctuations can be quantified using the thermal-energy conservation equation. Credits: Sun et al. (2020a)

1.6 Recent advancement in the understanding of long-term AGN variability

As it will be shown in Chapter 2, the power spectrum density (PSD, which quantifies variability power or variance as a function of frequency) encapsulates the variability properties of AGN. For a bending power law model for the PSD of the form:

$$P(f) = \frac{A f^{\alpha_L}}{1 + (f/f_b)^{\alpha_L - \alpha_H}}, \tag{1.6}$$

Where the damping timescale τ_{damp} represents the characteristic timescale at which the variability transitions from a random walk pattern at high frequencies to a plateau at lower frequencies.

The equation 1.6 determines the dependency of its normalization (A), bending frequency ($f_b \sim 1/\tau_{damp}$), and high and low frequency slopes (α_H, and α_L), as a function of black hole mass and accretion rate (for a given wavelength) will help to understand the nature of the underlying processes driving variability. In particular, Burke et al. 2021 established a relationship between f_b and black hole mass, while its dependency on rest-frame wavelength was recently reported by Stone et al. (2023).

In two very recent works Arévalo et al. (2023, 2024) (P. Patel included), have studied statistical significant samples of quasars with known black hole masses (M_{BH}) and accretion rates ($R_{\rm Edd}$) to determine their connection with variability. Arévalo et al. (2023) showed

that the dependency on variability was different for different time scales, implying that not only the normalization of the power spectrum density was a function of M_{BH} and R_{Edd}, but also its shape. In particular, Arévalo et al. 2024 proposed that these dependencies can be understood assuming a universal PSD. The following dependencies were explored:

$$\log f_b = \log B + C \times \log M/M_8 + D \times \log R_{Edd}/0.1 \quad (1.7)$$

$$\log A = \log A1 + F \times \log R_{Edd}/0.1, \quad (1.8)$$

$$A1 = A2 \times B/f_b \times f_b^{-a_L} \quad (1.9)$$

The variables f_b and B are expressed in units of $days^{-1}$. A1 and B represent the normalization of the power spectrum and the bend frequency, respectively, for quasars with a mass of 10^8 $M_\odot$ and a dimensionless Eddington ratio (R_{Edd}) of 0.1. With this scaling method, the variance ($P \times f$) is equal to $A2 \times B$ at the bend frequency for all mass bins when $R_{\rm Edd} = 0.1$. For other ranges of $R_{\rm Edd}$, this relationship scales in proportion to $R_{\rm Edd}$, formulated as $P(f_b) \times f_b = A2 \times B \times (R_{\rm Edd}/0.1)^F$.

Since the method used to measure variance and the sampling pattern of light curves can impact measurements, Arévalo et al. (2024) simulated light curves based on a model PSD (Eq.1.6) for different values of α_L and α_H, using time samplings reflecting actual observations (see Figure 1.7). This approach allows for a comparison between observed variances and a modified, or 'folded', model. A grid search was performed to identify the optimal parameters B, C, D, and F. The optimal value of A2 was identified by minimizing the difference between the sum of the variances from the data and the variances from the model.

Each set of parameters was assessed and assigned a figure of merit, represented as fom:

$$fom = \sum_{bins,timescales} \frac{(\tilde{var} - var)^2}{err^2}, \quad (1.10)$$

Table 1.1 summarizes the optimal parameter values and the minimum figure of merit (fom) obtained from the fitting process.

In Figure 1.7 the observed power spectrum is represented by large dots and a successful 'folded' model is represented by small black dots. The model closely mirrors the data with some variation, attributed to the sampling of the light curves and the stochastic nature of the 'folding' process. Figure 1.8 shows discrepancies between the model and actual data points, normalized by data point errors and color-coded according to mass. The universal power spectrum model provided a strong fit to the data, especially with a high-frequency slope of $\alpha_H = -3$, low-frequency slopes of $\alpha_L = -1$ and $\alpha_H = -2.5$ and $\alpha_L = -0.5$ or $\alpha_L = 0$. This implies a rapid suppression of fast variability for frequencies above f_b. Models with a less steep high-frequency slope of $\alpha_H = -2$, similar to the Damped Random Walk model (see Chapter 2), performed poorly in fitting our data.

α_L	α_H	$A2$	B	C	D	F	fom/N
0	-2.5	1.5	0.0052	-0.65	-0.30	-0.50	2.0
-0.5	-2.5	1.4	0.0052	-0.60	-0.30	-0.45	1.9
-1	-2.5	1.1	0.0058	-0.60	-0.35	-0.40	2.3
-0.5	-3	0.71	0.0086	-0.60	-0.35	-0.40	2.4
-1	-3	0.42	0.0104	-0.55	-0.35	-0.40	1.7

Table 1.1: Optimal parameters and associated figure of merit for the top five power spectrum models, indicated by their low and high-frequency slopes in the initial columns. These parameters are detailed in Eqs. 1.6, 1.7, 1.8, 1.9. Here, N represents the total count of power spectral data points, calculated as the product of the number of timescales and the number of M_{BH}-$R_{E\mathrm{dd}}$ bins. This set of results comes from the second run, which employed a finer grid for analysis.

The results show a distinct correlation between the $\tau_{damp} \sim 1/f_b$, and $R_{E\mathrm{dd}}$, in addition to the established dependence of τ_{damp} with M_{BH}. The fitting results indicate that τ_{damp} varies as $M_{BH}^{0.65-0.55}$ $R_{E\mathrm{dd}}$ $^{0.35-0.3}$, with the ranges in the exponents representing the best-fitting parameters for power spectrum models. Since the exponents for the dependence on mass and on $R_{E\mathrm{dd}}$ are distinct it is not possible for the bend timescale to be solely determined by the bolometric luminosity, which is the result of both parameters. Furthermore, due to the exponent of the dependence on $R_{E\mathrm{dd}}$ being significantly different from 0, it is evident that the bend timescale is not solely determined by mass.

A summary of the results is that while the Eddington ratio predominantly controls amplitude, the damping timescale is more strongly dependent on black hole mass. It suggests that quasars with larger black hole masses have lower variability amplitudes due to these smaller break frequencies. It also implies that the PSDs of larger black hole masses would be steeper compared to those with lower black hole masses, considering the impact of the break frequency on the PSD normalization. It also provides additional evidence to the growing body of work suggesting deviation from the DRW model in quasar variability studies.

Measuring the wavelength dependence of the bend timescale remains a significant challenge, given its subtle effect, considerable uncertainties, and dependence on different black hole parameters. Nevertheless, a connection has been discovered by analyzing the timescale of variability using the Structure Function (see Chapter 2), although the reported dependence is relatively small. Using the DRW model and τ_{DRW}, a study demonstrated a correlation with rest-frame wavelength that was stronger but not as strong as expected by the thin disk model. It is highly probable that the Vera Rubin LSST (Ivezić et al. 2019) will offer additional insights into this matter in the future.

It is possible that both the variability damping timescale and the power spectrum slopes could be affected by wavelength. In our work, Chapters 3 and 4 will carry out an analysis on the dependence of variability power on wavelength (Patel et al. 2024, A&A, accepted) by examining this dependency for different timescales.

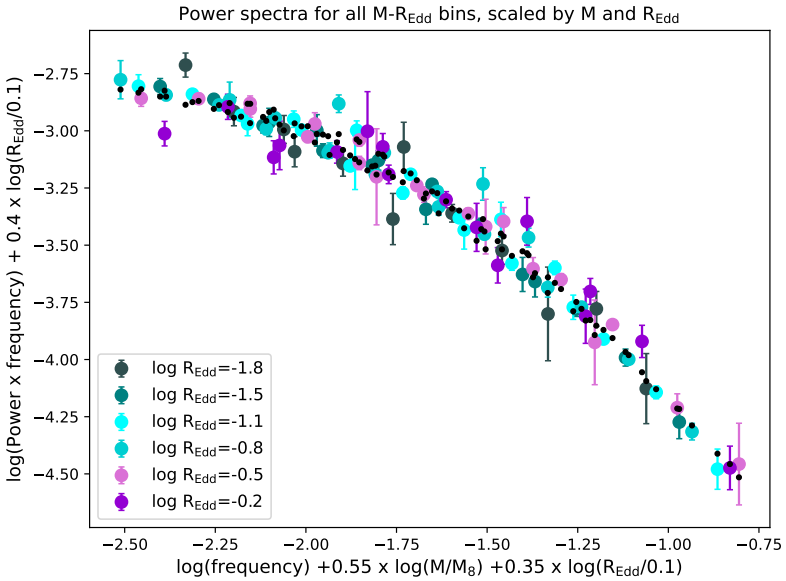

Figure 1.7: Power spectra (Power × frequency) of the data are displayed with large dots, each color-coded according to $R_{E\mathrm{dd}}$, after rescaling frequencies and amplitudes based on the mass, $R_{E\mathrm{dd}}$ of each bin, and the optimal scaling parameters C=-0.55, D=-0.35, F=-0.4. Black dots depict a 'folded' model derived from a bending power-law model with $\alpha_L = -1$ and $\alpha_H = -3$. Frequencies are expressed in units of day^{-1}.

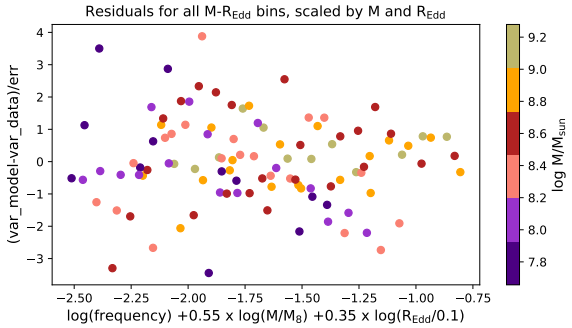

Figure 1.8: Residuals of the model and data plotted in Fig.1.7, color coded by mass. Frequencies are in units of day^{-1}.

1.7 Data Overview

The work described in this thesis is based on data collected by the Zwicky Transient Facility (ZTF). ZTF is an automated survey conducted using the Palomar 48-inch Schmidt Telescope. It is designed to survey the northern sky with a field of view of 47 square degrees, employing a 600-megapixel camera. ZTF can cover an area of 3760 square degrees per hour, reaching median depths of approximately g$\sim$20.8 and r$\sim$20.6 magnitudes (AB, 5 σ in 30 seconds) as reported by Masci et al. (2019). ZTF follows in the footsteps of its predecessor surveys, starting with the Palomar Transient Factory (PTF) and then the intermediate PTF (iPTF) program, both of which were conducted using the Palomar 48-inch Schmidt Telescope (P48) at Palomar Observatory. (Law et al. 2009, Rau et al. 2009). ZTF aims to survey the Northern Hemisphere sky repeatedly in three different wavelengths. These observations will cover time scales ranging from minutes to years. The expected outcome of this survey includes the discovery of young supernovae and rare transients associated with relativistic events, the formation of systematic samples of Tidal Disruption Events, AGN, variable stars, and precise measurements of various solar system objects (Bellm et al. 2019).

1.8 Motivation and thesis overview

AGN variability seems to be closely tied to black hole properties. Understanding these fluctuations helps in studying the feeding mechanisms of SMBHs and how matter transitions from the accretion disk into the black hole, including the role of magnetic fields and relativistic jets. Studying AGN variability not only enhances our knowledge of the physics governing these luminous objects but also contributes to broader astrophysical questions related to the formation and growth of SMBHs, the evolution of galaxies, and the fundamental physics of accreting systems.

However, characterizing AGN variability remains a significant challenge in astrophysics. The complexity of their variability across different wavelengths and the connections to fundamental properties like luminosity, black hole mass, and Eddington ratio highlights the need for further research. With the upcoming Legacy Survey of Space and Time (LSST) by the Vera C. Rubin Observatory on the horizon, there is clear need to be prepared to explore AGN variability from large data sets that will be available in the near future. In this context, my thesis utilizes data from ZTF to explore the optical variability of quasars, focusing on its relationship with rest-frame wavelength over different timescales. Determined correlations will in turn inform accretion disk models. The aim is to extend our comprehension of AGN variability, and help to prepare for the upcoming opportunities presented by large-scale time-domain surveys.

In this thesis, we continue with the work published in Arévalo et al. (2023, 2024). Samples correspond to SDSS quasars with well determinedM_{BH} and R_{Edd} values and good quality ZTF light curves. Following Arévalo et al. (2023, 2024), an ensemble study approach to examine quasar variability is used by averaging variability over large samples to uncover common trends, despite the fact that each quasar has distinct light curves. In this way it is expected that departures from common trends will be averaged away, keeping the relevant

physical information about the driving mechanisms driving variability.

1.9 Thesis Outline

Including this introduction, the thesis is comprised of 4 chapters.

Chapter 2 presents a detailed study of the analytical tools and methods used in AGN variability research. This section outlines techniques for analyzing AGN time series, including Damped Random Walk, CARMA, PSD, and Structure Function models, to examine the statistical characteristics and underlying mechanisms of stochastic AGN variability. It includes discussions on variance estimation using the Mexican Hat filter and Power Spectral Density analysis. Additionally, it covers simulation techniques for generating synthetic light curves to understand quasar variability.

Chapter 3 presents the statistical analysis connecting variability and rest-frame wavelength across different timescales (30, 75, 150, and 300 days). The study found that the anti-correlation between variability and rest-frame wavelength gets stronger with shorter timescale. We discuss how the amplitude and the slope of power spectra depends on the rest-frame wavelength.

Chapter 4 presents the validation of the CHAR model by comparing the results for the dependence of variability on the rest-frame wavelength using ZTF data. CHAR model considers the thermal-conservation model and magnetic coupling between the corona and the accretion disk. Utilizing the extensive dataset from the ZTF, we conducted a detailed comparison between the CHAR model predictions and quasar variability as a function of rest-frame wavelength, across four timescales studied.

Chapter 2

Tools for the analysis of AGN variability

This chapter will introduce essential analytical tools and methods used in AGN variability studies used in Chapters 3, and 4 of this thesis.

2.1 Introduction

AGN exhibits complex variability that provides critical insights into the physical processes occurring in the vicinity of supermassive black holes. This chapter is dedicated to exploring the essential tools and methodologies employed in the study of AGN variability, as applied in the subsequent chapters of this thesis. These tools, based on the methodologies outlined in Arévalo et al. (2023) and (2024) and Patel et al. (2024, A&A, accepted), are necessary to describe the properties of AGN variability in a quantitative manner. AGN light curves, often characterized by irregular sampling, noise, and significant stochastic variations, demand robust analytical approaches to extract meaningful patterns and trends. This chapter provides a comprehensive overview of key tools and methods used in AGN variability studies, emphasizing their application to the analysis of light curves and the extraction of relevant physical parameters.

The chapter is structured to provide a detailed exploration of each tool. It explores the AGN stochastic variability and the statistical functions used to quantify it, such as the Power Spectral Density (PSD), and Structure Function (SF). It also presents the most common prescriptions used for its description, such as the Damped Random Walk (DRW) and Continuous Auto-Regressive Moving Average (C-ARMA) models. The application of the Mexican Hat code for PSD estimation is also discussed.

This chapter also covers the generation of artificial light curves using simulation techniques, with known statistical and variability properties, to understand those artifacts caused by observing and analysis constraints. These simulations help in understanding the impact of various parameters on quasar variability and in identifying potential biases in observational data.

Additionally, methodologies like bootstrapping and linear regression analysis are explored, highlighting their role in error estimation and the robust analysis of AGN variability.

The chapter is structured as follows: Section 2.2 covers the techniques to examine AGN variability. Section 2.3 explores the Mexican Hat filter method for variance estimation. Section 2.5 introduces simulation techniques used to generate synthetic light curves. Section 2.6 provides a brief summary of our conclusions.

2.2 Extracting information from AGN time series

Unlike events confined to specific time periods, stochastic variability of AGN encompasses behavior that is not predictable, as in the case of periodicity. Stochastic processes can be quantified, despite their stochasticity. This is briefly covered in this section. The Damped Random Walk (DRW) and Continuous Auto Regressive Moving Average (CARMA) are models used to describe AGN variability, while its Power Spectral Density (PSD) and Structure Function (SF) provide means to sample the true underlying behavior. These techniques allow us to examine the statistical characteristics of AGN variability and obtain details about its underlying mechanisms.

Power Spectral Density (PSD)

The PSD is a statistical description that quantifies the frequency content of time series data, providing insights into the underlying mechanisms causing variability at different time scales (Vaughan et al. 2003)[1]. Usually, in real physical systems, the total PSD can be described as a superposition of many processes responsible for the variability at various time scales and it can be described as a power-law for the simplest cases, i.e., P $(\nu) \propto \nu^{\alpha}$. Depending on the processes engaged in the variation, the value of α changes. For example, a white noise process has a value of $\alpha = 0$, while a Damped Random Walk process has a value of $\alpha = -2$.

In the X-rays, PSDs were initially characterized as power laws in the 90s (McHardy & Czerny 1987, Lawrence & Papadakis 1993 1993). About ten years later, a broken power law was proposed for X-Ray Binaries (XRBs) and AGN (Nowak 2000; Ezoe et al. 2001). Later, McHardy et al. 2004 found that AGN X-ray PSDs are better characterized by smooth transitions rather than sharp breaks where α changes from ~ -1 to -3.

The observed optical PSD has also been modeled as a broken (or bending) power law (Mushotzky et al. 2011, Zu et al. 2013, Kasliwal et al. 2015, Caplar et al. 2017, Sánchez-Sáez et al. 2018, Stone et al. 2022). The bending power law model allows for a gradual transition between slopes, avoiding abrupt changes and better reflecting observed variability patterns. The general form of this PSD is described by:

[1]In Vaughan et al.(2003) a distinction is made between a PSD and its Periodogram, where the PSD corresponds to the underlying variability process while one realization of such is known as a Periodogram. In this Thesis we will not make such a distinction.

$$P(f) = \frac{A f^{\alpha_L}}{1 + (f/f_b)^{\alpha_L - \alpha_H}}, \tag{2.1}$$

where the power spectrum normalization is denoted by A, and the bending frequency by f_b. In this model, the power law has a slope α_L below the break frequency and a steeper slope α_H above the break frequency.

Figure 2.1 illustrates a model broken power law in the optical band of an AGN. It can be observed that there is more variability at smaller frequencies. This is referred to as a "red-noise" behavior, which characterizes the PSD in regions 3 and 2. Specifically, region 3 follows the relation $P(f) \propto 1/f$, while region 2 follows $P(f) \propto 1/f^2$ which corresponds to a Damped Random Walk. At the highest frequencies, there is a flat section that follows a white-noise pattern.

To estimate the PSD of a discrete light curve it is necessary to first subtract the mean flux. This removes the zero-frequency value of the PSD, which carries no information about its shape. Next, the discrete Fourier Transform (FT) is determined for a range of frequencies determined by the total length of the light curve ($\nu_{\min} = 1/T$, where T is the total duration of the time series) and its sampling ($\nu_{\max} = \nu_{\rm Nyq} = (2T/N)^{-1}$, where N the total number of points). Finally, the PSD is obtained as the modulus squared of the real and imaginary part of the FT (e.g., Uttley et al. 2002). This method, however, carries important challenges, such as aliasing and "red-noise leakage", which are made worse by the uneven and coarse sampling of astronomical time series.

Alternatively, the PSD can be obtained if we plot variance as a function of frequency. The variance of the flux is a measure of variability amplitude within a specific $\Delta\nu$. The variance is expressed as:

$$\sigma^2 = \frac{\Sigma_{\rm i=1}^{N} (f_{\rm i} - \langle f_{\rm i} \rangle)^2}{N} \tag{2.2}$$

where $\langle f_{\rm i} \rangle$ is the average flux across all N observations, i.e. $\langle f_{\rm i} \rangle = \frac{1}{N} \Sigma_{\rm i=1}^{N} f_{\rm i}$.

The Mexican Hat method, described below, makes use of this simplified prescription to determine the PSD of AGN for irregular sampling.

The Structure Function (SF)

The structure function (SF) is a method to quantify the variability of AGN light curves, and it provides information about the magnitude of variability as a function of time lag instead of frequency.

The structure function is calculated as the standard deviation of the time series by taking the flux difference between t_2 and t_1, where $\Delta t = t_2 - t_1$ is the time lag. When the structure function SF increases proportionally with time as a power law ($SF \propto t^{\alpha}$), then the PSD decreases proportionally with frequency (PSD $\propto 1/{\rm f}^{1+2\alpha}$). Hence in the case of white-noise

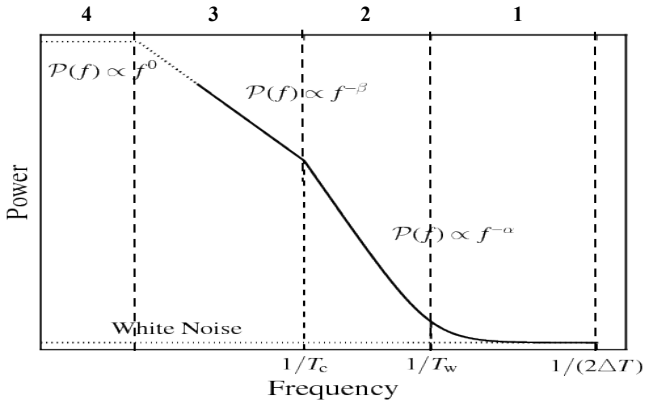

Figure 2.1: The broken power law that is used to model the PSD of AGN (Zhu & Xue 2016).

α has a value of zero, while for the damped random walk α has a value of 0.5.

SFs are generally believed to be less affected by aliasing issues caused by irregular sampling (Hughes et al. 1992, Collier et al. 2001). However, problems with an overinterpretation of its shape are also well-documented (Emmanoulopoulos et al. 2010)

The structure function can be related to the autocorrelation function (ACF):

$$SF(\Delta t) = SF_\infty[1 - ACF(\Delta t)]^{1/2}, \tag{2.3}$$

The standard deviation of the time series, calculated over a very long time interval or longer than any relevant timescale τ, is referred to as SF_∞. The ACF for the damped random walk is defined by:

$$ACF(t) = exp(-t/\tau), \tag{2.4}$$

Using equation 2.4, the SF can be written as:

$$SF(t) = SF_\infty[1 - exp(-t/\tau)]^{1/2}, \tag{2.5}$$

where the asymptotic value of the structural function is SF_∞.

2.3 Mexican Hat Code

The Mexican Hat Code method (Arévalo et al. et al. 2012) is easy to implement, robust, and computationally efficient. It does not require any tuning parameters, and the resulting power

spectrum is easy to interpret. The method gives a low resolution power spectrum, making it suitable for analyzing cases where the underlying power spectrum is a smooth function of wavenumber or frequency, which is assumed to be true for AGN in the absence of narrow features such as Quasi-Periodic Oscillations (QPOs). A key advantage is its ability to handle data with significant gaps of varying sizes without any modifications. This is especially useful for AGN light curves from large surveys, where estimating aliasing and red-noise leak for each AGN is challenging. This makes it particularly useful for studying the stochastic, red-noise dominated variability in AGN light curves, focusing on the broad-band shape of the power spectrum.

As outlined before, the first step is the subtraction of the mean flux from each individual light curve. After subtraction, the light curves with a mean of zero are normalized by their respective pre-subtraction mean flux. By normalizing the data, we can effectively compare the variability amplitude or variance of light curves that have different flux levels.

For a light curve without gaps, a Mexican Hat filter can be used to isolate fluctuations at specific temporal scales by simply convolving the original light curve with two Gaussian filters (G_{σ_1} and G_{σ_2}) of widths $\sigma_1 = \frac{0.225}{k_p\sqrt{1.0+\varepsilon}}$, where $k_p = \frac{1}{\text{timescale}}$, $\sigma_2 = (1.0+\varepsilon)\cdot\sigma_1$, and $\varepsilon << 1$. The difference between these convolved light curves effectively suppresses all fluctuations outside the space between the "core" (G_{σ_1}) and "annulus" (G_{σ_2}) Gaussians (hence, the Mexican Hat terminology), and the variance of this final filtered light curve is then determined (see Arévalo et al. et al. 2012 and references therein).

For a light curve with gaps, we use a mask M where $M = 1$ for defined points and $M = 0$ for gaps and regions outside the light curve. If we call I a light curve with gaps whose gap values are zero, then $I = M \times I_0$, with I_0 being the complete, gap-free light curve. The light curve and the mask are both convolved with the two Gaussian filters, and the results are divided before computing the final filtered light curve. This approach effectively compensates for data gaps, even those with complex patterns or that cover a substantial portion of the data. For convolution with a Gaussian, i.e., $I_1 = G_{\sigma_1} * I = G_{\sigma_1} * (M \times I_0)$, the resulting amplitudes will decrease near gaps or edges. The convolved mask $M_1 = G_{\sigma_1} * M$ exhibits similar reductions in these areas. Dividing I_1 by the convolved mask M_1 compensates for the amplitude reduction near gaps, thus normalizing the effect of gaps and boundaries. The variance calculation is performed only where the corrected light curve $I_c(k_p)$ has $M = 1$. The flux that spreads beyond the mask boundaries during convolution is offset by a corresponding loss in the mask area near the edges.

Figure 2.2 presents an example light curve and filtered light curves after using the Mexican Hat method. The filtered versions were determined for four different timescales, showing that gaps in the time series and varying sampling rates do not obstruct clean filtering of fluctuations.

In light curves, variability at timescales shorter than the sampling interval ($\Delta\nu$) can cause aliasing, shifting power to lower frequencies and distorting the power spectrum. To minimize aliasing, a point in the light curve must have a minimum number of neighbors within the convolution Gaussian to be included in the variance calculation. Points that lack at least

six nearby neighbors within the filter width are excluded from the variance calculation. This results in the filtered light curves shown in Figure 2.2, where only the densely sampled sections accurately probe shorter timescales.

The variances obtained from filtered light curves, with units of days, are used to estimate the normalized PSD. This is done by multiplying the normalized variances by the peak frequency, denoted as k_p, of each frequency filter in order to derive dimensionless variance estimates. The 'low-resolution' power spectrum is then constructed as the dimensionless variance estimates as a function of peak frequency.

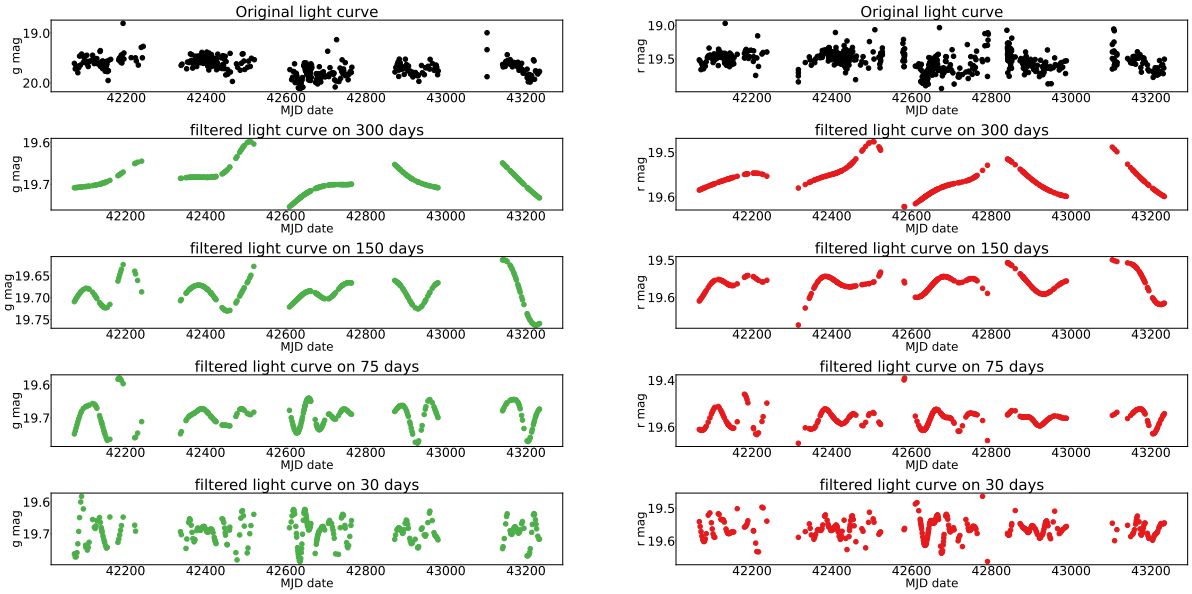

Figure 2.2: The left panel presents the original g-band corrected light curve, followed by the filtered light curves for the four timescales studied. The right panel displays the original r-band corrected light curve, with the filtered light curves for the same timescales shown below.

2.4 Damped Random Walk and C-ARMA process

Kelly et al.(2009) modeled light curves of quasars using a Continuous Time First-Order Autoregressive (CAR(1)) process. The power spectra of this form follow $P(f) \propto 1/f^2$ at high frequencies. The CAR(1) process, also known as a Damped Random Walk (DRW), is a random walk model that incorporates a damping term that moves the value of the system (y(t)) back to its average (mean) value. It has been referred to as a "married drunkard's walk" because, unlike a random walk where the system can move away from its average value, a DRW process always returns to the average value. A differential equation describes this process as follows:

$$\mathrm{d}X(t) = -\frac{1}{\tau}X(t)\mathrm{d}t + \sigma_{DRW}\sqrt{\mathrm{d}t}\varepsilon(t) + b\,\mathrm{d}t, \qquad \tau, \sigma_{DRW}, t > 0 \tag{2.6}$$

Here $X(t)$ is the quasar flux, τ is the relaxation time of the process $X(t)$, and ε is the white noise process with zero mean and variance equal to 1. The process has a mean value of $b\tau$ and a variance of $\tau\sigma^2/2$. The relaxation time can be understood as the amount of time needed for the time series to become roughly uncorrelated, and σ represents the time series variability on timescales shorter than τ.

The PSD of a CAR(1) process can be described as

$$PSD(f) = \frac{2\sigma^2_{DRW}\tau^2}{1 + (2\pi\tau f)^2} \tag{2.7}$$

According to the equation, the CAR(1) process exhibits two distinct regimes in its PSD. For frequencies $f \gtrsim (2\pi\tau)^{-1}$, the power spectrum follows a $1/f^2$ trend. However, for frequencies $f \lesssim (2\pi\tau)^{-1}$, the power spectrum stays constant and resembles white noise. This distinction between the two regimes implies that the relaxation time τ can be considered as a characteristic timescale for the quasar light curves (Kelly et al. 2009).

According to Kelly et al. (2014), the variability in many astronomical sources can be modeled using Continuous-time AutoRegressive Moving Average (C-ARMA) processes. There are two reasons for using C-ARMA processes while modeling stochastic processes. (1) They directly specify the correlation structure of the light curve by providing a differential equation that governs its evolution over time. (2) By allowing for multiple Autoregressive and Moving Average terms, the C-ARMA model provides a high level of flexibility in terms of its PSD shape, which can be adjusted to fit a wide range of observed phenomena. The PSD of a C-ARMA process can be made arbitrarily complex to model a diverse range of physical systems, making it a valuable tool for modeling stochastic variability in astrophysical phenomena.

It has been recently proposed that a Damped Harmonic Oscillation (DHO or C-ARMA(2,1)) can be used to model the AGN UV/optical time variability (Phillipson et al. 2020). A C-ARMA(2,1) has the general form[2]:

$$\mathrm{d}^2\chi + \alpha_1 \mathrm{d}\chi + \alpha_2 \chi = \beta_0(\mathrm{d}W) + \beta_1 \mathrm{d}(\mathrm{d}W), \tag{2.8}$$

where α_1 and α_2 are the autoregressive (AR) coefficients, and β_0 and β_1 are the moving-average (MA) coefficients. W represents a Wiener process which is responsible for incorporating stochasticity into the behavior of χ. Here, χ stands for the brightness of the modeled quasars.

An example of the C-ARMA(2,1) is shown in Figure 2.3. At high and low frequencies, the C-ARMA(2,1) PSD resembles a CAR(1) with the PSD approximately proportional to $1/\nu^2$. However, there is a range of mid-range frequencies where the ν^4 term in the denominator dominates. The lowest frequencies are dominated by the frequency-independent terms, which approach $\beta^2/2\pi\alpha_2^2$. Kepler observations suggest that the PSD is steeper than a CAR(1)

[2]Notice that for specific parameter values a C-ARMA(2,1) shows a Lorentzian-like peak PSD that can be used to represent a QPO.

because ground-based observations may not be sampling at a high enough frequency to observe the ν^4 dominated regime (Kasliwal et al. 2017)).

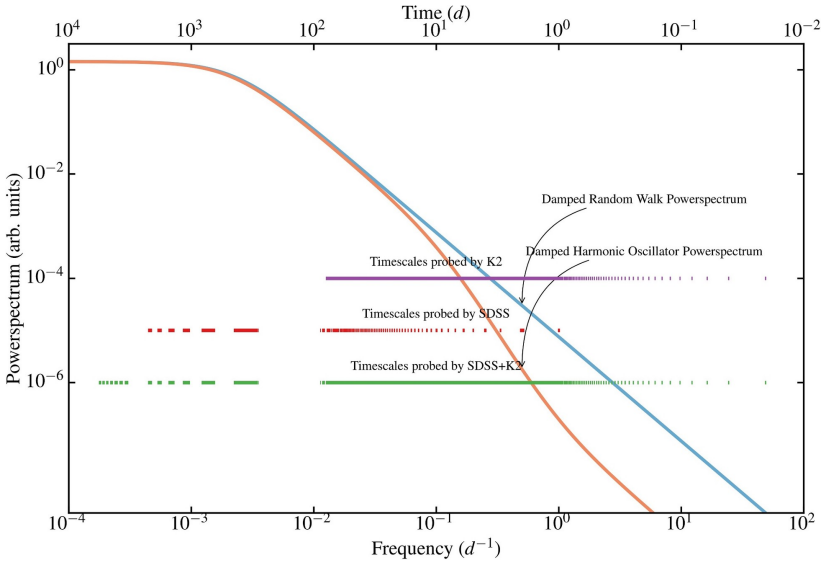

Figure 2.3: The plot compares two PSD models: a DRW model from Kelly et al. (2009) shown in cyan, and a DHO model in orange. The DRW is a C-ARMA(1,0) model, the simplest form of a C-ARMA model, while the DHO is a second-order C-ARMA(2,1) model. Vertical dashed lines indicate the time intervals covered by NASA's K2 mission (purple), the SDSS survey (red), and a hypothetical combination of both (green). For time scales longer than about 10 days, both PSDs exhibit similar behavior, which explains the frequent use of the simpler DRW model for light curves that do not cover shorter time scales. However, with better data in the future, more advanced C-ARMA models will be required. It is important to note that the ZTF survey, which began in March 2018, has a cadence of approximately 4 days and is expected to continue for at least two more years, providing light curves spanning several months to years. LSST, with a high cadence, will span a 10-year survey duration, offering dense, long-term light curves. Credits: Kasliwal et al. 2017).

2.5 Simulating Light Curves

The generation of artificial light curves with known statistical and variability properties helps understand all features introduced by the observation and analysis processing. In this section, we introduce the simulation techniques employed in this thesis to generate synthetic light curves, essential for testing variability models and understanding observational biases. By introducing error and variability patterns, we can assess the impact of different parameters on quasar variability and refine our models to ensure more accurate interpretations of quasar behavior.

Due to spectral leakage in the Fourier transform caused by gaps in observed light curves, it is often challenging to accurately determine fluctuation characteristics from the power

spectrum. Consequently, simulating the optical time series of AGN is necessary to correctly interpret the data or to apply alternative methods for quantifying time variability. Based on the theory of spectral estimation, Timmer & Koenig (1995) introduced an algorithm capable of generating a wide range of non-deterministic linear time series that exhibit a $(1/f)^{\beta}$ spectrum. The core of this algorithm is the randomization of both the phase and amplitude of the Fourier transform, reflecting the stochastic nature of the data. This method can be used to simulate AGN light curves, analyze observed data, and test proposed models.

To generate simulated light curves, we employed the Timmer & Koenig (1995) method, which creates artificial light curves with a specific PSD, preserving the statistical properties observed in real astrophysical data. First, a PSD model, such as a bending power law with parameters for normalization, bend frequency, low and high-frequency slopes, and an additive constant, is defined. A frequency array up to the Nyquist frequency is created, and the corresponding power law is calculated using the PSD model. Complex Gaussian noise is then added to the power law in the frequency domain to simulate realistic noise characteristics based on the PSD model. This noisy power law is transformed back to the time domain using an inverse Fourier transform, resulting in a long light curve that includes both the signal and noise.

Red-noise leakage occurs when the amplitude variations present at small frequencies (long time-scales) is present in short light curves. When obtaining the PSD of such observations the power coming from these variations will appear at larger frequencies (shorter times-scales), distorting the shape of the PSD. To avoid red-noise leakage, simulated light curves are extended by a large factor, and a segment of the desired length is extracted. This segment is normalized to match the mean and standard deviation of the original data light curve if provided. Finally, the appropriate sampling is obtained to reflect the timing properties of the observed data.

In this work simulations were implemented using the python Stingray library. The simulator allows to obtain time series from a power-law PSD, more complex user-defined models or through the implementation of impulses.

2.6 Conclusion

This chapter has outlined essential analytical tools and methodologies used in AGN variability studies. A key statistical description, the Power Spectral Density (PSD) was presented, while the method that will be used in following chapters for PSD estimation, the Mexican Hat filter, was also described. Additionally, we discussed the simulation of light curves to understand data features and further test our modeling. These methods address challenges such as irregular sampling, noise, and stochastic variations in the ZTF optical light curves of AGN, ensuring robust and reliable data interpretation. By presenting these tools and methodologies, this chapter lays the groundwork for the analyses conducted in Chapters 3 and 4.

Chapter 3

Studying the Variability of Quasars as a function of rest-frame wavelength from the Zwicky Transient Facility

The content of this chapter is based on the research published by Patel et al. (2024, in revision).

3.1 Introduction

The variability of quasars in optical light curves can be used to study the physical mechanisms occurring in the accretion disk surrounding a supermassive black hole (SMBH) that is undergoing significant accretion. These quasars predominantly emit radiation in the UV to optical range when observed in their rest frame. Several studies have found that time scales of the variability in the optical and UV wavebands range from days to years (de Vries et al. 2003, McHardy et al. 2006, Sesar et al. 2006, Wilhite et al. 2008, and Kasliwal et al. 2015). It is also well established from a variety of studies, that shorter wavelengths show variability in shorter time scales.

A key characteristic of AGN UV/optical variability is the correlation of light curves over these wavelength range, exhibiting wavelength-dependent time delays. In particular, the light curves of longer wavelengths are observed to lag behind the light curves at shorter wavelengths (Krolik et al. 1991; Stirpe et al. 1994; Ulrich et al. 1997; Collier et al. 1998, 2001; Nandra et al. 1998; Peterson et al. 1998; Kriss et al. 2000). This is explained as reprocessing, where the accretion disk absorbs variable X-ray radiation emitted from a compact region close to the central SMBH and reemits it as UV/optical emission. Thus the accretion disk is illuminated by this variable source. This explains the correlated variability and short time delays observed. In this scenario, the source of variability can be attributed to a central radiation source, which is believed to be the "corona" (Haardt & Maraschi 1991; Chakrabarti & Titarchuk 1995). The delay observed is a result of the time required for light to propagate

from the central region to different radial distances of the accretion disk.

The UV/optical variability of AGN depends on wavelength, showing more pronounced changes at bluer wavelengths (Cutri et al. 1985; Paltani & Courvoisier 1994; Cristiani et al. 1997; Giveon et al. 1999; Hawkins 2003; Vanden Berk et al. 2004a; MacLeod et al. 2010, 2012; Meusinger et al. 2011; Zuo et al. 2012; Morganson et al. 2014; Li et al. 2018; Sánchez-Sáez et al. 2018. This effect is further supported by the observation that AGNs tend to get bluer with increasing brightness. This suggests that emissions with higher variability are usually bluer than less variable emissions (Giveon et al. 1999; Wilhite et al. 2005; Sakata et al. 2011; Schmidt et al. 2012; Wamsteker et al. 1990; Webb & Malkan 2000; Sun et al. 2014).

Adopting a power-law description of the Structure Function (see Chapter 2), $SF(t) \propto t^{\gamma}$, there are disagreements between the correlation of γ and the rest-frame wavelength (λ_{RF}) of the observations, with some studies reporting positive correlations (Li et al. 2018) and others finding no clear relationship (Morganson et al. 2014, Sánchez-Sáez et al. 2018). Using the Bayesian linear regression method proposed by Kelly (2007), Sánchez-Sáez et al. (2018) observed that γ does not exhibit a statistically significant correlation with any SMBH physical parameter. This is evident as the absolute values of the slopes in all regression models are small (less than 0.1) and/or have high errors relative to the measured values. Additionally, for 20.6% of the variable sources in their sample, a Damped Random Walk (DRW) model is inadequate for describing the variability, as γ significantly deviates from the expected value of 0.5. Using a multidimensional fit, Li et al.(2018) found that the γ significantly correlates with the λ_{RF}. Specifically, a $\gamma = 0.089 \pm 0.034$ indicates a notable dependence on λ_{RF}. These conflicting results imply that further research is required. In particular previous sample sizes might have been too small to fully understand the relationship between γ and λ_{RF}. The stochastic nature of AGN implies that average properties help to reduce random noise fluctuations found in individual objects, making large population studies the most useful strategy (Vaughan et al. 2003).

There are some significant challenges when studying the relationship between AGN variability and rest-frame wavelength since variability depends on black hole properties like mass and Eddington ratio. As the temperature stratification of the disk is a function of the black hole mass (M_{BH}) and Eddington ratio ($R_{E\mathrm{dd}}$), and specific regions are observed at specific wavelengths, variability properties might change from object to object for the same λ_{RF} as M_{BH} and $R_{E\mathrm{dd}}$ differ. In order to isolate the dependence of black hole properties, we selected quasars with a narrow range in M_{BH} and $R_{E\mathrm{dd}}$, as explained in the next Section.

This study utilizes the Zwicky Transient Facility (ZTF) light curves obtained from their Data Releases to examine the link between the AGN variability and rest-frame wavelength. Crucially, the study offers some important insights into the AGN variability by analyzing this correlation over various timescales. Previous studies have often focused on single timescales rather than different timescales, resulting in unresolved issues on the connection between variability and wavelength. By employing the broad observational range of ZTF, which can detect variability from a few days to several hundred days, this research addresses these gaps.

The chapter is organized as follows: Section 3.2 provides a description of the sample and the photometric light-curve data, offers a comprehensive description of the methodology, and presents the results of the variability analysis. Section 3.3 provides a statistical analysis that establishes a connection between variability and rest-frame wavelength. Section 3.4 investigates whether some observed variability wiggles in the variance vs rest-frame wavelength plot can be explained by the emission lines and Balmer continuum. Section 3.5 examines the impact of this correlation on the power spectrum and provides insight into the structure of AGN accretion disks. Section 3.6 provides a summary of the main findings.

3.2 Methods

3.2.1 Final Sample

We selected our sample from the catalog of Rakshit et al.(2020), which contains a total of 526,265 SDSS-DR14 quasars. The catalog offers a comprehensive analysis of black hole masses and Eddington ratios, along with other relevant quantities, derived from SDSS spectra. They provided a homogeneous quasar sample in the optical band. The catalog includes selected sources with calculated virial black hole mass values using single-epoch spectra based on two different lines: (a) the Hβ line for sources with redshift less than 0.8, and (b) the Mg II line for sources with redshift between 0.8 and 1.9. Since the single epoch mass estimator obtained from the Hβ line is more reliable, we choose a quasar sample for a wide range of redshift from 0.1 to 0.8. The selected sample includes only quasars that have measurement errors on the black hole mass less than 0.2 dex. To determine the rest-frame wavelength for each quasar, we divided the observed effective wavelengths of the g and r bands (4722.74 Å and 6339.61 Å, respectively) by $(1+z)$. The sample contains the rest-frame wavelength range from 2700 Å to 5200 Å, within the chosen redshift range.

To minimize the impact of black hole mass and Eddington ratio on variability, we have defined a narrow range for these two properties. This range corresponds to the region with the highest density of objects in the M_{BH} vs $R_{E\mathrm{dd}}$ space, enabling the best possible statistical analysis. The selected sample includes black holes with a mass range of $\log M_{BH}$ between 8.0 and 8.5 $\mathrm{M}_{\odot}$, an Eddington ratio range of $\log R_{E\mathrm{dd}}$ between -1.3 and -0.8, and a bolometric luminosity range of $\log L_{bol}$ between 44.85 and 45.83 ergs^{-1}. Figure 3.1 represents this selection through a scatter plot of $\log M_{BH}$ versus $\log R_{E\mathrm{dd}}$, with different redshifts represented by a color map. This plot illustrates the specific criteria within the broader quasar population. Figure 3.2 displays the distribution of $\log M_{BH}$ and $\log R_{E\mathrm{dd}}$ in our selected sample. This selected subset of 7392 quasars enables us to measure the amplitude of variability as a function of rest-frame wavelength, with minimal dependence on other physical parameters. To enhance the reliability of the dataset, we excluded extended objects and focused only on point-like and radio-quiet sources.

Extended objects have been eliminated in favor of point-like sources because using point spread function (PSF) photometry from the ZTF Data Releases to generate light curves would result in inaccurate flux measurements for extended objects. The catalog of Tachibana & Miller (2018) identifies a total of 1687 extended objects leaving a sample 5664 point-lie

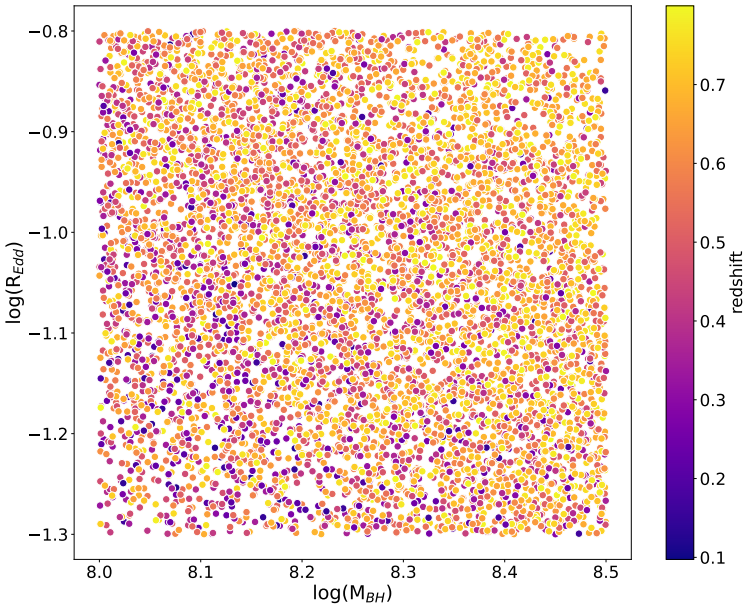

Figure 3.1: Scatter plot illustrating the relationship between the logarithm of the black hole mass ($\log(M_{\rm BH})$, in $M_\odot$) and the logarithm of the Eddington ratio ($\log(R_{\rm Edd})$). Each point represents an individual quasar observation, color-coded by redshift (z).

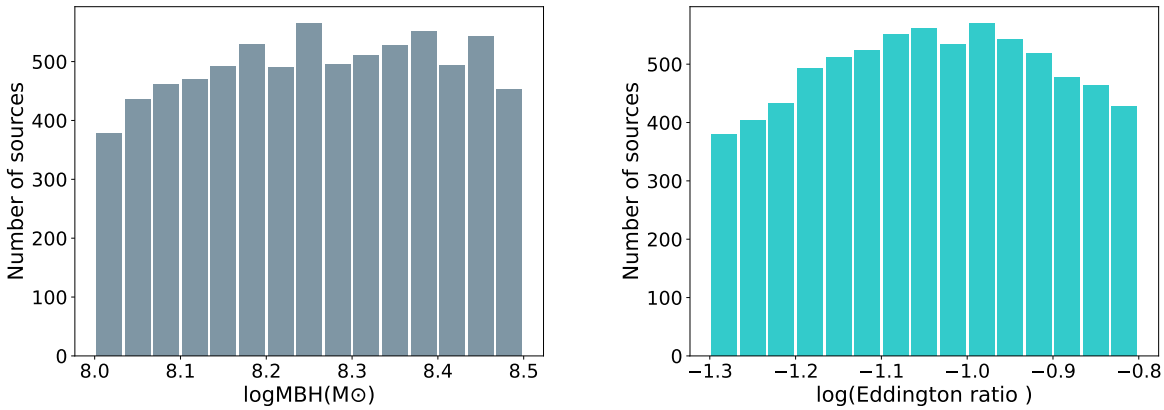

Figure 3.2: Histograms showcasing the distribution of black hole mass ($\log(M_{\rm BH})$) and Eddington ratio ($\log(R_{\rm Edd})$). These plots highlight the narrow range within the selected sample, illustrating the criteria used to minimize the influence of these parameters on variability analysis.

quasars.

Radio-loud quasars often have powerful jets, which can complicate the analysis as they present jet-related variability. Radio-loud quasars show variability amplitudes that are roughly 30% larger compared to radio-quiet objects (MacLeod et al. 2010; Vanden Berk et al. 2004a). We collected 20 cm continuum data from FIRST and NVSS for our final sample. We gave priority to NVSS values for radio flux, using the unified radio catalog of Kimball & Ivezić (2008) when available. The radio-loudness parameter $R_{\rm i}$ was determined using the formula provided by Ivezić et al. (2002), which defines it as the ratio of radio flux density to optical flux density without K-correction. Therefore, the equation for $R_{\rm i}$, which represents the logarithm of the ratio of radio flux (F_{radio}) to optical flux ($F_{optical}$), can be expressed as $R_{\rm i} = 0.4({\rm i} - t)$.

$$\mathrm{R_i} = \log(\mathrm{F_{radio}}/\mathrm{F_{optical}}) = 0.4(\mathrm{i} - \mathrm{t}) \tag{3.1}$$

The equation relates the SDSS magnitude (represented by i) to the AB radio magnitude (represented by t).

$$\mathrm{t} = -2.5\log(\frac{\mathrm{F_{int}}}{3631\mathrm{Jy}}) \tag{3.2}$$

where F_{int} is the integrated flux density.

We identified radio-loud quasars with $R_{\rm i} \geq 1$ based on the criterion established by Ivezić et al. (2002). Figure 3.3 illustrates the distribution of radio-quiet and radio-loud quasars in the sample and their magnitudes. There are 136 quasars classified as radio-loud. After filtering for these objects our sample corresponds to 5528 quasars.

Finally, we excluded objects with any host contribution to minimize the impact of host contributions. There are 553 objects that have significant contributions from their hosts at wavelengths of 4200Å and/or 5100Å, as documented by Rakshit et al. (2020). After filtering for this, the final sample for our study consists 4975 selected quasars.

3.2.2 ZTF data

We extracted data from the ZTF DR15 survey (Masci et al. 2019) which correspond to observations obtained during March 2018 - November 2022 in the g-band and r-band for the selected sample of 4975 quasars (see Figure 3.4). The ZTF DR15 survey consists of light curves that are observed approximately every four days. The data spans a duration of up to four years and eight months, with seasonal gaps occurring on a yearly basis. Most objects had only one observation on a particular night, while a few had multiple observations across a few selected nights. To ensure uniformity in the light curves among different objects, we enforced a requirement for observations to be spaced at least 0.5 days apart in the observed frame. We retained only the first observation from any given night with multiple observations and excluded subsequent data points. This process was applied to create a more standard-

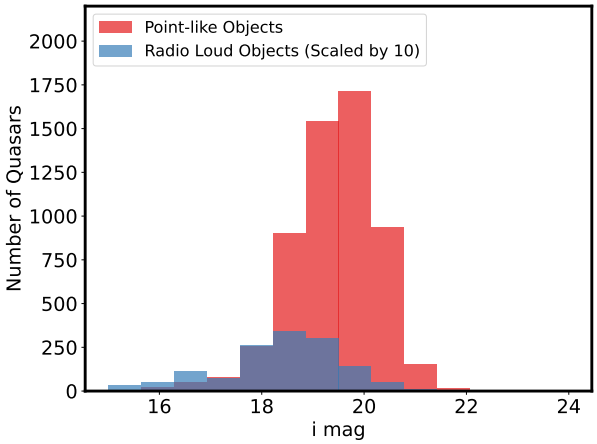

Figure 3.3: A comparison of the number of radio-loud quasars, scaled by a factor of 10, against the total quasar population in our sample as a function of the i-band magnitude.

ized dataset of light curves for various objects. As a result, the cadence, or the timing of observations, became more consistent. Additionally, we eliminate inaccurate measurements by filtering out any instances where the "catflags" parameter is not equal to zero. The catflags value is utilized to identify and omit unusable observation epochs in light curves by flagging overall image and calibration quality issues. Epochs having a catflags value less than 32768 are generally considered usable. For analyses requiring perfectly clean data, it is recommended to select light curve epochs where catflags = 0, ensuring the exclusion of any source-specific issues or bad-pixel information.

ZTF observations utilize a new camera with 16 CCDs, which can lead to cross-calibration offsets. To reduce these uncertainties, we create individual light curves for each CCD, potentially generating multiple light curves for some objects. To improve the quality of each light curve, we exclude observations with a limitmag value of less than 20. This ensures that objects with a magnitude of 20 or less are detected with a significance level of at least 5σ, largely determined by the sky conditions during the observing night. We will limit the sample to only include light curves that are at least 550.0 days long and consist of a minimum of 90 data points. This sample is well-suited for quasar variability research because it enables us to analyze variations occurring over a wide range of timescales, from tens to hundreds of days.

Once the light curves were acquired, the average flux of the filtered ZTF light curves was determined, and objects with a magnitude greater than 20 in both the *g-band* and *r-band* were excluded to ensure a favorable signal-to-noise ratio (5σ).

Our final collection includes 2533 objects in the g-band, with 314 having two good light curves, and 14 having three, and 2795 objects in the r-band, with 353 objects having two acceptable light curves, and 17 having three. This results in 2875 valid g-band and 3182 valid r-band light curves.

In the rest-frame, the g-band light curves that are considered valid have an average du-

ration of 1059 days (with a median duration of 1043 days), and a standard deviation of 120 days. The light curves exhibit an average (median) of 270 (266) good data points, with a standard deviation of 98 data points. The average (median) duration in the r-band is 1052 (1036) days, with a standard deviation of 122 days. The light curves consist of an average (median) of 293 (295) valid data points, with a standard deviation of 95 data points.

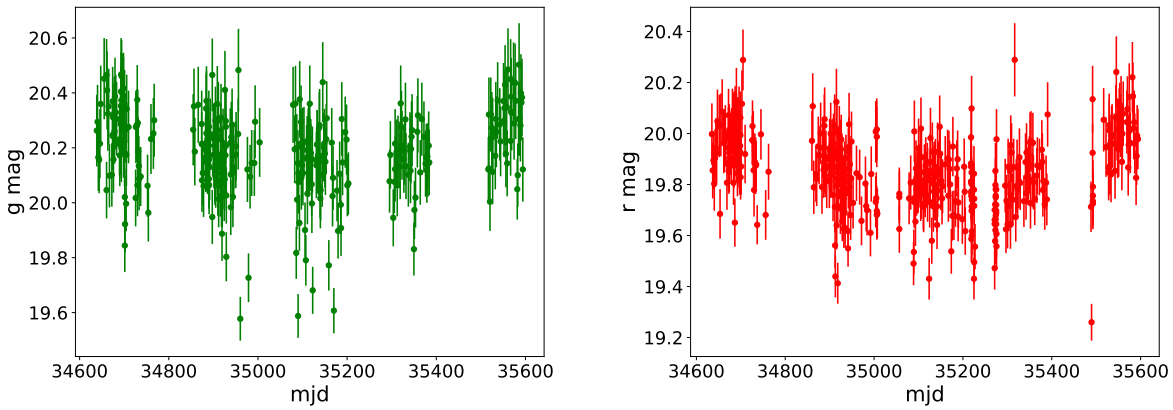

Figure 3.4: This is the corrected light curve for a quasar with RA = 359.786, Dec = 21.122, adjusted for a redshift of z = 0.68.

3.2.3 Variability analysis: Variance Estimation

As described in Chapter 2, the variance of the light curves was computed using the Mexican Hat filter method, a technique that accommodates data gaps commonly present in optical light curves and calculates a normalized variance (or PSD) for effective variability comparison (see Section 2.3 for a detailed methodology). This method involves convolving the light curve with two Gaussian kernels to produce a variance estimate from the filtering over a narrow range in the frequency domain. To take into account variability at different time scales the correlations were obtained across four rest-frame timescales (300, 150, 75 days, and 30 days).

In order to directly determine the variance from the data it is crucial to take into account the amount of Poisson noise present, as this results from uncertainties and not from real variability. It is therefore key, that the photometric errors are well determined.

The accuracy of the photometric noise estimates was validated by carrying out a detailed analysis on a sample of non-variable stars observed with ZTF. A total of 4100 ZTF light curves of individual stars were selected and extracted from the SDSS Stripe 82 Standard Star Catalog stars, as documented Thanjavur et al. (2021). The light curves were selected based on specific magnitude ranges: $16 < g < 20$ and $15.5 < r < 20$, similar to the magnitude range of the quasars. The sample of quasars included in this study encompasses a wide range of redshift values, specifically ranging from 0.1 to 0.8. For consistency, we applied a transformation to the star light curves with eight different redshift values, specifically 0.1, 0.19, 0.28, 0.35, 0.44, 0.53, 0.62, 0.71, and 0.8. This transformation allowed us to align the time axis of the star light curves with that of the quasar light curves in the rest frame. We applied the Mexican Hat filter to estimate the variance of the star light curves across the

four selected timescales in a similar way to the estimation of variation for quasar light curves. This allowed us to estimate the variance associated with observational noise, as mentioned earlier. Finally, the quasar variances were corrected by incorporating in the surplus noise that was calculated from the respective star bins (see Figure 3.7).

Despite our initial expectation of symmetric distributions of the estimated intrinsic variances for the star sample, our observations primarily revealed negative net variances with a few positive ones. When values are negative, it means that noise has been overestimated.

The adjustments to the quasar variances in the *g-band* and *r-band* are depicted in Figure 3.5 and Figure 3.6 respectively, taking into account the outcomes obtained from the analysis of stars. This correction has the strongest effect on the short timescales of variability, as well as objects that have low brightness. The noise-subtracted and corrected variance shall hereafter be referred to as "variance".

After calculating the variance of each quasar, it is important to check that the sample is homogeneous since it includes the black hole mass range ($\log M_{BH}$; $M_\odot$) from 8.0 to 8.5 and the Eddington ratio ($\log R_{E\mathrm{dd}}$) from -1.3 to -0.8, i.e., a variation of 0.5 dex for each parameter. However, this range is sufficient to cause changes in the variability characteristics of the quasars.

We rescaled all systems to a common value of M_{BH}=$10^{8.0}$ $M_\odot$ and $R_{E\mathrm{dd}} = 0.1$ to handle the expected minor differences in variance among quasars with slightly different parameters. We use the scaling relations provided in tables 2 and 3 of Arévalo et al. (2023).

Specifically, in that work, the quasar sample was selected to have a narrow redshift range ($z = 0.6 - 0.7$) in order to control for the wavelength dependency of the emission, but with a $\log(R_{\mathrm{Edd}})$ range of -2 to 0 and a $\log(M/M_{8.5})$ range of 7.5 to 9.5. The quasars were then binned into groups based on their M_{BH}, and R_{Edd} with a bin width of 0.33 dex. For each bin, the median variance, median, M_{BH}, and median R_{Edd} was calculated. The standard errors were estimated using bootstrapping. Then, median variances were determined for four different frequency ranges (corresponding to 30, 75, 150 and 300 days, the same ranges used in this work) by applying the Mexican Hat method.

To determine the linear relationship between variance and mass, i.e., $\log(\mathrm{var}) = a \times \log(M/M_{8.5}) + b$, the study performed Orthogonal Distance Regression (ODR) to fit a linear model to the logarithm of the median variance as a function of $\log M_{BH}$ in each M-R_{Edd} bin. The resulting best-fit parameters a and b were recorded, along with their $1 - \sigma$ errors. Similarly, the relationship was obtained between variance and R_{Edd} i.e., $\log(\mathrm{variance}) = a \times \log(R_{\mathrm{Edd}}/0.1) + b$ by fitting a linear model of the logarithm of the median variance as a function of $\log R_{\mathrm{Edd}}$ for each mass bin (for more details, refer to Section 4 of Arévalo et al. 2023). Linear regression results were used to determine the relationships between the logarithm of variance and the logarithm of the black hole mass (M_{BH}), as well as the logarithm of variance and the logarithm of the Eddington ratio ($R_{E\mathrm{dd}}$). These relationships

were then used to calculate the following equations :

$$\begin{aligned}
\text{rescaled var(300 days)} &= \text{var(300 days)} \times 10^{(0.17\pm0.04)\times(\log M_{BH}-8.0)} \\
&\quad \times 10^{(0.50\pm0.04)\times(\log R_{\rm Edd}+1)} \qquad (3.3)\\
\text{rescaled var(150 days)} &= \text{var(150 days)} \times 10^{(0.37\pm0.05)\times(\log M_{BH}-8.0)} \\
&\quad \times 10^{(0.61\pm0.06)\times(\log R_{\rm Edd}+1)} \qquad (3.4)\\
\text{rescaled var(75 days)} &= \text{var(75 days)} \times 10^{(0.66\pm0.02)\times(\log M_{BH}-8.0)} \\
&\quad \times 10^{(0.81\pm0.07)\times(\log R_{\rm Edd}+1)} \qquad (3.5)\\
\text{rescaled var(30 days)} &= \text{var(30 days)} \times 10^{(1.02\pm0.07)\times(\log M_{BH}-8.0)} \\
&\quad \times 10^{(0.96\pm0.14)\times(\log R_{\rm Edd}+1)} \qquad (3.6)
\end{aligned}$$

In this section, we will explore the different correlations between the rest-frame wavelength (λ_{RF}) and the observed variability features obtained from the ZTF light curves. The quasar rest-frame time series T_{rest} is determined by dividing the observed time sequence, T_{obs}, by the factor $1+z$. Besides, redshift allowed us to carry out the analysis at different rest-frame wavelengths by determining the rest-frame wavelength as $4722.74/(1+z)$ and $6339.61/(1+z)$, with z a different value for each quasar within the 0.1 to 0.8 range.

In our analysis, we considered the final samples as defined in section 3.2.1. To perform median binning, we organized the variance of quasars into 19 bins of equal width, determined by their rest-frame wavelength. The bin median value was used to substitute each value within the rest-frame wavelength bin. We then conducted a filtering step, eliminating bins that did not meet the criterion of containing at least 40 quasars. As a result, our analysis ultimately retained 17 bins.

In order to conduct a more comprehensive data analysis, we have computed variance ratios. A variance ratio is defined as the variance observed over a longer timescale to the variance observed over a shorter timescale. For this determination, we proceeded by organizing the variance ratios into 19 bins of equal width, based on the rest-frame wavelength. We only considered bins that contained 50 or more quasars in order to assure dependability and reduce error propagation. As a result, our analysis ultimately retained 16 bins.

3.3 Dependence of quasar variability on rest-frame wavelengths

3.3.1 Correlations

To examine the connection between variance and rest-frame wavelength across four defined timescales of variability (300, 150, 75, and 30 days), we used the Spearman's rank correlation coefficient (ρ_s) before and after median binning. The correlations between variance and rest-frame wavelength for a total of 2531 sources in the g-band and 2791 sources in the r-band are displayed in Table 3.1 and in Figure 3.8. Before grouping the data into bins, it was observed that the variance at timescales of 300, 150, and 75 days displayed a weak

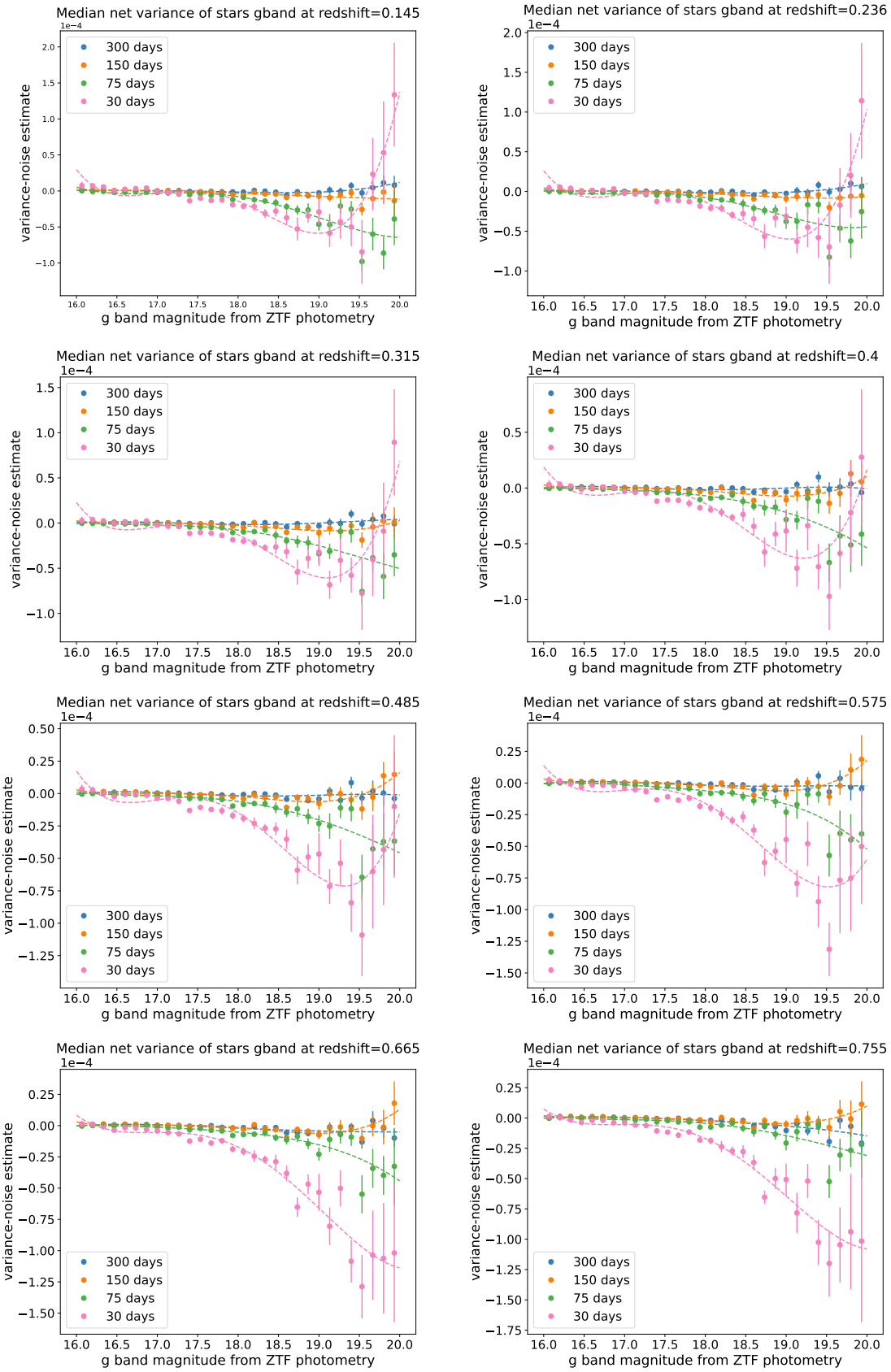

Figure 3.5: Correction to the g-band variance for standard stars across eight redshift bins (from 0.145 to 0.755), over four timescales. Each plot shows median net variance by magnitude with polynomial fits (dashed lines) and error bars calculated via 1000 bootstrapped samples, illustrating the root-mean-squared scatter of these variances.

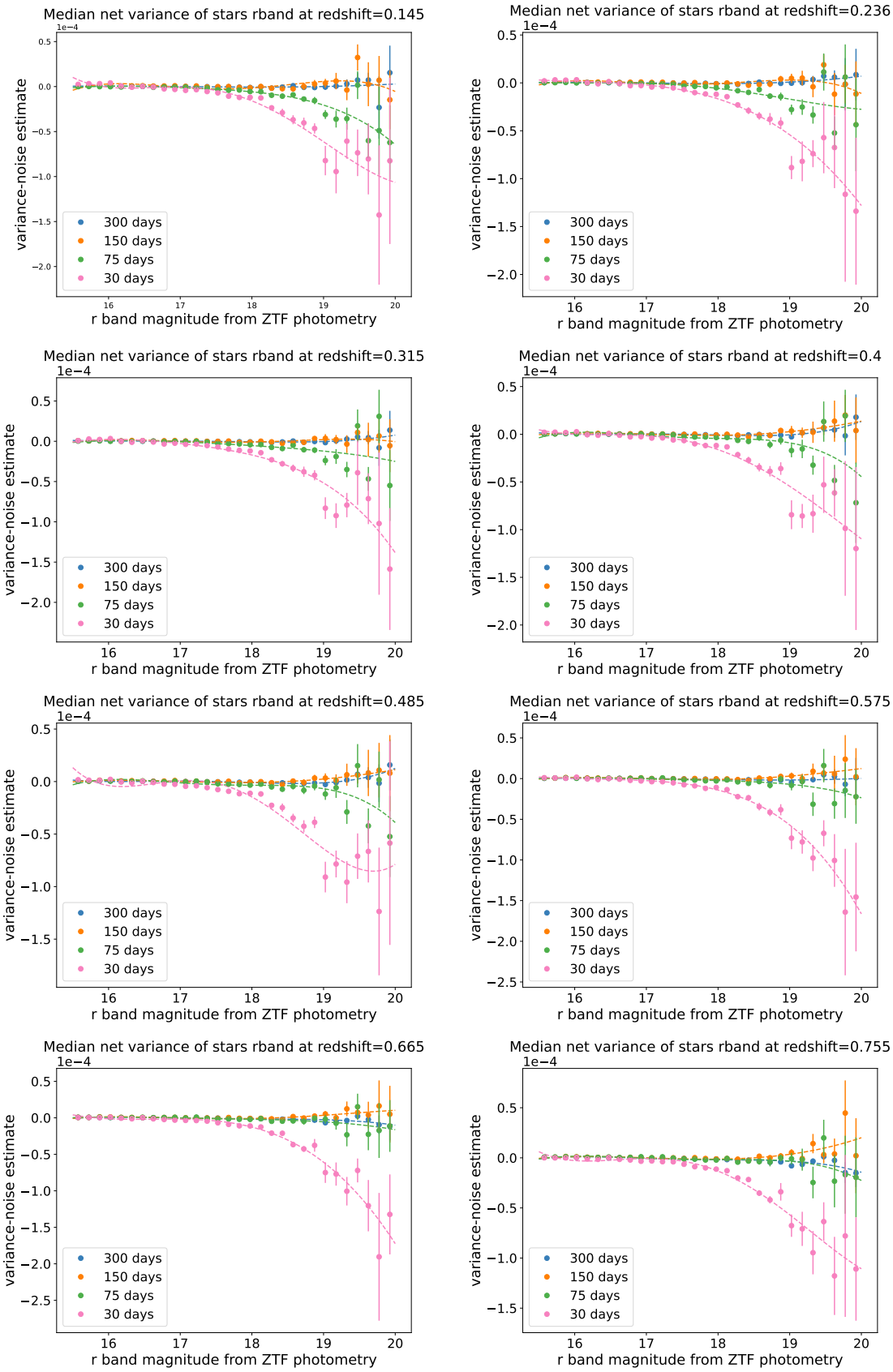

Figure 3.6: Correction to the r-band variance for standard stars across eight redshift bins (from 0.145 to 0.755), over four timescales. Each plot shows median net variance by magnitude with polynomial fits (dashed lines) and error bars calculated via 1000 bootstrapped samples, illustrating the root-mean-squared scatter of these variances.

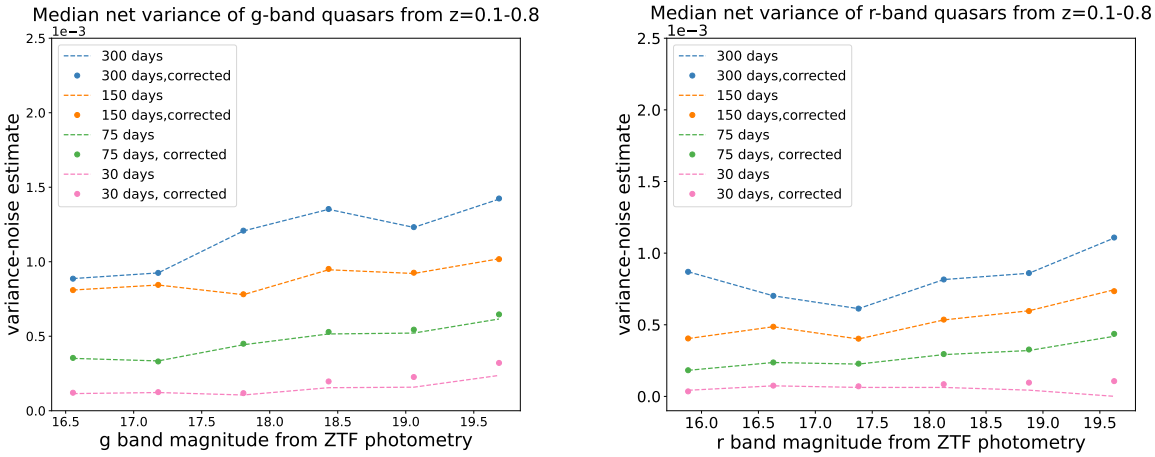

Figure 3.7: This figure displays the median net variances of quasars, illustrated by solid lines, across different timescales as specified in the legend. Following the adjustment for noise estimates, there is a noticeable transition in median variance from the original values (solid lines) to the corrected values, marked by solid circles. The correction for overestimated noise, initially calculated using standard stars, involves adding the "missing variance" needed to adjust the variance of non-variable stars to zero. This adjustment has a significant effect on the median variance, particularly at the shortest timescales.

but statistically significant inverse relationship with rest-frame wavelength. The variance at the timescale of 30 days showed a moderate negative correlation. After median binning was carried out, the correlations between variance and rest-frame wavelength became much stronger and became consistently anti-correlated throughout all timescales. This finding supports previous research that has found inverse correlation between variability amplitude and rest-frame wavelength (Cutri et al. 1985; Paltani & Courvoisier 1994; Vanden Berk et al. 2004a; MacLeod et al. 2010, 2012; Meusinger et al. 2011; Zuo et al. 2012; Morganson et al. 2014; Li et al. 2018; Sánchez-Sáez et al. 2018).

As a next step, we examined the correlations between the variance ratios at 300 over 150, 150 over 75, and 75 over 30 day time-scales and the rest frame wavelength. Spearman's rank correlation was calculated between the logarithm of λ_{RF} and the logarithm of the variance ratios, both prior to and following median binning. These correlations are shown in Table 3.2, and Figure 3.9. The correlation strength between the 300/150 and 300/75 variance ratios showed no significant correlation with rest-frame wavelength before and after binning. On the contrary, in the case of the remaining four variance ratios, we noticed a weak positive correlation with rest-frame wavelength prior to median binning that was statistically significant. The correlations between variance ratios and rest-frame wavelength were found to be significantly stronger after median binning.

The logarithm of the variance ratio can be used as a measure of the power spectral slope, indicating that the power-law slope depends on the rest-frame wavelength. These findings are consistent with those reported by Li et al. (2018) in their study. Li et al. (2018) employed a power-law model to characterize the variability Structure Function, which is represented

Table 3.1: Correlation coefficient (p-value) between log(variance) and log(rest-frame wavelength)

timescale	Unbinned	Binned
300 days	-0.23 (<1e-8)	-0.93 (4e-8)
150 days	-0.24 (<1e-8)	-0.92(1e-7)
75 days	-0.35 (<1e-8)	-0.99 (<1e-8)
30 days	-0.47 (<1e-8)	-0.97 (<1e-8)

Table 3.2: Correlation coefficient (p-value) between log(variance ratio) and log(λ_{RF})

timescale	Unbinned	Binned
300/30	0.17 (<1e-8)	0.74 (2e-3)
300/75	0.05 (1e-3)	0.58 (0.02)
300/150	-0.03 (0.08)	0.04 (0.9)
150/30	0.23 (<1e-8)	0.74 (2e-3)
150/75	0.12 (<1e-8)	0.90 (6e-6)
75/30	0.20 (<1e-8)	0.69 (4e-3)

as $V = A(t/1\text{yrs})^{\gamma}$. It is observed that the logarithmic gradient of variability, denoted as γ, can be expressed as a positive function of the rest-frame wavelength.

3.3.2 Linear Regressions

In order to understand how variance depends on rest-frame wavelength, linear regression was performed. As already described, the variance of quasars was divided into equal-width bins based on the rest-frame wavelength in order to perform median binning. The standard error for the medians was computed using bootstrapping. The bootstrapping procedure involved generating 1000 random samples from the original dataset and the standard deviation of the medians for each bin was determined to find the error estimates. Median bootstrapping sample variance was used to calculate variance.

A linear regression analysis was performed to determine the correlation between the median variance and each rest-frame wavelength bin. This study utilized Orthogonal Distance Regression (ODR) to account for errors in both axes, including errors perpendicular to the line, rather than only considering vertical errors. Figure 3.10 illustrates the variance as a function of the rest-frame wavelength, as shown in the left column. There is a significant decrease in variance as the rest-frame wavelength increases in the four variability timescales. It must be stressed that the observed correlations between variances at specific timescales and rest-frame wavelength are applicable to a black hole with a mass of $10^8 M_{\odot}$ and an Eddington ratio of 10^{-1}.

A significant deviation from linearity is observed across all four time scales in the wavelength range of log(rest-frame wavelength) = 3.50–3.56 and 3.68-3.71 Å. The discrepancy observed could be explained by the particular spectral characteristics in the quasar spec-

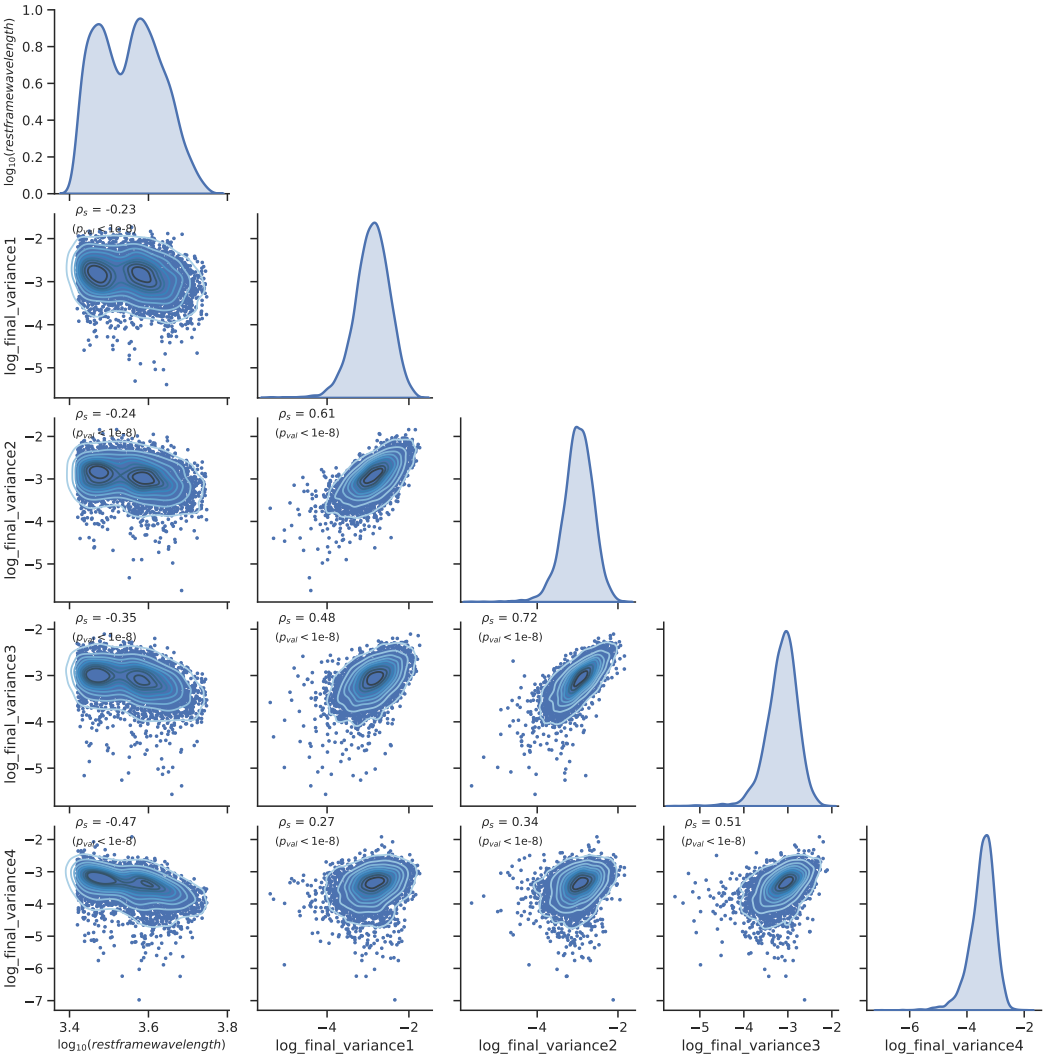

Figure 3.8: Examining the correlations among the variable features of all the final sample quasars before binning. The diagonal represents the individual distributions. We include the Spearman's rank correlation coefficient for each pair of variables as a point of reference. final variance1, final variance2, final variance3, and final variance4 correspond to timescales of 300, 150, 75, and 30 days, respectively.

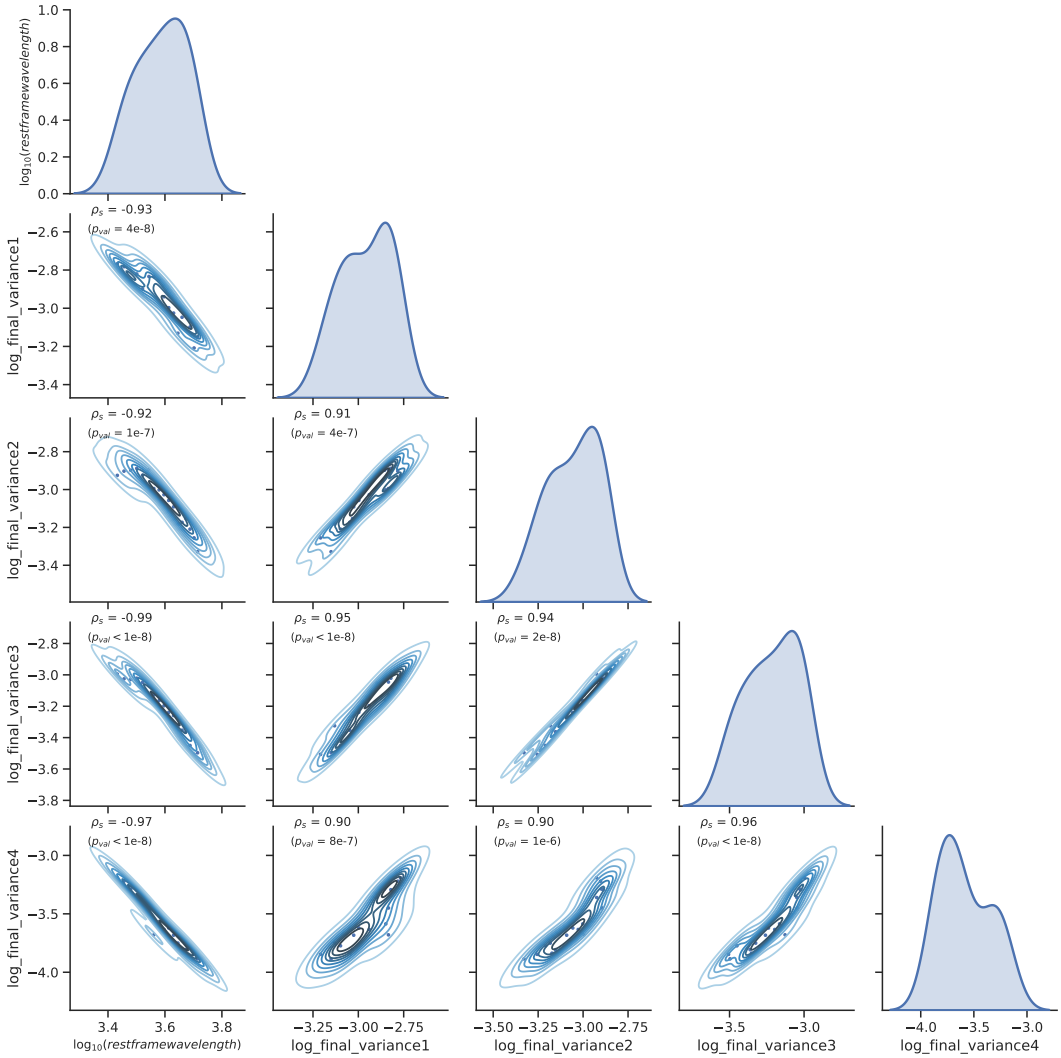

Figure 3.9: Examining the correlations among the variable features of all the final sample quasars after binning. The diagonal represents the individual distributions. We include the Spearman's rank correlation coefficient for each pair of variables as a point of reference. final variance1, final variance2, final variance3, and final variance4 correspond to timescales of 300, 150, 75, and 30 days, respectively.

tra. In Section 3.4, we will investigate how spectral properties may impact the determined variance spectra.

After establishing the linear relationship between variance and rest-frame wavelength, we also conducted linear regression analysis between the logarithm of the variance ratios and the logarithm of the rest-frame wavelength. Figure 3.13 illustrates a significant increase in the variance ratio with rest-frame wavelength. The first column in Table 3.3 (Original Data) displays the regression results for the variance and variance ratio. The table displays the optimal values slope (a) and intercept(b) and their $1-\sigma$ uncertainties.

3.4 Spectral Study

To learn more about the deviations from linearity (wiggles) that appear in Figure 3.10, we study the spectral components falling into the wavelength range of interest. Our sample has rest-frame wavelength intervals in the ZTF g-band and r-band that range from 2700 Å to 4105 Å and 3633 Å to 5200 Å, respectively, for a total wide range from 2700 Å to 5200 Å. This range of wavelengths contains the accretion disk continuum; broad and narrow emission lines, such as Mg II at 2800 Å, Hγ at 4341.68 Å, and Hβ at 4862.68 Å; the Balmer recombination continuum emission; and the Fe II pseudo continuum (very broad spectral features due to many blended Fe II broad lines). When calculating the contribution of emission lines and continuum emission, we must take into account their observed-frame wavelength given by the redshift of each object. These features can shift into or out of the wavelength coverage of the filters, depending on the particular value of z.

The estimated normalized variance is a dimensionless quantity obtained by dividing variance by the square of the mean flux. If the fractional fluctuations of broad emission lines and pseudo-continua is the same as those of the quasar continuum, they act as multipliers in the numerator and the total flux squared in the denominator, resulting in an unaltered normalized variance. On the other hand, if these lines remain constant, they contribute solely to the total flux in the denominator, leading to a reduction in the normalized variance (for more details, see Section 3.5.3). The formula for the largest decrease in normalized variance caused by emission lines and the Balmer continuum is given by a factor $1/(1+f)^2$, where f is the ratio of line flux to quasar continuum flux and is given by:

$$f = \frac{a \cdot (\text{Broad Emission Line Flux}) + b \cdot (\text{flux from Balmer continuum}) + c \cdot (\text{flux from FeII})}{\text{flux from AGN} + \mathrm{d} \cdot (\text{Broad Emission Line Flux}) + \mathrm{e} \cdot (\text{flux from Balmer continuum}) + h \cdot (\text{flux from FeII})} \tag{3.7}$$

Where a, b, c, d, e, and h are constants specific to each band, accounting for the flux contributions of each component in the overall measurement. The values for these constants have been derived from studies that measured the line responsivity (η) for the Balmer lines (Hα, Hβ, Hγ), and Mg II lines (Goad et al. 1999; Korista & Goad 2004) (See Section 3.5).

We determined the f ratio to see if the wiggles we saw in the variance-restframe wavelength

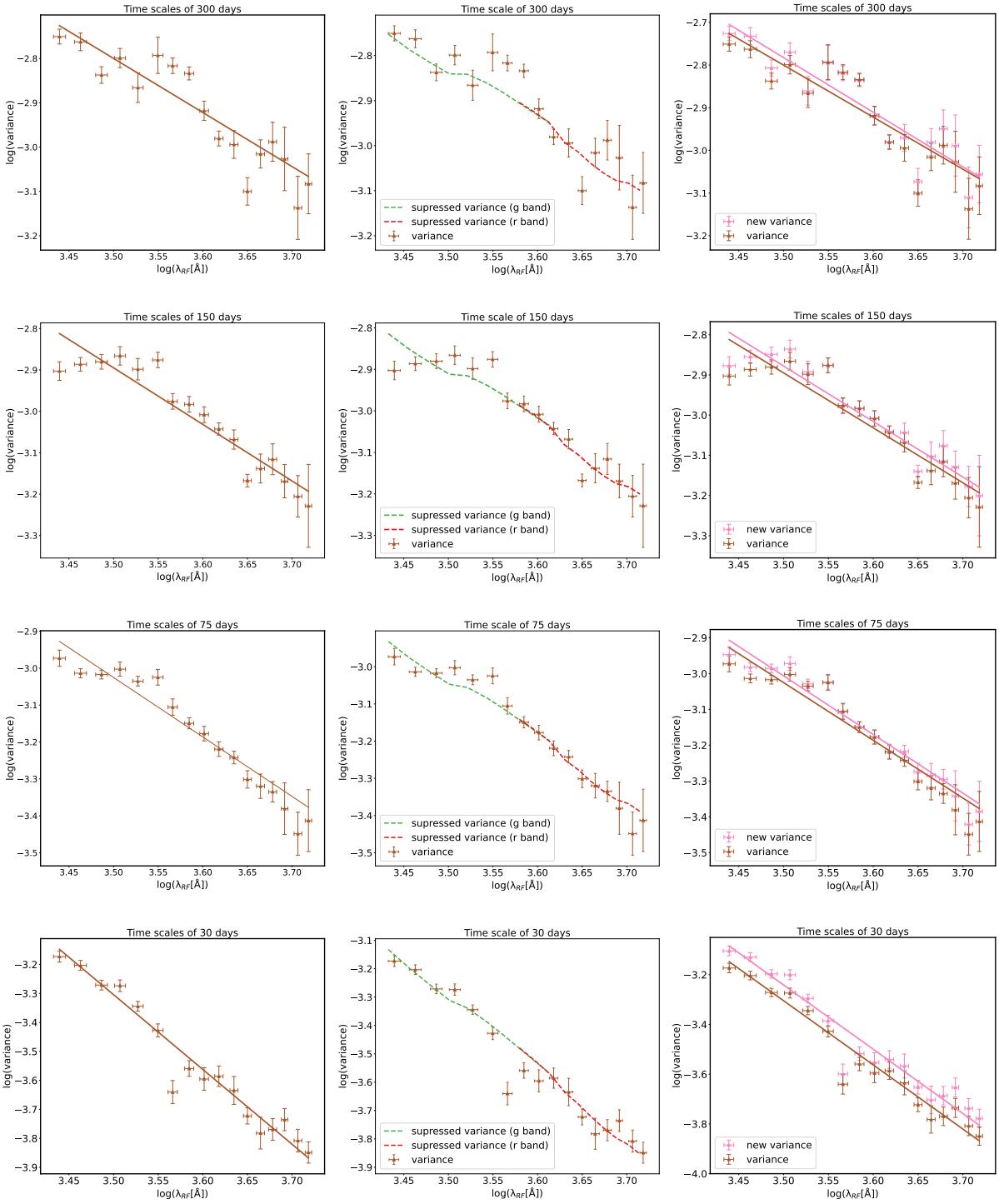

Figure 3.10: The figure compares variance versus rest-frame wavelength for four different variability timescales. In the left column, the original variance is shown, the middle column illustrates the suppression of variance due to emission lines and the Balmer continuum at specific wavelengths, and the right column displays the variance after accounting for this suppression. Each row represents a different timescale: 300 days, 150 days, 75 days, and 30 days. The median net variances, shown with brown and pink triangle-up markers, indicate the values before and after the correction. A significant anti-correlation between median variance and rest-frame wavelength is observed, with linear fits revealing a steeper negative correlation for shorter timescales. The error bars, which depict the root-mean-squared scatter of the median variance, are calculated via bootstrapping with 1,000 re-samples per bin. Detailed information about the correction is provided in Section 3.4 of this thesis.

plot can be replicated by the amplitude and spectral properties of the emission lines and pseudo continua. We chose the SDSS DR14 spectrum spec-3767-55214-0738 from the final group of quasars and used it as a case study. This particular spectrum has signal-to-noise ratio estimate (SNR) of 10 at 5100 and 14 at 3000 . It is located at RA = 143.45 and DEC = -1.71. At a redshift of $z = 0.71$. We chose this spectrum because higher redshift quasars offer an advantage in estimating the Balmer continuum because their spectral features are shifted, which helps in studying a spectral region that is abundant in high-transition hydrogen emission lines. Furthermore, the wavelength range of the spectrum corresponds to the spectral range of the study. Its significantly higher broad emission line equivalent width (EW) in comparison to similar spectra contributes to its importance.

Next, we used the Penalized Pixel-Fitting (pPXF) package (pPXF; Cappellari & Emsellem 2004; Cappellari 2016), which is a spectroscopic fitting tool, to carry out the spectral fitting. The spectral decomposition of the SDSS DR14 spectrum spec-3767-55214-0738 is shown in Figure 3.11. From the fitting process, we can determine the flux corresponding to different spectral components using the g and r filters for different redshift ranges across the sample. This analysis covered continuum, pseudo continuum, and emission lines as given by the following equations:

For the g-band:

$$\mathrm{i}v_g = \frac{4086.68}{1 + z_g} \tag{3.8}$$

$$fv_g = \frac{5521.96}{1 + z_g} \tag{3.9}$$

Where 4086.68 and 5521.96 are λ_{min} and λ_{max} of the g band filter.

The factor $f(g$ band) is defined as:

$$f(g\text{ band}) = \frac{0.68 \cdot (\text{Broad Emission Line Flux}) + 0.32 \cdot (\text{flux from Balmer continuum}) + 0.76 \cdot (\text{flux from FeII})}{\text{flux from AGN} + 0.32 \cdot (\text{Broad Emission Line Flux}) + 0.68 \cdot (\text{flux from Balmer continuum}) + 0.24 \cdot (\text{flux from FeII})} \tag{3.10}$$

For the r-band:

$$\mathrm{i}v_r = \frac{5600.40}{1 + z_r} \tag{3.11}$$

$$fv_r = \frac{7316.69}{1 + z_r} \tag{3.12}$$

Where 5600.40 and 7316.69 are λ_{min} and λ_{max} of the r band filter.

The factor $f(r$ band) is defined as:

$$f(r\text{ band}) = \frac{0.68 \cdot (\text{Broad Emission Line Flux})] + 0.32 \cdot (\text{flux from Balmer continuum}) + 0.76 \cdot (\text{flux from FeII})}{\text{flux from AGN} + 0.32 \cdot (\text{Broad Emission Line Flux}) + 0.68 \cdot (\text{flux from Balmer continuum}) + 0.24 \cdot (\text{flux from FeII})} \tag{3.13}$$

The plot in Figure 3.12 demonstrates the decrease in variability caused by the Mg II emission line ($\sim$ 2800 Å) and the Fe II pseudo-continuum ($\sim$ 2200–3000 Å). We have included the quasar template, which consists of the Broad component, Balmer continuum, and Fe II pseudo-continuum.

The middle column of Figure 3.10 shows broad lines, Balmer continuum, and Fe II pseudo-continuum can account for the suppression of the estimated variance. We included the amount of suppression in the variance estimate and determined a new corrected variance. Our assumption was that significant variability was limited to the continuum emission. Linear regression analysis was again used to fit the new median variance for each rest-frame wavelength bin, as clearly illustrated in the right column of Figure 3.10.

Finally, the new variance estimates were also used to determine variance ratios. Figure 3.13 shows the new variance ratios as a function of the rest-frame wavelength. From now on, the terms 'observed variance' and 'observed variance ratio' will be used in place of 'new variance' and 'new variance ratio'.

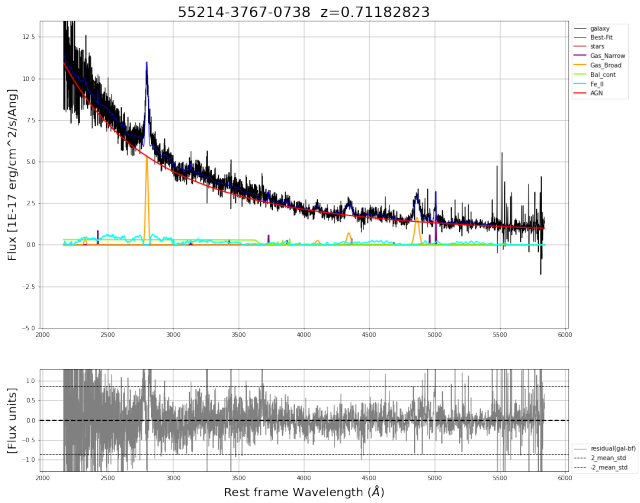

Figure 3.11: Decomposition of the quasar spectrum at z = 0.71. The upper subplot presents the spectral decomposition for a quasar at z=0.71, including the galaxy spectrum (black), the best-fit model (blue), stellar features (indianred), narrow emission lines (purple), broad emission lines (orange), the Balmer continuum (lawngreen), Fe II lines (cyan), and the AGN component (red). The lower subplot shows the residuals (grey) calculated as the difference between the galaxy spectrum and the best-fit model.

3.5 Discussion

In this work, we demonstrated a negative correlation between variance and rest-frame wavelength across four distinct timescales, namely 300 days, 150 days, 75 days, and 30 days. The findings of this study corroborate earlier findings of the inverse relationship between the amplitude of variability and rest-frame wavelength (Cutri et al. 1985; Paltani & Courvoisier 1994; Vanden Berk et al. 2004a; MacLeod et al. 2010, 2012; Meusinger et al. 2011; Zuo et al. 2012; Morganson et al. 2014; Li et al. 2018; Sánchez-Sáez et al. 2018). In addition,

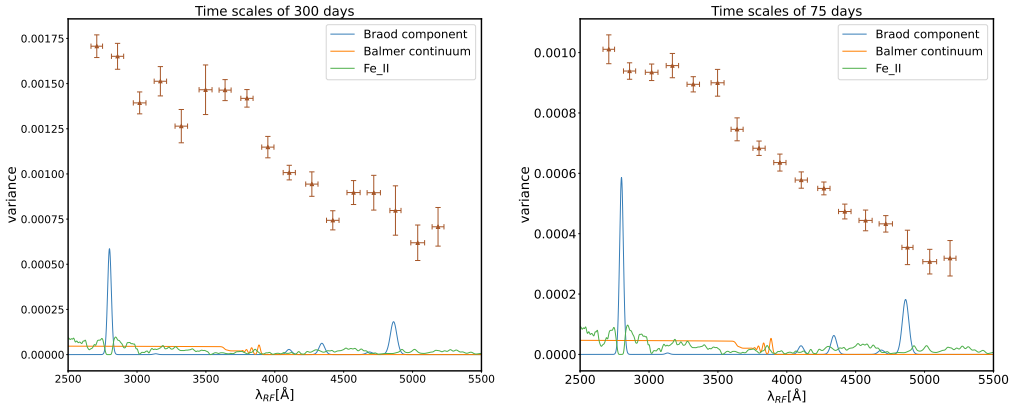

Figure 3.12: The quasar template for the Broad component, Balmer continuum emission, and Fe II pseudo-continuum is overlaid on the variance vs. rest-frame wavelength plot. The two panels show variability amplitudes for 300-day and 75-day timescales, with triangles marking the median values and lines representing the Broad component (orange), Balmer continuum (green), and Fe II pseudo-continuum (cyan).

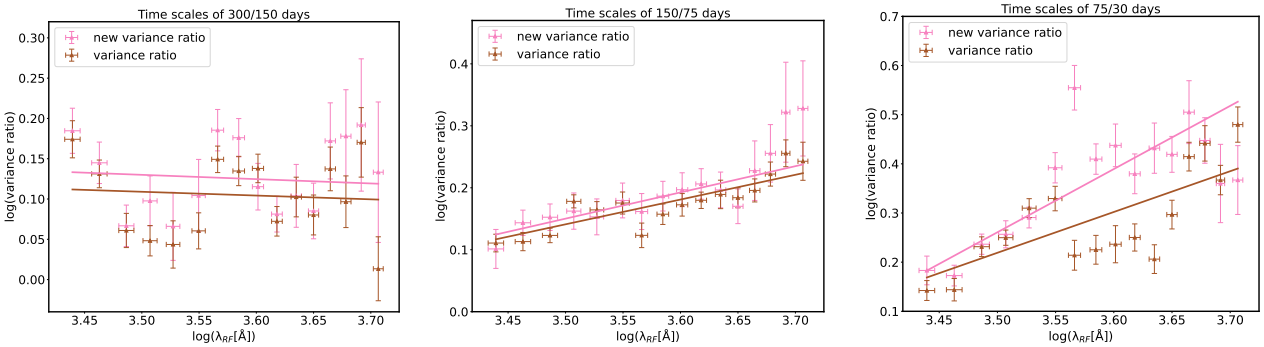

Figure 3.13: The variance ratio as a function of rest-frame wavelength. The median variance ratio of the quasars, with brown and pink markers (triangle up markers), denotes correction. The error bars show the root-mean-squared scatter of the median variance ratio. A linear regression analysis shown as solid lines was used to investigate the relationship between variance ratio and rest-frame wavelength.

Table 3.3: Best-fit values for slope (a) and intercept (b) obtained from linear regression using λ_{RF} as the independent variable. The columns include: 'Original Data' (linear regression applied to the initial variance and variance ratio), and 'Corrected Data' (linear regression applied to the new variance and new variance ratio, incorporating estimated variance suppression.)

	Original Data		Corrected Data	
timescale	a	b	a	b
variance(300 days)	-1.22 ± 0.18	1.47 ± 0.63	-1.28 ± 0.15	1.70 ± 0.54
variance(150 days)	-1.37 ± 0.16	1.89 ± 0.58	-1.38 ± 0.14	1.95 ± 0.49
variance(75 days)	-1.61 ± 0.13	2.61 ± 0.45	-1.64 ± 0.10	2.72 ± 0.36
variance(30 days)	-2.58 ± 0.13	5.73 ± 0.45	-2.58 ± 0.15	5.80 ± 0.52
variance ratio(300/150)	-0.04 ± 0.16	0.25 ± 0.56	-0.05 ± 0.17	0.32 ± 0.60
variance ratio(150/75)	0.40 ± 0.07	-1.25 ± 0.25	0.42 ± 0.07	-1.33 ± 0.26
variance ratio(75/30)	0.83 ± 0.20	-2.69 ± 0.70	1.29 ± 0.20	-4.24 ± 0.72

Note: Observed data are reported to two decimal places, reflecting measurement precision.

the we have found that the strength of this anti-correlation is more pronounced for shorter timescales.

3.5.1 Anti-correlation between Variance and Wavelength

The outcome from our study is an observed anti-correlation between variability and wavelength in Active Galactic Nuclei (AGNs). This relationship, where variability decreases with increasing wavelength, suggests that the shorter, bluer wavelengths are inherently more variable than the longer, redder wavelengths.

The observed negative correlation shows that as the radius of the accretion disc increases, the optical fluctuations at various timescales become less prominent. This phenomenon is particularly noticeable when examining shorter timescales. In other words, the damping of the variability occurs faster at shorter wavelenghts. Additionally, the study revealed that the amplitude of variability is greater at longer timescales when compared to shorter timescales within the rest-frame wavelength range of 2700 Å to 5200 Å, something expected because of the red-noise nature of AGN variability. The normalized variance is plotted in Figure 3.14 as a function of λ_{RF}, where the x-axis is corresponds to $\log(\lambda_{\rm RF})$.

The starlight from a host galaxy is constant over typical AGN variability timescales, but it can dilute variability normalized by total flux due to its redder intrinsic emission compared to the AGN. However, our sample contains objects with minimal host galaxy emission which is reported in the catalog of Rakshit et al. 2020. Therefore, the contribution from the host galaxy (stellar contamination) should not be significant and the observed variability patterns are driven by intrinsic AGN processes rather than the host galaxy.

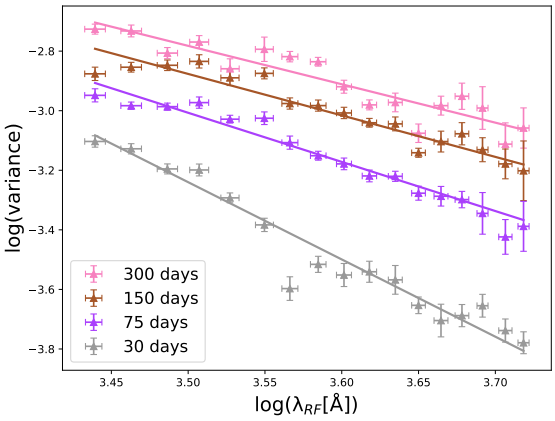

Figure 3.14: The normalized variance as a function of λ_{RF} for four studied timescales. The observed median variance is indicated by upward triangles, showing the corresponding errors. The straight line represents the linear regression fit, with different colors denoting different timescales. The variability amplitude is greater at smaller radii, and this effect is more pronounced on shorter timescales.

3.5.2 The Impact on Power Spectra

The PSD of a variability process provides a useful description of the flux variations across different frequencies or timescales. Existing research usually adopt a damped random walk (DRW) model to describe the PSD of AGN, which mimics a random walk pattern at higher frequencies ($P(f) \propto 1/f^2$) and transitions to a plateau at lower frequencies ($f < f_b$). The

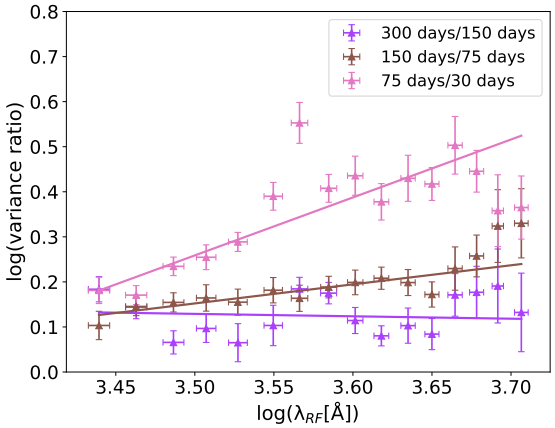

Figure 3.15: The variance ratio is plotted against rest-frame wavelength. Upward triangles denote the observed median variance ratios with their respective errors. Error bars shows the root-mean-squared scatter of the median variance ratio. Solid line represents the linear regression fit, and different colors denote different variance ratios.

frequency at which this transition occurs, denoted as f_b, relates to a damping timescale $\tau_{damp} = 1/f_b$.

Adopting a bending power-law model allows a more general representation of the PSD, and allows to directly determine for both its low- and high-frequency slopes. Please refer to Figure 3.16 for visual representation. A recent study by Arévalo et al. (2024) found that combinations of high-frequency slope (α_H) and low-frequency slope (α_L), such as α_H = -3 and α_L = -1, as well as α_H = -2.5 and α_L = -0.5, provide a good fit for quasars with $7.5 < \log(M_{BH}/M_\odot) < 9.5$ and $-2 < R_{Edd} < 0$, at a fixed rest-frame wavelength of approximately 2900 Å. On the other hand, the damped random walk (DRW) model with $\alpha_H = -2$ and $\alpha_L = 0$ does not provide a fit of the same quatlity. In what follows we will adopt a bending power-law with indices α_H = -3 and α_L = -1 as the best possible representation of a quasar PSD. Additional evidence of a deviation from the power law at lower frequencies has been proposed by Stone et al. (2022). However, further data with longer temporal baselines is required to validate this hypothesis.

Research by Burke et al. 2021 established a relationship between τ_{damp} and black hole mass, finding that $\tau_{damp} \propto 107^{+11}_{-12} \times (M_{\rm BH}/10^8 M_\odot)^{0.38^{+0.05}_{-0.04}}$ days for a particular wavelength $\lambda_{RF} = 2500$ Å, closely matching the starting wavelength of 2700 Å of our study. Furthermore, Arévalo et al. (2024) not only found that the break frequency scales with M_{BH} to the power of -0.55, but also that there is a dependency with accretion rate R_{Edd} to the power of -0.35. Using these later results (see Eq. 2 and Tables 3 and 4 in Arévalo et al. (2024)), we find that adopting the model with $\alpha_H = -3$ and $\alpha_L = -1$, the break frequency for our chosen mass and accretion rate is estimated to be 96^{+9}_{-2} days at 2900 Å, again quite close to the bluest wavelength considered in this work ($\sim$ 2700 Å).

Our investigation uncovers a negative correlation between observed variance and rest-frame wavelength, formulated as $\log(variance) = a \times \log(\lambda_{RF}) + b$ (see Figure 3.10 and Table

3.3). This indicates an increase in power spectrum normalization with decreasing λ_{RF}. However, this relationship varies across different timescales, suggesting a more complex relation than a mere vertical shift in the variance curves would imply. Notably, variance at shorter timescales exhibits a steeper slope compared to longer timescales. Figure 3.15 shows an approximately constant value for the variance 300/150 ratio as a function of λ_{RF}, indicating a flat dependence at these timescales. The 75/30 ratio exhibits a robust and statistically significant positive correlation. In our study, we performed linear fits to analyze the relationship between the logarithm of the variance ratio and the logarithm of the λ_{RF} values as $\log(\text{variance ratio}) = a \times \log(\lambda_{RF}) + b$. The results of these fits can be found in Table 3.3. Figure 3.15 displays the linear fits for the binned data, in addition to the corresponding data points. The observation that the slope of the relationship between variance and wavelength increases for shorter-timescale fluctuations indicates that the power spectral shape, in addition to its normalization, is a function of wavelength.

Figure 3.17 shows the low-resolution power spectra (Power $\times$ frequency) for different $\lambda_{\rm RF}$ bins in different colors. In all panels, the $\lambda_{\rm RF}$ dependence becomes obvious, where higher $\lambda_{\rm RF}$ correspond to lower normalization and increasingly steeper slopes, though the steepness is less evident. This visual evidence clearly illustrates the trends described earlier.

MacLeod et al. (2010) and Stone et al. (2023) found a dependence of the damping timescale with λ_{RF}, which can be represented as $\tau_{damp} \propto \lambda_{RF}^{B}$. With B values reported as 0.17 ± 0.02 and 0.43 ± 0.10 respectively, there is a consensus that longer wavelengths present larger τ_{damp}, corresponding to smaller f_b values. This behavior is consistent with the observations in Figure 3.17, which show that the power spectra steepen with increasing wavelength, indicating that the break frequency shifts to lower values for longer wavelengths. This wavelength-dependent shift in f_b could account for the differing variance relationships with wavelength observed across timescales. The gradual shift of the PSD around f_b, along with its vertical displacement based on wavelength (refer to Figure 3.16, where the position of f_b is indicated by a blue star for $\lambda_{RF} = 2700$ Å and a red star for $\lambda_{RF} = 5200$ Å), may result in varying variance-wavelength dependencies across different timescales. We can experimentally verify this.

Our findings indicate a decrease in power from the blue to the red end of the wavelengths we studied. Specifically, we observed a decrease of approximately 0.33 dex for a 300 day timescale. Similarly, for timescales of 150, 75, and 30 days, we observed drops of approximately 0.33, 0.44, and 0.68 dex respectively between the same two wavelengths (refer to Figure 3.14). We will examine whether these changes in variance align with a distinct bending power-law PSD and a wavelength-dependent f_b. The decrease of 0.33 dex over a period of 300 days establishes a normalized ratio of the Power Spectral Densities for two specific wavelengths, $\lambda_{RF} = 2700$ Å and $\lambda_{RF} = 5200$ Å, as shown in Figure 3.16. The frequency correponding to 300 days corresponds to the lowest frequency (longer timescale) that we can observe. By choosing a timescale long enough the PSD should remain largely unaffected by the break frequency, as hinted by the consistent slope observed in the variance ratio between 300 and 150.

By utilizing a bending power-law expression for the PSD, it is found that variance is inversely proportional to $(f(1+(f/f_b)^2))^{-1}$, assuming $\alpha_H = -3$ and $\alpha_L = -1$. Additionally, the variance ratio at a specific frequency f for two different wavelengths is given by $A^{\rm red}(1+(f/f_b^{\rm blue})^2)/A^{\rm blue}(1+(f/f_b^{\rm red})^2)$, with $A^{\rm red}$ and $A^{\rm blue}$ representing the normalizations of the PSDs. It has been previously shown that the value of f_b is 1/96 days^{-1} at the blue end ($\lambda_{RF} = 2700$ Å), and it is estimated to be approximately 1/107-1/130 days^{-1} at the red end ($\lambda_{RF} = 5200$ Å), based on MacLeod et al. (2010) and Stone et al. (2023). By incorporating the normalization difference (0.33 dex) for the PSDs associated with the shortest and longest wavelength ranges at 300 day timescales, we obtain the expected variance difference at $\lambda_{RF} =$ 5200 Å to be approximately 0.51 dex for the 75 day timescale and 0.58 dex for the 30 day timescale. To maximize the changes in variance, we assume a $f_b = 1/130$ days^{-1}. Thus, the relationship between f_b and wavelength can account for the fluctuations observed over 75 day periods, but it does not fully explain the decrease in variance seen over the 30 day timescale.

To interpret the observed variations in variance and variance ratios, as indicators of the PSD slopes, it is crucial to consider how the f_b varies with wavelength. However, our analysis also suggests the need for a modification in the PSD slope at frequencies higher than f_b to fully account for the behaviors seen at the highest frequencies. A more precise assessment of how f_b changes with wavelength is essential, especially since previous studies by MacLeod et al. (2010) and Stone et al. (2023) were based on a DRW model. Our findings also reveal that for frequencies below the f_b, disk variability across different wavelengths appears to be modulated merely by changes in normalization for timescales up to 300 days. Conversely, above f_b, we observe a wavelength-dependent chromatic effect that alters the PSD shape.

3.5.3 Impact of Continuum Changes on Emission-Line

Understanding the impact of continuum changes on emission-line and pseudo-continuum variability can help to better explain the deviations observed in the variance plots (Figure 3.10). According to previous studies, if changes in the continuum have a linear effect on the emission-line gas locally (Goad et al. 1999; Korista & Goad 2004; Goad et al. 2012), line responsivity η, as defined by Goad et al. (1993), relates line emissivity to the ionization parameter, i.e., with the distance from the ionizing source for a given electron density. Higher η values indicate greater responsiveness to continuum fluctuations. Typically, high-ionization emission lines have $\eta \sim 1$, Balmer lines (Hα, Hβ, Hγ) have $\eta \sim 0.6$, and Mg II lines have $\eta \sim 0.2$ (Goad et al. 1999; Korista & Goad 2004). Consequently, Mg II and Fe II lines exhibit weak variability (Kokubo et al. 2014). The Balmer pseudo-continuum is likely formed by specific photoionization processes in the broad line region (Yip et al. 2004). Variability in the Balmer pseudo-continuum is significantly stronger compared to the Mg II and Fe II pseudo-continuum (Kokubo et al. 2014).

In order to reproduce the features observed in the variance spectrum, particularly below $\lambda_{\rm RF} = 4000$ Å, we had to assume that all components other than the emission from the accretion disk had to present no flux variations. Figure 3.12 shows that below $\lambda_{\rm RF} = 4000$ Å several emission components are present, as required to explain the spectral wiggles. However, the studies just mentioned suggest that some of them are significantely variable. Spectral

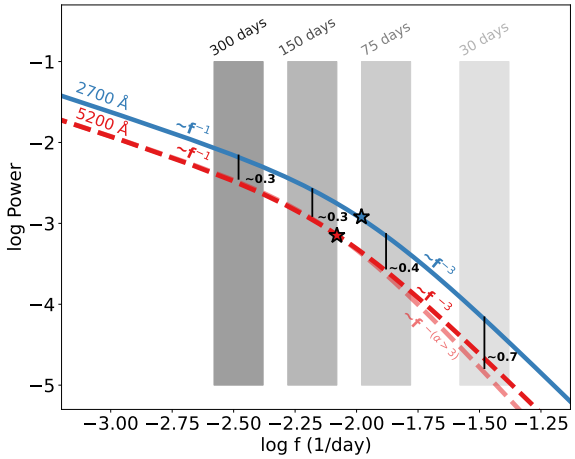

Figure 3.16: The figure demonstrates the variation of power spectral models with rest-frame wavelength for quasars with a consistent black hole mass and Eddington ratio. It indicates that higher rest-frame wavelengths are associated with lower normalization in the power spectrum. A significant trend is observed in the dependence of variance on rest-frame wavelength (λ_{RF}) over shorter timescales. This trend could be partially explained by an inverse relationship between the break frequency (f_b) and λ_{RF}. However, if f_b were the sole factor influencing variance based on wavelength, we would expect a consistent decline in variance at both 75 and 30-day timescales, which is not supported by the data. Thus, the observed variance trends suggest a more complex interaction: a steeper slope at higher λ_{RF}, along with a decrease in the break frequency at these wavelengths, is necessary to comprehensively explain the quasar variability observed, as depicted by the dashed-line spectrum in the figure.

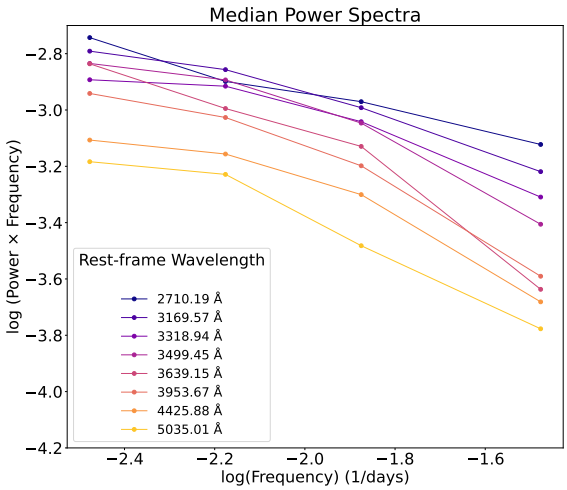

Figure 3.17: Power spectra (Power × frequency) at various $\lambda_{\rm RF}$ are represented by different colors, focusing on low-resolution. The markers indicate the median variance of all quasars in each $\lambda_{\rm RF}$ bin and temporal frequency for each bin, obtained through bootstrapping the samples. The frequencies are expressed in units of day^{-1}. The normalization is affected by rest-frame wavelengths, and the power spectra appear to become steeper as the wavelengths increase.

inhomogeneities in our sources might also account for some variance deviations as orientation and BLR dynamics and spatial distribution can impact the observed line emissivity.

3.6 Conclusions

In this study, we explored the relationship between the variability of the quasar ensemble and the wavelength in its rest frame using a sample characterized by a mass of 10^8 $M_\odot$ and an Eddington ratio of 10^{-1}. By choosing this specific range of black hole mass and Eddington ratios, we can clearly differentiate the impact of wavelength on variance from its connection to these black hole parameters. Our research investigates the fluctuations of quasars over different time values (300, 150, 75, and 30 days) and at a wavelength range of approximately 2700 - 5200 Å in the rest frame. Here are the key findings from this study:

1. There is an inverse relationship between the quasar variance and the rest-frame wavelength, when the black hole mass is held fixed at $10^8 M_\odot$ and Eddington ratio of 10^{-1}. These results provide further evidence in line with previous research (e.g., Li et al. 2018; Sánchez-Sáez et al. 2018).
2. We present new linear equations that establish a relationship between variance and rest-frame wavelength across four distinct timescales, ranging from 30 to 300 days in the rest-frame of quasars. The linear connection, for instance, has a slope of -1.29 ± 0.15 and an intercept of 1.73 ± 0.55 for a 300-day timescale, and a slope of -2.59 ± 0.14 and an intercept of 5.84 ± 0.51 for a 30-day timescale. The variance shows a noticeable decrease as the rest-frame wavelength increases, and this decrease becomes more pronounced for shorter time scale fluctuations.
3. We observed a strong positive correlation between the variance ratio and rest-frame wavelength and a flat dependency for the 300/150-day timescale. This finding supports

the previous research by Li et al. (2018).

4. Our findings indicate that a PSD described as a bending power-law with a wavelength dependent break frequency is not enough to explain the observed change in slope for different time scales. Instead, it appears that the steepness of the power spectrum above the break frequency becomes more pronounced as the wavelengths get longer.

In this study, ZTF DR15 light curves were utilized, with a cadence of roughly four days and a duration of 4 years and 8 months, accounting for yearly gaps. As a result, it was not possible to obtain variance on timescales shorter than 30 days or longer than 300 days. Our findings contribute to determine the characteristics of accretion disc variability and have the potential to be continued with the Legacy Survey of Space and Time data (LSST, Ivezić et al. 2019). LSST will offer frequent and long-term observations across a wide range of wavelengths, spanning from the near-ultraviolet to the near-infrared. Expanding this project to incorporate the Deep Drilling Fields, which boast a higher cadence, holds great promise for advancing our comprehension of AGN short-timescale variability. Specifically, variance estimation over many timescales and more wavebands would be possible with such a dataset, which would offer more accurately constraints to comprehend the processes underlying the variability of the accretion disk.

Chapter 4

CHAR model

The content of this chapter is based on the research published by Patel et al. (2024, in revision).

4.1 Introduction

Time-dependent physical models are necessary to account for AGN variability. The Corona Heated Accretion Disk Reprocessing (CHAR) model takes into account the time-dependent evolution of the standard thin accretion disk model, as proposed by Shakura & Sunyaev (1973 – SSD), to describe temperature fluctuations. The CHAR model, as proposed by Sun et al. (2020a), describes a link between disk fluctuations and observed variability. This model successfully replicates the variability seen in SDSS quasars (Sun et al. 2020b; Chen et al. 2024).

In the CHAR model, the magnetic field plays a fundamental role. The accretion disk and the corona are magnetically coupled and magnetic waves are responsible for propagating fluctuations from the center of the system outwards. Although the CHAR model does not solve for the magneto-hydrodynamics of the system and simply characterizes the magnetic variability assuming a power-law distribution of fluctuations, it offers a framework that is able to reproduce many observed properties of AGN variability despite its simplicity. Some details of this setup are given below.

Supermassive black holes (SMBHs) often gather material from their surroundings, such as the hot gas released by stellar winds. This gas does not have to align with the plane of the disk and can instead create a heated accretion stream encircling the disk. The flow struggles to cool off effectively to release heat efficiently, resulting in a spatially expanded, or geometrically thick, structure. Closer to the black hole, the magnetic fields amplified near the disk midplane rise toward the surface due to magnetic buoyancy (Parker 1966, Miller & Stone 2000). Once they reach this region, they can undergo effective amplification, leading to the formation of large-scale poloidal (along the axis of rotation) fields (Rothstein & Lovelace 2008).

In the vertical regions of an accretion disk, highly magnetized fields can undergo magnetic reconnection, dissipating magnetic energy and heating the surrounding low-density plasma (e.g., Di Matteo 1998; Liu et al. 2002). This process leads to increased plasma temperatures when compared to the accretion disk due to its lower surface density for the same accretion rate (Jiang et al. 2014). Near a SMBH, energy dissipation primarily heats protons in the low-density environment, where protons and electrons are largely decoupled, making Coulomb coupling inefficient (Di Matteo 1998; Różańska & Czerny 2000). The accreting plasma has higher proton temperatures since viscous dissipation transfers more energy to heavier protons, which radiate slower than electrons. This results in "radiatively inefficient" plasma, addressing the energy-budget issue of the X-ray reprocessing model and resembling advection-dominated accretion flows where energy is advected inward rather than radiated away. This mechanism would form the corona. The corona is situated in the inner regions ($< 10R_s$), and it is considered that it has negligible contribution in the UV/ optical region.

As the magnetic field of the corona experiences fluctuations, it results in magnetic variations. These will be quantified by the $Q^+_{\rm mc}$ power term. Different from the cooler, thinner SSD disk, the corona exhibits a much faster rate of material flow towards the black hole. This is because the gas in the corona is hotter, and mechanisms like the magnetorotational instability (MRI) generate viscosity which effectively transfer angular momentum. This allows material to spiral inward quickly and converts gravitational energy into magnetohydrodynamic (MHD) turbulence. This rapid movement means that magnetic fields anchored in the corona are pulled towards the black hole along with the inflowing gas. In contrast, the magnetic fields extending into the colder, denser disk below do not move significantly because the disk material flows inward more slowly. The hotter, faster-moving gas in the corona, coupled with the slower inward flow in the cooler disk, creates conditions where magnetic fields can connect and interact between the corona and the broader, cooler disk surrounding it, leading to a magnetic connection between the corona and the broader, cooler disk surrounding it. Because of this magnetic coupling, MHD fluctuations propagate into the accretion disk and generate coherent MHD turbulence. This turbulence subsequently dissipates which causes the change in the heating rate. Consequently, variations in the disk heating rate lead to fluctuations in the accretion disk internal structure, with the changes in disk configuration at different annuli being interconnected. Therefore, the observed UV/optical fluxes should be expected to exhibit coherent stochastic changes.

The CHAR model has a broad scope for explaining quasar UV/optical variability and its connection to physical properties, which makes it a valuable tool for interpreting observed AGN variability. In particular, Sun et al. (2020a) explored the statistical properties of CHAR model-simulated light curves, including the effects of wavelength on variability, and investigated both short-term and long-term temperature fluctuations in AGN disks. In particular, Sun et al. (2020a) implemented a $1/f$ law for the PSD of $Q^+_{\rm mc}$, and determined the disk innermost temperature as 2.5 $logT^+_c$ and effective temperture as 2.5 $logT^+_{\rm eff}$, to find the statistical properties of light curves, as shown in Figure 4.1, T_c denotes the inner temperature of the accretion disk, while $T_{\rm eff}$ represents the effective temperature. The PSDs of the 3000 and 5100 Å light curves follow the shape of the $Q^+_{\rm mc}$ at low frequencies, however, get steeper than that of $Q^+_{\rm mc}$ at high frequency. Figure 4.2 presents the PSDs at 3000 and 5100 Å.

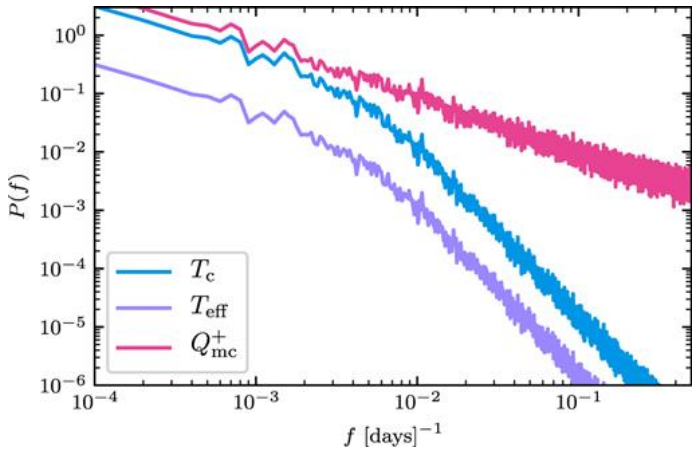

Figure 4.1: The Power Spectral Densities (PSDs) for 2.5 log $Q^+_{\rm mc}$, 2.5 log $T_{\rm c}$, and 2.5 log $T_{\rm eff}$ are presented. For enhanced visibility, they have elevated the PSD of 2.5 log $T_{\rm c}$ by a multiplicative factor of 10. Credits: Sun et al. (2020a).

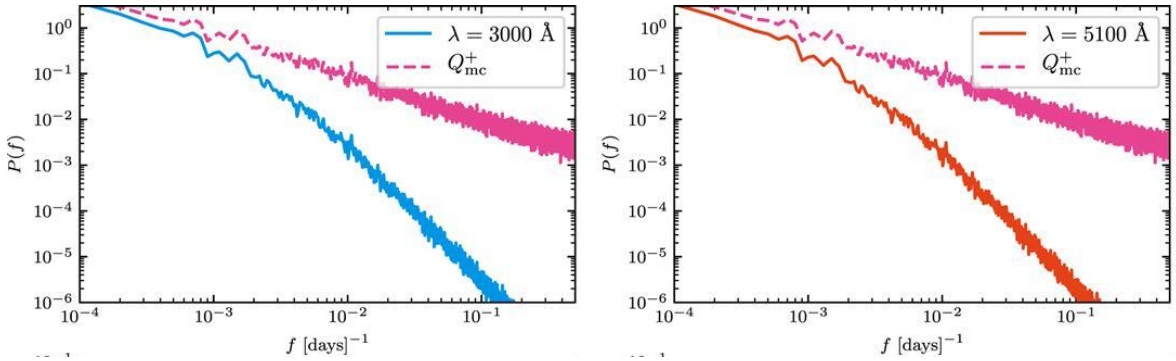

Figure 4.2: In the left section of the figure, the PSDs for the 3000 Å emission shown by the blue line, alongside 2.5 times the logarithm of Q^+_{mc}, depicted by the pink line. In the right section, a similar comparison is made for the 5100 Å emission, represented by the red line. Credits: Sun et al. (2020a).

One finding from this modelling is the wavelength dependency of the variability amplitude in the CHAR model-simulated light curves, which was inversely proportional to the wavelength (see Figure 4.3). Moreover, temperature fluctuations within the accretion disk intensify closer to its center and are more pronounced over shorter timescales (see Figure 4.4). These findings are crucial for comparison with our study presented in Chapter 3, where we analyzed the variance as a function of rest-frame wavelength using ZTF data. The CHAR model's predictions of wavelength-dependent variability as a function of accretion disk radius offer a compelling framework for interpreting our findings.

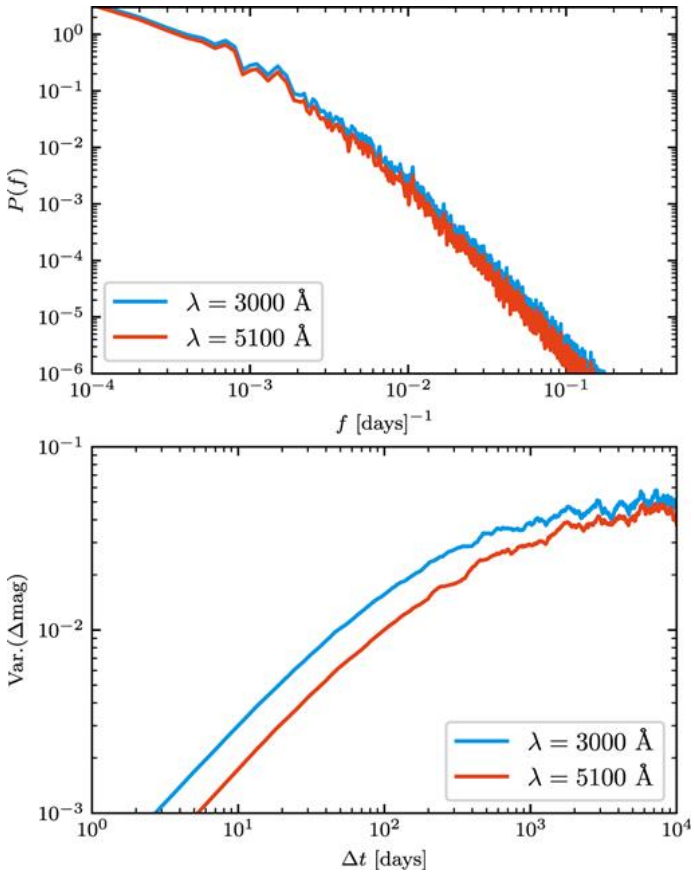

Figure 4.3: In the upper section of the diagram, the PSDs for emissions at 3000 Å and 5100 Å, illustrated with blue and red lines, respectively. The lower section showcases the Structure Functions (SFs) for the same emissions, again using blue for 3000 Å and red for 5100 Å. From this analysis, it is observed that the 3000 Å emission exhibits a higher level of variability, up to a factor of less than 2, compared to the 5100 Å emission. Credits: Sun et al. (2020a)

In this study, we analyzed the variance and variance ratio of light curves simulated by the CHAR model across various timescales, focusing on their dependency on the rest-frame wavelength, to compare them with observed findings. While previous studies have investigated variability in relation to λ_{RF}, direct comparisons with the models discussed in Chapter 1 have been notably absent. The chapter is structured as follows: Section 4.2 introduces the CHAR model framework and establishes the setup for modeling quasar variability. This section also outlines the methodology for simulating light curves using the CHAR model. Section 4.3 investigates the comparison between the CHAR model simulated light curves and ZTF observational data, evaluating how well the model predictions align with the observed

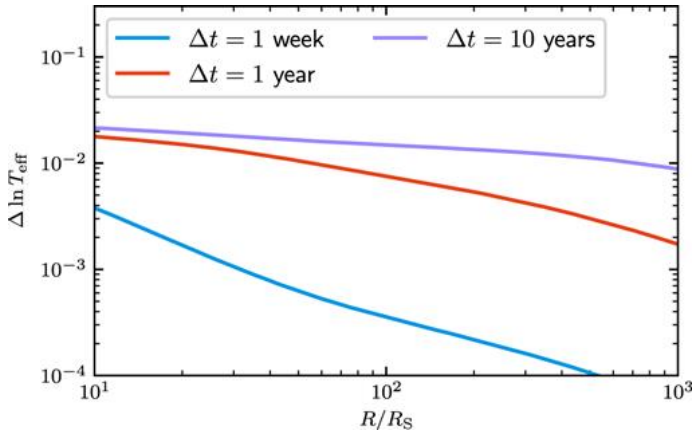

Figure 4.4: The variability amplitude ratio, $\Delta T_{\rm eff}/T_{\rm eff}$, varies with distance from the center. The plots in blue, red, and purple represent fluctuations over periods of one week, one year, and ten years, respectively. Credits: Sun et al. (2020a)

variability. Section 4.4 discusses the results of the CHAR model-data comparison, including the dependence of variability on model parameters, the power spectra of the simulated light curves, insights gained from the data-CHAR model comparison, and the limitations of the model with suggestions for future work. Section 4.5 summarizes the main findings and evaluates the performance of the CHAR model in predicting quasar variability, along with potential improvements for future work.

4.2 Modeling ZTF Quasar Variability

4.2.1 Establishing the CHAR Model Framework

To deepen insights into the interband correlations, time delays, and various observed phenomena of AGN UV/optical variability, the CHAR model proposes a significant link between the corona and the accretion disk, mediated by magnetic fields. The fluctuations in the magnetic field of the corona can cause corresponding fluctuations in the accretion disk. These fluctuations, which have a power distribution specified by the function Q^+_{mc}, can induce coherent magnetic turbulence in the disk. This means that the fluctuations at different distances from the center of the disk are correlated. The magnetic turbulence in the disk dissipates and leads to variable heating rates. It is the thermal timescale that determines how long it will take for the disk temperature to adapt to the varying disk heating rate. Thus, it follows that fluctuations in the coronal magnetic fields are likely to lead to consistent and stochastic variations in the observed UV/optical fluxes.

However, at the much longer viscous timescale, the variability of the accretion disk is likely influenced by both the magnetically coupled corona and the intrinsic disk dissipation of gravitational potential energy. Q^+_{vis} is the vertically integrated internal viscous heating rate, which changes simultaneously with Q^+_{mc} after a travel-time delay of the magnetic waves. The travel-time delay implies that $Q^+_{vis}(t) = Q^+_{mc}(t - R_X/c_{avf})/k$, where R_X and c_{avf} are the distance from the disk to the corona and Alfvén velocity respectively, and k is the average Q^+_{mc}/Q^+_{vis}, which is assumed to be a constant and independent of radius. The Alfvén velocity

in an intensely magnetized plasma could match the velocity of light. It is also assumed that an accretion disk possesses the capacity to adapt its vertical configuration and scale height in reaction to the changing parameters $Q^{+}_{mc}(t)$ and $Q^{+}_{vis}(t)$. This adaptability suggests a dynamic interaction between different parts of the accretion disk, where changes in the corona can lead to adjustments in the disk to maintain a certain equilibrium or stability in the accretion. The temperature fluctuations within the disk are addressed by solving vertically integrated thermal-energy conservation equations (see Kato et al. 2008), which essentially balance the rate of internal energy change of the disk and the work done by or on the disk (viscous and other mechanisms), and the cooling (radiation) processes.

4.2.2 Simulating light curves

In order to solve the disk thermal evolution it is necessary to first specify the variability power distribution of Q^{+}_{mc}. Previous works have shown that the PSD for the energy dissipation in the corona follows a $1/f$ relationship (Lyubarskii 1997; King et al. 2004; Arévalo et al. 2008; Lin et al. 2016). Noble & Krolik (2009) MHD simulations find similar results. Building on this finding, Sun et al. (2020a, 2020b) also adopted a $1/f$ model for the PSD of Q^{+}_{mc}. In this work alternative PSDs for Q^{+}_{mc} where explored, specifically $\propto 1/f^{\beta}$ where β ranges from 0.6 to 2, aiming to identify the best fit of the data. All light curve simulations were carried out by Professor M. Sun (see Figure 4.5).

The CHAR model also require a few key parameters: the dimensionless accretion rate ($\dot{m}$), a radiative efficiency of $\eta = 0.1$; the black hole mass (M_{BH}); the dimensionless viscosity parameter (α, defined as the ratio of the magnitude of the turbulent stress to the thermal pressure); and the fractional variability amplitude of the coronal magnetic fluctuations (δ_{mc}). Research over the years (e.g., Chokshi & Turner 1992; Small & Blandford 1992; Yu & Tremaine 2002; Marconi et al. 2004; Shankar et al. 2004; Cao & Li 2008; Cao 2010; Li et al. 2012; Ueda et al. 2014) has suggested η values ranging between 0.05 to 0.1.

To match our quasar sample $\dot{m} = 0.1$ and $M_{BH} = 10^{8} M_{\odot}$ were chosen. To determine the values of the remaining free parameters, α and δ_{mc}, we explored various combinations by incrementing α in eight steps from 0.1 to 0.8, while the magnetic fluctuation fractional variability (δ_{mc}) was tuned to fit the flux changes, which, while influencing the amplitude of variations, did not alter power spectra or wavelength dependence. In our analysis, k is set to 1/3. It is important to note that Sun et al.(2020a) found that the results remain unchanged considering different values of k.

Following Sun et al.(2020a) the boundaries of the accretion disk were established at 10 Schwarzschild Radii (R_s) for the inner limit and 1000 (R_s) for the outer limit. Although the inner boundary is set at 10 (R_s), actual extent of the disk can reach down to the innermost stable circular orbit. However, the regions within 10 R_s are expected to make minimal contributions to the optical emissions being analyzed. Indeed, adjusting the inner boundary to 3 R_s would not significantly alter our findings (Sun et al. 2020a). This assumption also allows the model to ignore the effects of general relativity and complex comptonization mechanisms.

After computing the effective temperature as a function of radius and time ($T_{\rm eff}(R, t)$)

Planck's law is used to determine the black-body spectral radiance as a function of R and t, which is then integrated over the area of an annulus of size ΔR to obtain $L_\lambda(R,t)$. The total luminosity $L_\lambda(t)$ at a given wavelength λ and time t is obtained by integrating the contributions from each annulus over the entire disk radius from $R_{\rm in}$ to $R_{\rm out}$, where $R_{\rm in} = 3{\cdot}R_s$ and $R_{\rm out} = 1000 \cdot R_s$. The observed flux $F_\lambda(t)$ in the rest-frame is derived directly from the total luminosity $L_\lambda(t)$ by rescaling to the observed magnitudes without changing the variability properties (Δmag or $\Delta F/F$).

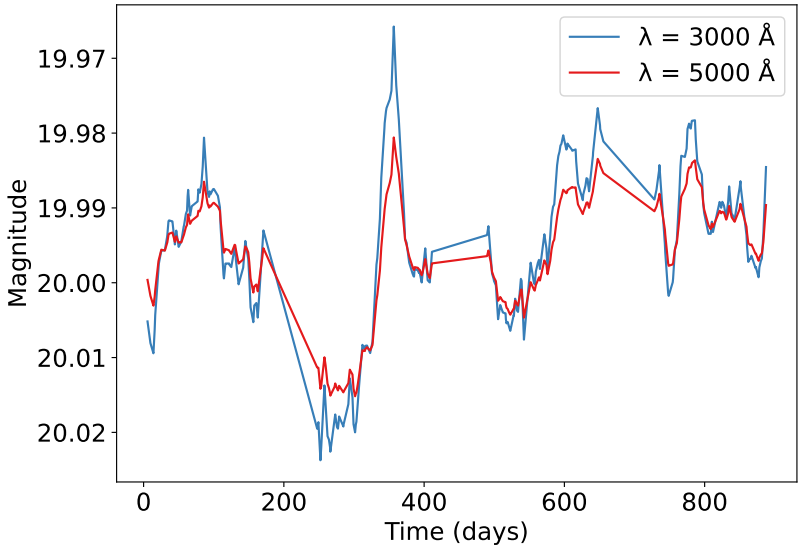

Figure 4.5: Mean simulated light curves for the 3000 Å (blue curve) and 5000 Å (red curve) emission lines derived from 128 simulations.

4.3 Data-CHAR Model Comparison

We analyze the variance-wavelength relationship for different power-laws describing the input variability of Q^+_{mc}, i.e., $\propto 1/f^\beta$, where β spans from 0.6 to 2 (see Figure 4.8). We also explore how the variance changes with wavelength under different values of the viscosity parameter, α, from 0.1 to 0.8 (see Figure 4.9). We generate 128 mock light curves in the rest-frame having the same sampling pattern as the observed light curves for wavelengths and covering the 1500 Å to 9000 Å and for different combinations of the α and β values. The CHAR model light curves extend up to 1000 days in the rest-frame, which corresponds to approximately 4 years in the observed frame for a quasar at $z = 0.5$. These light curves include seasonal gaps, with about 4 months missing each year in the observed frame. For each light curve, the magnitude values are normalized so that the mean is 20 mag. The sample size of 128 mock light curves ensures robust statistical validity while being computationally feasible. Figure 4.5 presents the light curves for 3000 Å and 5000 Å to illustrate the obtained magnitude variations over time.

To compare the simulated data with the ZTF results already presented, the variance was determined for the four timescales already used in our analysis (300, 150, 75, and 30 days).

Again the Mexican Hat methodology was implemented for variance determinations. The mean was then obtained for each wavelength value from the 128 variance determinations. Error bars were computed as the standard error of the mean.

The analysis reveals that higher α values correspond to increased variance and flatter slopes, with a trend of saturation to a maximum variance for even larger α values. This is indicative of the improved capability of accretion disk to adjust to fluctuations originating from the corona as α increases, thereby amplifying the observable variability over a broader range of wavelengths. On the other hand, the β parameter induces a more complex behaviour for the variance, first increasing sharply as β grows from 0.6 to 1.0, reaching a maximum value for $\beta \sim 1.0 - 1.3$, and then decreasing for even larger values. The slopes of the variance-wavelength spectra remain rather constant, except for the highest β values, where it flattens.

Comparison with the data revealed the optimal value of $\alpha = 0.5$. This specific choice of α, combined with a δ_{mc} value of 1.32, which indicates that the structure function of the natural logarithmic heating rate fluctuation over a 100-day period is 1.32, most accurately reflected the normalization observed in the data. The biggest disagreements appear at 150 days, where the normalization of the CHAR model appear too large, and at 30 days, where the slope of the model it too flat.

The analysis also reveals that a power spectral density (PSD) proportional to $1/f^{0.6}$ aligns closely with our observational data, diverging from the $1/f$ approach taken by Sun et al. (2020a, 2020b). This modification to the PSD, favoring a β value of 0.6, corresponds to a shallower power decrease with frequency, hence emphasizing the impact of shorter-term (high frequency) fluctuations.

Figures 4.6 and 4.7 present the dependence of variance and variance ratios with rest-frame wavelength (λ_{RF}) for both data and the CHAR model, for $\alpha = 0.5$ and $\delta_{mc} = 1.32$. Table 4.1 presents the linear regression results, detailing the intercept (a) and slope (b) for both the observed data (corrected and uncorrected) and the CHAR model. Our analysis suggests a considerable degree of alignment in variance for most of the timescales we studied, with the slope values aligning closely within one standard deviation for the 300, 150, and 75-day periods. However, the slopes exhibit a 3σ deviation between the observed and CHAR model values for the 30 day timescale, with the observed slope being steeper than that of the model. The intercepts were within 1σ of each other for all the timescales studied.

The timescales we have examined exceed the reprocessing timescales for a quasar harboring a black hole mass of 10^8 solar masses and an Eddington ratio of 0.1. Kammoun et al. (2021) investigate in detail the accretion disk response to fluctuating irradiation (likely from the X-ray corona) highlighting the process of disk thermal reverberation. Their findings confirm many previous works where the delay between X-ray and UV/optical emissions increases with wavelength, but generally staying below 10 days for wavelengths as long as 10,000 Å. This suggests that at the timescales we study (30–300 days), variations in the primary X-ray signal would be reprocessed and reemited without significant variance damping due to the different paths the light will follow before reaching the observer. In other words, the influence

Table 4.1: Results from linear regressions showing the best-fit slope (a) and intercept (b) using λ_{RF} as the independent variable. The table is divided into three sections: 'Original Data' (linear regressions for the initial variance and variance ratio), 'Corrected Data' (linear fits to the revised variance and variance ratio accounting for variance suppression effects), and 'CHAR Model' (regressions for variance and variance ratio based on the CHAR model predictions).

	Original Data		Corrected Data		CHAR Model	
timescale	a	b	a	b	a	b
variance(300 days)	-1.22 ± 0.18	1.47 ± 0.63	-1.28 ± 0.15	1.70 ± 0.54	-1.122 ± 0.011	1.147 ± 0.041
variance(150 days)	-1.37 ± 0.16	1.89 ± 0.58	-1.38 ± 0.14	1.95 ± 0.49	-1.378 ± 0.005	1.993 ± 0.018
variance(75 days)	-1.61 ± 0.13	2.61 ± 0.45	-1.64 ± 0.10	2.72 ± 0.36	-1.728 ± 0.002	3.039 ± 0.008
variance(30 days)	-2.58 ± 0.13	5.73 ± 0.45	-2.58 ± 0.15	5.80 ± 0.52	-2.184 ± 0.003	4.309 ± 0.010
variance ratio(300/150)	-0.04 ± 0.16	0.25 ± 0.56	-0.05 ± 0.17	0.32 ± 0.60	0.321 ± 0.003	-1.031 ± 0.012
variance ratio(150/75)	0.40 ± 0.07	-1.25 ± 0.26	0.42 ± 0.07	-1.33 ± 0.26	0.336 ± 0.006	-0.990 ± 0.023
variance ratio(75/30)	0.83 ± 0.20	-2.69 ± 0.70	1.29 ± 0.20	-4.24 ± 0.72	0.448 ± 0.001	-1.232 ± 0.004

Note: Observed data are reported to two decimal places, reflecting measurement precision. Model data, due to computational accuracy, are to three.

of light travel time effects due to the size of the disk emitting regions (which are larger at longer wavelengths because of the disk temperature profile) should be negligible.

If any potential dampening is indeed present, it should be observable at the shorter 30-day timescale and would be expected to have a more pronounced dampening effect at longer wavelengths. This should lead to a steeper correlation than predicted if reprocessing is accounted for. As the CHAR model does not take into account X-ray irradiation and the reprocessing of this incoming variable source, it is possible that the model disk response at the shortest timescales is too high at the longest wavelengths. This is in qualitative agreement with the results shown. X-ray heating has not been implemented in the CHAR model and a prescription needs to be determined to characterize the level of correlation between the X-ray energy power and Q^{+}_{mc}.

Our analysis identified a consistent positive correlation between the 150/75 and 75/30 variance ratios and the rest-frame wavelength, evident in both the simulated CHAR model light curves and the observational data. However, the correlation for the 300/150 ratio was steeper in the CHAR model and flatter in the observed data. Through linear regression, we found that the CHAR model variance ratios for the 300/150 and 150/75 ratios are consistent with those observed. The slope differences fall within 3σ and 2σ, respectively, and the intercept differences fall within 1σ. Discrepancies were notable in all variance ratios involving the 30-day timescale, as expected.

4.4 Discussion

4.4.1 Power spectra of CHAR model light curves

The power spectra for the 3000 Å and 5000 Å wavelenghts, as illustrated in Figure 4.10, reveal that the emission at 3000 Å exhibits greater variability than that of the emission at 5000 Å, as also observed in the ZTF data. Through the use of the thermal-energy conservation law and the α-viscosity prescription (as proposed by Shakura and Sunyaev in 1973), it can be demonstrated that the thermal timescale (t_{th}) has the following form:

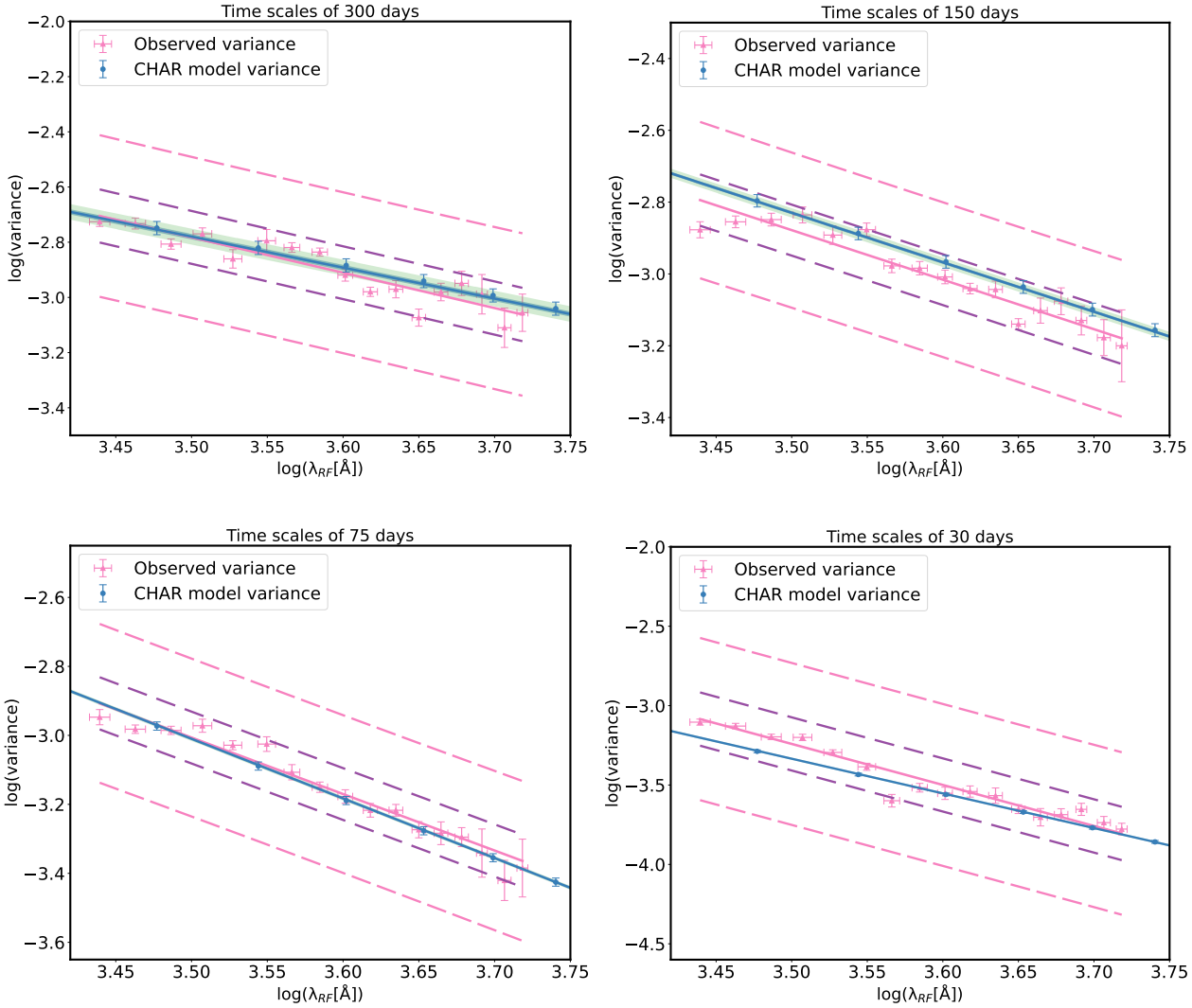

Figure 4.6: Comparison of ZTF data with the CHAR model for variance versus rest-frame wavelength plots across four different timescales. The observed median variance is indicated by pink triangles, with error bars showing the root-mean-squared scatter. The solid pink line represents the linear fit to the observed median variances, while the purple and pink dashed lines illustrate 1σ and 3σ uncertainties, respectively. Blue circles denote the mean model variance estimated for the corresponding 128 simulated rest-frame wavelength light curves, with error bars reflecting the Standard Error of the Mean. The solid blue line represents the linear fit to the mean model variances. The shaded blue and green areas indicate the 1σ and 3σ uncertainties, respectively. The fits to the observed variance and the CHAR model variance show good agreement, except for the shortest timescale of 30 days.

$$\tau_{\rm TH} \sim \frac{1}{\alpha\Omega_k} \propto \alpha^{-1}\lambda^2[(k+1)\dot{M}]^{0.5} \propto \alpha^{-1}\lambda^2 L_{\rm bol}^{0.5} \tag{4.1}$$

With α, λ, and L_{bol} the dimensionless viscous parameter, wavelength, and bolometric luminosity, respectively. The bolometric luminosity (L_{bol}) is obtained by integrating the summation of Q^+_{vis} and Q^+_{mc}.

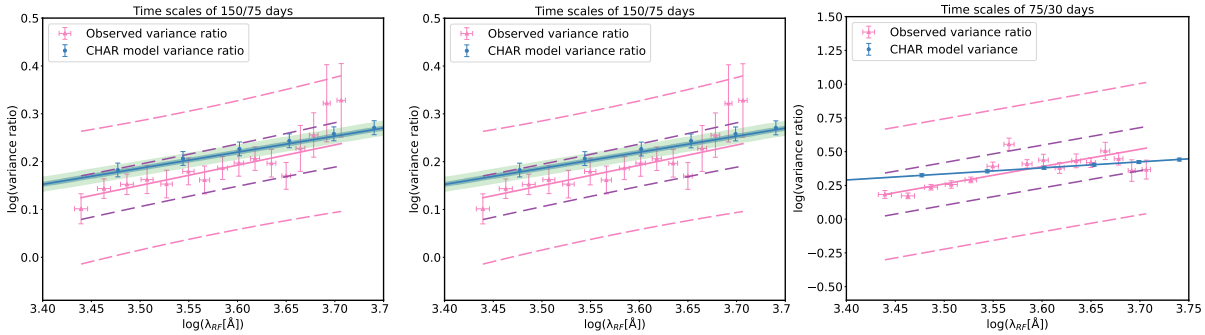

Figure 4.7: Comparison of ZTF Data and the CHAR Model: This figure illustrates the comparison between ZTF data and the CHAR model for the variance ratio versus rest-frame wavelength. The pink triangles represent the observed median variance ratios, with the solid pink line showing the linear regression fit, and the purple and pink dashed lines denote 1σ and 3σ uncertainties. The blue circles indicate the mean model variance ratios, with error bars representing the Standard Error of the Mean, and the solid blue line depicts the linear fit to these model variance ratios. The shaded blue and green regions show the 1σ and 3σ uncertainties. The CHAR model variance ratios are consistent with the observed data for the 300/150 and 150/75 timescales, but the model fails to match the variance ratio slope for the 75/30 timescale.

The thermal timescale essentially measures how quickly a particular region of the accretion disk can respond to changes, adjusting its temperature back to a state of equilibrium. Equation 4.1 highlights that the region responsible for the shorter wavelength emission operates on a shorter thermal timescale compared to the region emitting at longer wavelength. This implies that the inner, hotter parts of the disk, which emit at shorter wavelengths like 3000 Å, can adapt more rapidly to disturbances than the cooler, outer regions emitting at longer wavelengths like 5100 Å. Therefore, these inner hot regions can show more power for any given frequency.

The top panel of Figure 4.12 displays our chosen CHAR model power spectra at 3000 Å alongside the best-fit bending power law and residuals, which highlight the presence of some oscillations in the CHAR PSD. The best-fit parameters are: $A = 0.0054$, $\alpha_{\rm L} = -0.843$, $\alpha_{\rm H} = -2.238$, and $f_{\rm b} = 0.01 {\rm d}ays^{-1}$. These parameters define the amplitude, the low- and high-frequency slopes, and the frequency at which the power law bends, respectively. In contrast, the DRW fit shown in Figure 4.11 demonstrates that the DRW model is a poorer description. This is evident from the comparison where the DRW model significantly deviates from the CHAR model power spectra at short timescales.

The best fit values for $\alpha_{\rm L}$ and $\alpha_{\rm H}$ must be compared to those found by Arévalo et al. (2024). As already mentioned, that work found that a high-frequency and low-frequency PSD slopes of α_H = -3 and α_L = -1, as well as α_H = -2.5 and α_L = -0.5, provide a good fit for quasars with $7.5 < \log(M_{BH}/M_{\odot}) < 9.5$ and $-2 < R_{\rm Edd} < 0$, at a fixed rest-frame wavelength of approximately 2900 Å. The CHAR model best fit slopes show good agreement with the α_L prescription of -1, predicting a slightly flatter α_L. But it predicts a significantly flatter α_H (although not as flat as the DRW prescription). This again points at further corrections needed at the highest frequencies. A steeper slope implies more dampening of the variance

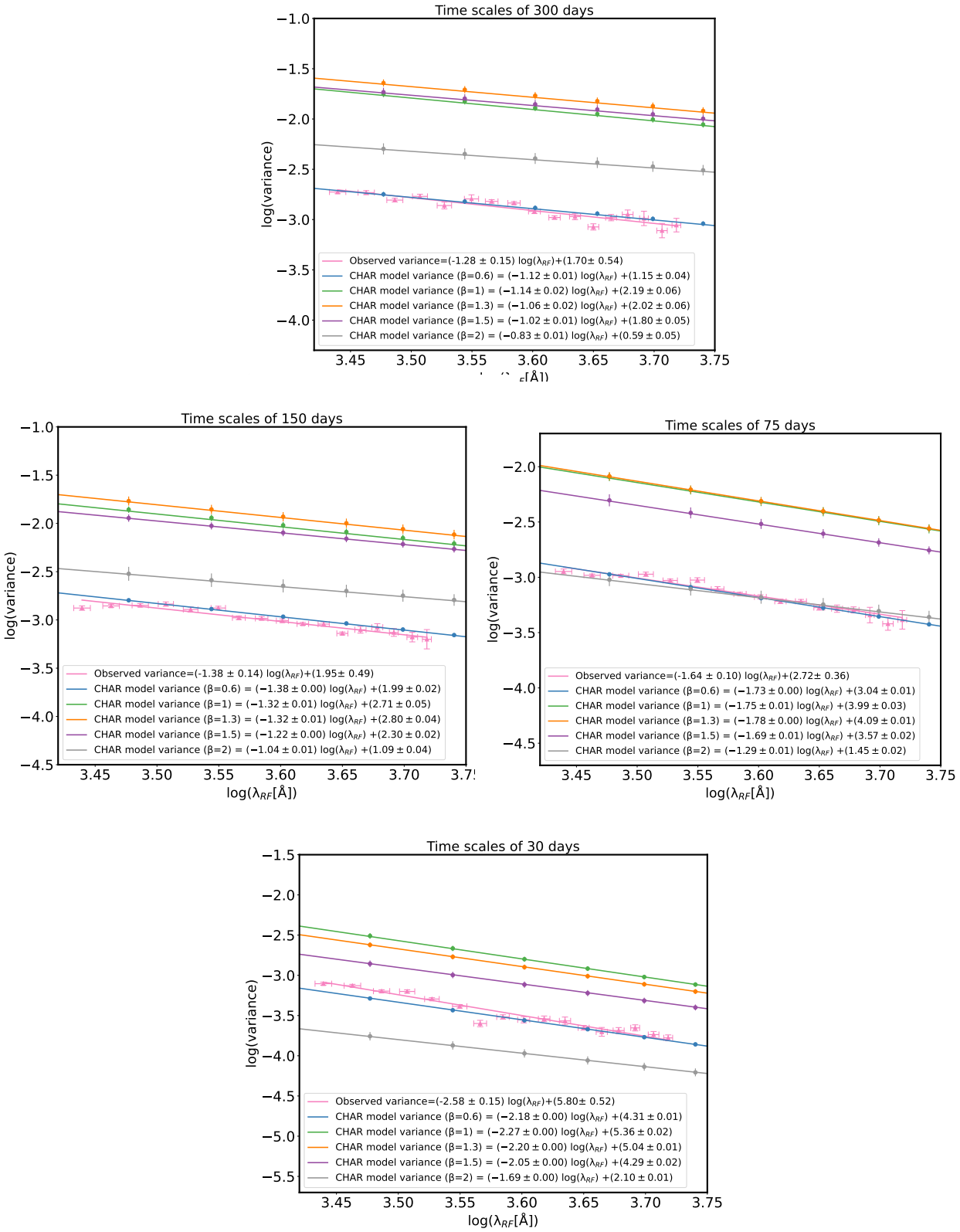

Figure 4.8: CHAR Model Variance and Wavelength Analysis Across Four Timescales: The figure depicts the variance versus rest-frame wavelength for the CHAR model over four timescales, exploring PSD values with β ranging from 0.6 to 2. Multiple linear regression fits are shown in the plots, as noted in the legends, to reveal how different PSD values affect behavior of the model. pink triangles represent observed median ZTF variances with error bars for root-mean-squared scatter, and a solid pink line provides the linear fit to the observed variance data.

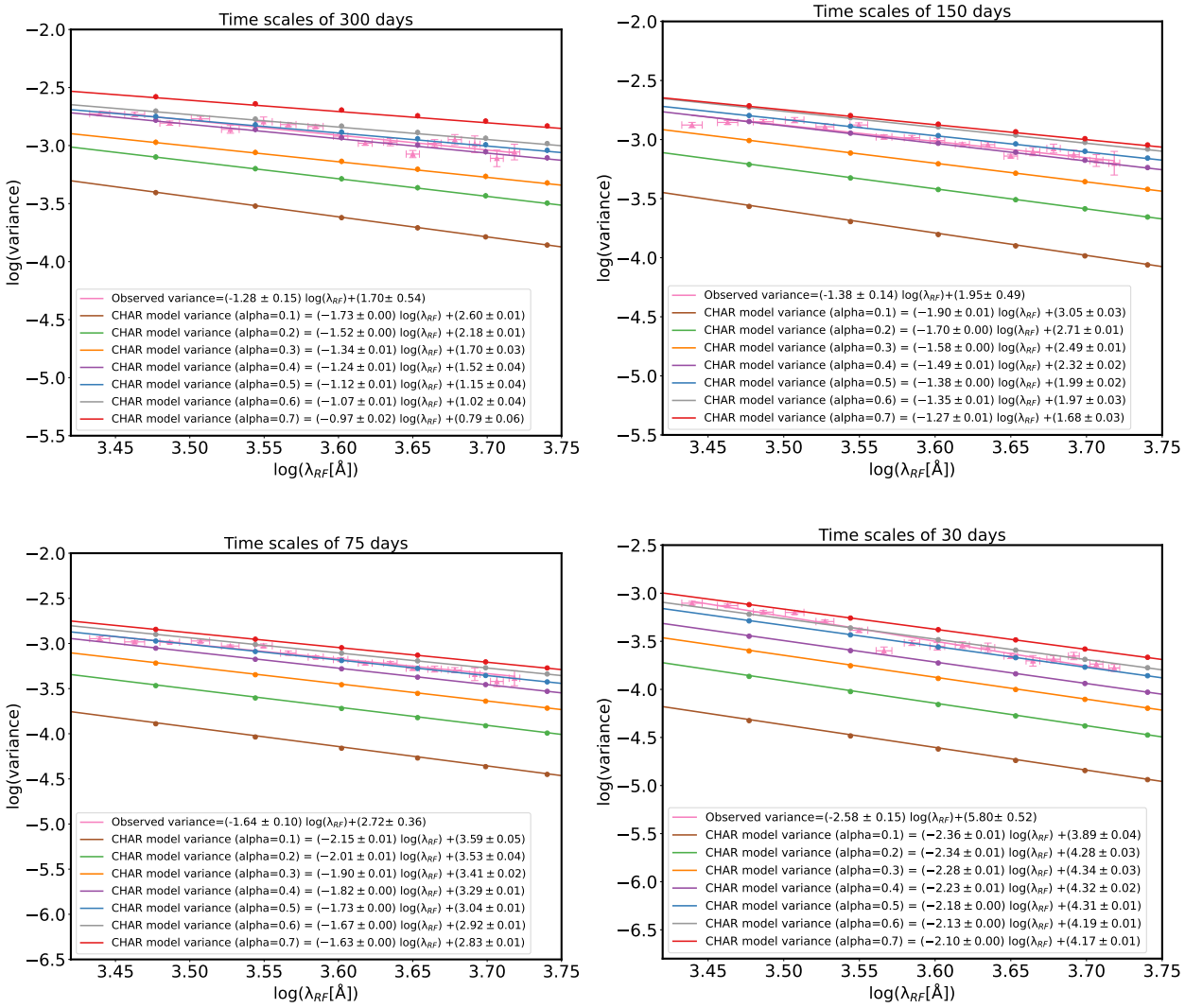

Figure 4.9: CHAR Model Variance-Wavelength Analysis with Varying α Values: The figure shows the relationship between variance and rest-frame wavelength in the CHAR model for different α values ranging from 0.1 to 0.8. Multiple linear regression models are displayed, as indicated in the legend, demonstrating the effects of changing α on behavior of the model. Observed ZTF median variances are represented by pink triangles with error bars for root-mean-squared scatter, and the solid pink line illustrates the linear regression fit to the observed data.

at the fastest timescales. In the future it can be explored whether reprocessing could provide sufficient smoothing of the variability to account for this disparity.

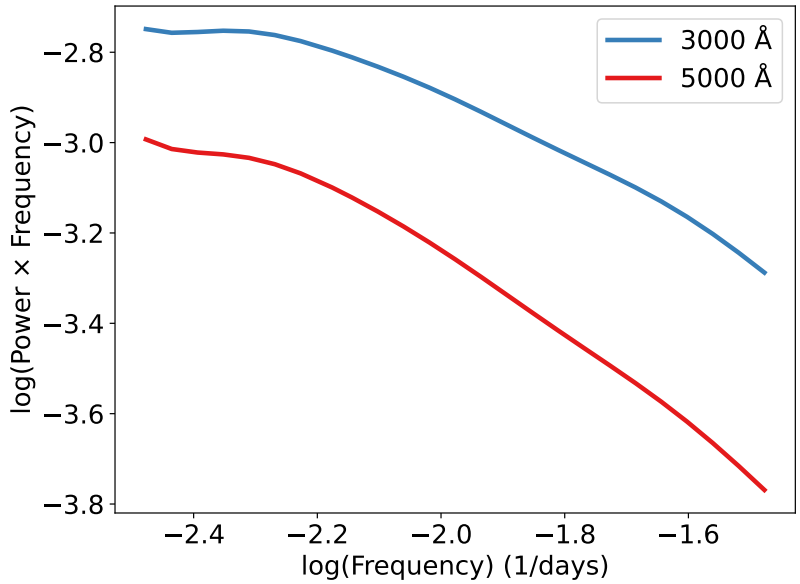

Figure 4.10: The plot shows the power spectra of the 3000 Å (blue curve) and 5000 Å (red curve) emissions.

4.4.2 Insights from CHAR Model-Data Comparison

In our study, we bridge the gap between the observed quasar variability across different rest-frame wavelengths (λ_{RF}) and theoretical models, specifically focusing on the CHAR model discussed in the introduction. Our comparison in Section 4.3 highlights how well the CHAR model, with a viscosity parameter (α) set at 0.5, reproduces the observed trends: an inverse relationship between variance and wavelength, with a steepening of the correlation towards shorter timescales, and more quantitavely, the correct variance normalizations and slopes for the four timescales discussed here.

The concept of viscosity in standard accretion disk theory is critical, as it defines the thermal timescale ($\tau_{\rm TH} = \tau_{\rm DYN}/\alpha$). This timescale is essential for understanding how different parts of the disk respond to changes. A region in thermal equilibrium reacts as a unified whole, with its response timescale and intensity inversely proportional and proportional to its size, respectively. Conversely, areas not in equilibrium act as a sum of smaller, incoherent parts, leading to rapid but smaller fluctuations. Hence, the sum of incoherent fluctuations will supresses vatiations faster than $\tau_{\rm TH}$, and this effect becomes more severe at shorter timescales. This explains why the 300-day variance spectrum has the largest variance, followed by the 150-day variance spectrum and so on (for all wavelengths). As longer wavelengths are emmited primarely at larger radii, the suppression of variability will be more severe for longer wavelengths, where the total variance needs to be summed over a larger area, explaining the observed negative slopes of variance as a function of wavelength

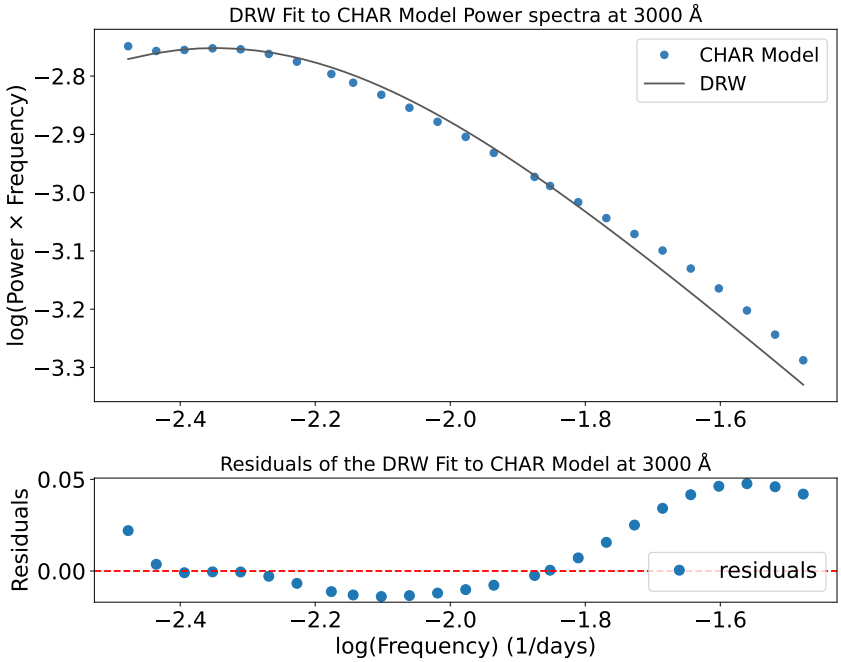

Figure 4.11: The top panel of the figure displays the CHAR model power spectra at 3000 Å (blue dots) alongside the best-fit DRW model (solid gray line). The bottom panel presents the residuals of the fit (blue dots), with a horizontal red dashed line at zero to indicate perfect agreement between the data and the model. The residuals are plotted against the logarithm of the frequency, with the y-axis showing the logarithmic difference between the observed data and the fitted model.

(for all timescales). Finally, the dependence of $\tau_{\rm TH}$ with radius implies that regions emitting primarely at longer wavelengths have characteristicly larger $\tau_{\rm TH}$ values. Hence, the loss of fast variation is more pronounced as wavelengths get longer, explaining the different slopes observed in the variance spectra as a funtion of timescale.

In principle, the loss of high-frequency power in the observed PSDs should not occur at sufficiently small frequencies, where the input Q^{+}_{mc} distribution should be recovered. Interestingly, adopting a Q^{+}_{mc} power distribution $\sim 1/f^{\beta}$ with $\beta = 0.6$ returns $\alpha_{\rm L} \sim -1$, an excellent match for the PSD low-frequency slope determined Arévalo et al. (2024). Whether a flatter slope is found at even smaller frequencies can only be tested with much longer monitoring, something only available for a handful of objects at the moment.

4.4.3 Limitations of the CHAR model and Future Work

The CHAR Model has potential for further refinement. Disk winds have the potential to exert significant power and alter the composition of the accretion disk, as observed by Sun et al. 2019. Additionally, the emission from the disk may deviate from a perfect black-body, as noted by Hall et al. (2018). The UV/optical variability caused by X-ray reprocessing of a static SSD or the emission from the BLR clouds is not taken into account in the model. This has been discussed in previous studies by Cackett et al. (2018) and Sun et al. (2018a). Besides, the CHAR model requires to include not only the reprocessing signal but also the

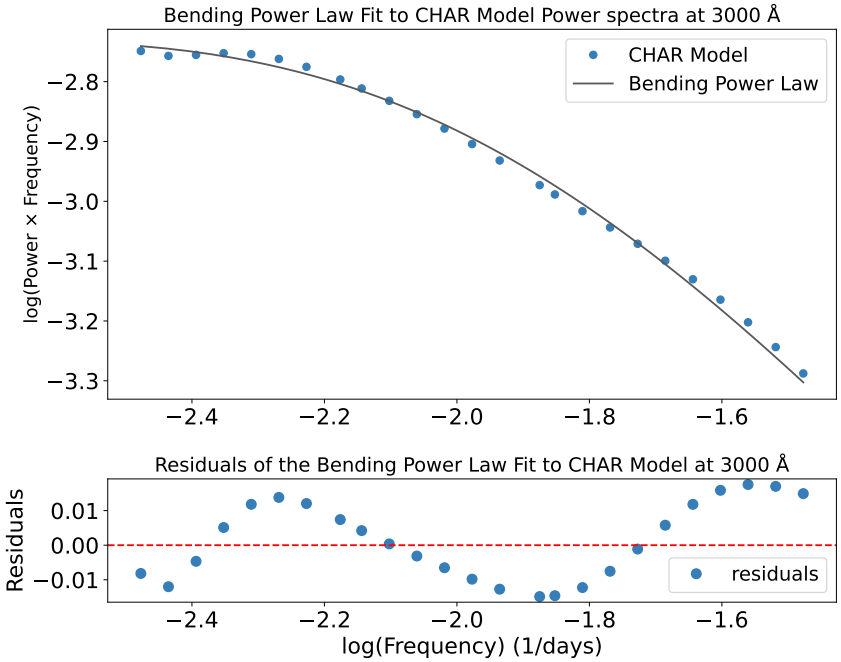

Figure 4.12: The top panel of the figure illustrates the CHAR model power spectra at 3000 Å (blue dots) along with the best-fit bending power law model (solid gray line). The bottom panel shows the residuals of the fit (blue dots) with a horizontal red dashed line at zero to indicate perfect agreement between the data and the model. The residuals are plotted against the logarithm of the frequency, with the y-axis representing the logarithmic difference between the observed data and the fitted model.

accretion rate fluctuation inherent to the accretion disk.

In terms of the analysis of quasar ZTF light curves, it would be important to independently determine the dependency of the PSD bending frequency with wavelength, as previous works used a DRW modeling for these determinations. Also, the large number of quasars with light curves available in both the g and r-bands could be used to determine the characteristic time lags between two rest-frame wavelengths as given by their redshifts. Binning in black hole mass and Eddington ratio it might be possible to determine population-wide prescriptions for the disks geometry and responsivity.

With the upcoming LSST survey, we expect to obtain extensive AGN variability data that will significantly extend the duration of the light curves in six different filters, thus allowing for more thorough characterization of the quasar PSD. Besides, the depth of LSST data will allow to extend variability studies to much higher redshifts and test whether accretion theory can be assumed to behave in the same way locally and in the early Universe.

4.5 Conclusion

This thesis chapter analyzed quasar variability using the CHAR model, focusing on its relationship with rest-frame wavelength (λ_{RF} for black hole masses of $10^8 M_\odot$ and Eddington

ratios of 10^{-1}. Our study examined various observational timescales (30, 75, 150, and 300 days) and wavelengths ($\sim$ 2700 - 5200 Å).

In our analysis comparing observed variability with the CHAR model, as presented in Sun et al. (2020a), we found that adopting parameters $\alpha = 0.5$ and $\delta_{mc} = 1.32$, closely aligns with the observed data for all timescales, both in slope and intercept. However, at the 30-day timescale, we observed a notable deviation in the slope between the CHAR model and the observed data. It is suggested that including the reprocessing scenario in the model might alleviate this discrepancy.

Chapter 5

Conclusions

Here I present an investigation into quasar variability, using a method that separates variability on different timescales and examines its dependence on rest-frame wavelength. Furthermore, we assess the applicability of CHAR models by comparing them with ZTF data.

Chapter 2 presented essential analytical tools and methodologies for AGN variability studies, addressing challenges such as irregular sampling, noise, and stochastic variations in the ZTF optical light curves of AGN. The chapter covered the following key areas:

- Extracting Information from AGN Time Series: Methods for analyzing AGN time series were explored, focusing on extracting meaningful information about variability and underlying physical processes.
- Mexican Hat Filter: The Mexican Hat filter was employed for variance estimation in light curves. For a light curve with no gaps, a Mexican Hat filter is applied to isolate variations at specific time scales. This technique involves convolving the original light curve with two Gaussian filters of similar widths, calculating the difference between these convolved light curves, and then determining the variance of the resulting filtered light curve. This method effectively manages data gaps that often occur in optical light curves due to seasonal observability. The chapter provided detailed information on the implementation and application of the Mexican Hat code.
- Simulating Light Curves: This section describes methods for generating artificial light curves with known statistical and variability properties to understand sampling irregularities and refine variability models. It includes two primary approaches:
  - **Bending Power Law Model:** This method generates light curves in the frequency domain following a power spectrum characterized by a low and a high-frequency power law and a bending frequency determining the transition point. The power law is then transformed to the time domain to produce simulated AGN light curves. This approach effectively simulates realistic light curves that reflect both the statistical properties of AGN variability and the stochastic nature of the data.
  - **CHAR Model (Found in Chapter 4):** The CHAR model simulates quasar

UV/optical variability by modeling interactions between the magnetic corona and the accretion disk. It generates synthetic light curves by introducing a $(1/f)^{\beta}$ prescription for the magnetic fluctuations that propagate and heat the accretion disk. Light curves are determined by solving the vertical thermal structure of the accretion disk as a function of time and wavelength. This simulations were performed by Dr. Mouyuan Sun.

By presenting these tools and methodologies, Chapter 2 laid the groundwork for the detailed analyses conducted in subsequent chapters. The discussed techniques ensure robust and reliable interpretation of AGN variability data and their comparison with models.

In Chapter 3, our investigation focused on the relationship between quasar variability and rest-frame wavelength, using light curves from the ZTF Data Release 15. Our methodology was designed to isolate the effects of wavelength on quasar variability while controlling for other factors such as black hole mass and accretion rate. In more detail, we corrected the observed quasar variance to a common black hole mass of $10^8 M_{\odot}$ and an Eddington ratio of 10^{-1}, and analyzed variability across four distinct timescales (30, 75, 150, and 300 days) across wavelengths ($\sim 2700 - 5200$ Å). The detailed approach and the resulting conclusions are outlined below.

- Our analysis revealed several important insights into quasar variability. We confirmed a significant inverse correlation between quasar variance and rest-frame wavelength, consistent with previous studies and supporting the notion that variability decreases with increasing wavelength. We also determined linear relations that describe how variance changes with wavelength over four different timescales (30, 75, 150, and 300 days). The observed relationships demonstrate that variance decreases more noticeably with λ_{RF} at shorter timescales.

- We identified an important interplay between variance and spectral components such as the Balmer emission lines and the Balmer and Fe II pseudo-continua, by modeling their influence on the observed variability spectrum. This aspect highlights the importance of accounting for these spectral features to accurately interpret quasar variability.

- Additionally, as a probe of PSD slope, we determined the correlation between variance ratio and rest-frame wavelength. All ratios showed a positive dependency, except for the 300/150-day timescale which exhibited a flat dependency. Our study also demonstrated that a wavelength-dependent break frequency alone cannot fully explain the changes in the power spectrum slope across different timescales. Our study suggests along with wavelength-dependent break frequency, the power spectrum steepness becomes more pronounced at longer wavelengths.

In Chapter 4, we explored the wavelength dependency of variability amplitude in simulated AGN light curves using the CHAR model. We also conducted a detailed comparison between the CHAR model predictions and ZTF quasar variability as a function of λ_{RF}, across different timescales (30, 75, 150, and 300 days). The main results derived from this study are:

- We demonstrated that the CHAR model predicts a wavelength-dependent variability

amplitude where the variability is inversely proportional to wavelength, as observed.

- Through detailed analysis, we determined that model parameters ($\alpha = 0.5$ and $\delta_{mc} = 1.32$) best fit the observed ZTF variance across different timescales and wavelengths.
- The slope and intercept of CHAR model variance vs. λ_{RF} closely agree with the observed trends in ZTF observed variance, particularly for longer timescales (up to 75 days). These results suggests that the CHAR model, despite its simplicity, correctly describes the radial dependency of variability and offers a prescription for further analysis of the mechanisms driving variability.
- The comparison of CHAR power spectra at high frequencies, which represent short-term variability, differs from the observed properties, with the CHAR model predicting a less steep decline in power compared to the observations. X-ray reprocessing, which is not considered in the CHAR model might aleviate this issue.

Chapter 4 established a strong framework for understanding AGN variability through the CHAR model, setting a foundation for future studies and advancements in modeling AGN light curves.

Finally, in this thesis, we analyzed ZTF DR15 light curves with a four-day cadence over up to 4.7 years, which effectively limited our ability to study variability on timescales shorter than 30 days or longer than 300 days. Future work using multi-wavelength data of LSST (Ivezić et al. 2019) will offer opportunities for more detailed studies of AGN variability and accretion disk mechanisms.

Bibliography

Andrae, R., Kim, D. W., & Bailer-Jones, C. A. L. 2013, A&A, 554, A137

Angione, R. J., & Smith, H. J. 1972, in External Galaxies and Quasi-Stellar Objects, ed. D. S. Evans, D. Wills, & B. J. Wills, Vol. 44, 171

Antonucci, R. 1993, ARA&A, 31, 473

Arévalo, P., Churazov, E., Lira, P., et al. 2024, A&A, 684, A133

Arévalo, P., Churazov, E., Zhuravleva, I., Hernández-Monteagudo, C., & Revnivtsev, M. 2012, MNRAS, 426, 1793

Arévalo, P., Lira, P., Sánchez-Sáez, P., et al. 2023, MNRAS, 526, 6078

Arévalo, P., & Uttley, P. 2006, MNRAS, 367, 801

Arévalo, P., Uttley, P., Kaspi, S., et al. 2008, MNRAS, 389, 1479

Arévalo, P., Uttley, P., Lira, P., et al. 2009, MNRAS, 397, 2004

Behar, E., Kaspi, S., Paubert, G., et al. 2020, MNRAS, 491, 3523

Bellm, E. C., Kulkarni, S. R., Graham, M. J., et al. 2019, PASP, 131, 018002

Breedt, E., Arévalo, P., McHardy, I. M., et al. 2009, MNRAS, 394, 427

Breedt, E., McHardy, I. M., Arévalo, P., et al. 2010, MNRAS, 403, 605

Burke, C. J., Shen, Y., Blaes, O., et al. 2021, Science, 373, 789

Butler, N. R., & Bloom, J. S. 2011, AJ, 141, 93

Cackett, E. M., Chiang, C.-Y., McHardy, I., et al. 2018, ApJ, 857, 53

Cameron, D. T., McHardy, I., Dwelly, T., et al. 2012, MNRAS, 422, 902

Cao, X. 2010, ApJ, 725, 388

Cao, X., & Li, F. 2008, MNRAS, 390, 561

Caplar, N., Lilly, S. J., & Trakhtenbrot, B. 2017, ApJ, 834, 111

Cappellari, M. 2016, MNRAS, 466, 798. https://doi.org/10.1093/mnras/stw3020

Cappellari, M., & Emsellem, E. 2004, PASP, 116, 138

Chakrabarti, S., & Titarchuk, L. G. 1995, ApJ, 455, 623

Chen, J., Sun, M., & Zhang, Z.-X. 2024, ApJ, 962, 134

Chokshi, A., & Turner, E. L. 1992, MNRAS, 259, 421

Clavel, J., Nandra, K., Makino, F., et al. 1992, ApJ, 393, 113

Collier, S., & Peterson, B. M. 2001, ApJ, 555, 775

Collier, S. J., Horne, K., Kaspi, S., et al. 1998, ApJ, 500, 162

Cristiani, S., Trentini, S., La Franca, F., & Andreani, P. 1997, A&A, 321, 123

Cutri, R. M., Wisniewski, W. Z., Rieke, G. H., & Lebofsky, M. J. 1985, ApJ, 296, 423

de Vries, W. H., Becker, R. H., & White, R. L. 2003, AJ, 126, 1217

Dexter, J., Xin, S., Shen, Y., et al. 2019, ApJ, 885, 44

Di Matteo, T. 1998, MNRAS, 299, L15

Edelson, R., & Nandra, K. 1999, ApJ, 514, 682

Edelson, R., Gelbord, J. M., Horne, K., et al. 2015, ApJ, 806, 129

Edelson, R., Gelbord, J., Cackett, E., et al. 2019, ApJ, 870, 123

Emmanoulopoulos, D., McHardy, I. M., & Uttley, P. 2010, MNRAS, 404, 931

Ezoe, Y.-I., Iyomoto, N., & Makishima, K. 2001, PASJ, 53, 69

Fausnaugh, M. M., Starkey, D. A., Horne, K., et al. 2018, ApJ, 854, 107

Gallo, L. C., Blue, D. M., Grupe, D., Komossa, S., & Wilkins, D. R. 2018, MNRAS, 478, 2557

Gaskell, C. M. 2007, in Astronomical Society of the Pacific Conference Series, Vol. 373, The Central Engine of Active Galactic Nuclei, ed. L. C. Ho & J. W. Wang, 596

Giveon, U., Maoz, D., Kaspi, S., Netzer, H., & Smith, P. S. 1999, MNRAS, 306, 637

Gliozzi, M., Papadakis, I. E., Grupe, D., Brinkmann, W. P., & Räth, C. 2013, MNRAS, 433, 1709

—. 2017, MNRAS, 464, 3955

Goad, M. R., Koratkar, A. P., Axon, D. J., Korista, K. T., & O'Brien, P. T. 1999, The Astrophysical Journal, 512, L95. https://dx.doi.org/10.1086/311884

Goad, M. R., Korista, K. T., & Ruff, A. J. 2012, MNRAS, 426, 3086

Goad, M. R., O'Brien, P. T., & Gondhalekar, P. M. 1993, MNRAS, 263, 149

Haardt, F., & Maraschi, L. 1991, ApJL, 380, L51

Hagen, S., & Done, C. 2022, arXiv e-prints, arXiv:2210.04924

Harrison, C. 2014, PhD thesis, Durham University, UK

Hawkins, M. R. S. 2003, MNRAS, 344, 492

Hernández Santisteban, J. V., Edelson, R., Horne, K., et al. 2020, MNRAS, 498, 5399

Hook, I. M., McMahon, R. G., Boyle, B. J., & Irwin, M. J. 1994, MNRAS, 268, 305

Hughes, P. A., Aller, H. D., & Aller, M. F. 1992, ApJ, 396, 469

Ivezić, Ž., Menou, K., Knapp, G. R., et al. 2002, AJ, 124, 2364

Ivezić, Ž., Kahn, S. M., Tyson, J. A., et al. 2019, ApJ, 873, 111

Jiang, Y.-F., Stone, J. M., & Davis, S. W. 2014, ApJ, 796, 106

Just, D. W., Brandt, W. N., Shemmer, O., et al. 2007, ApJ, 665, 1004

Kammoun, E. S., Dovčiak, M., Papadakis, I. E., Caballero-García, M. D., & Karas, V. 2021, ApJ, 907, 20

Kang, W.-y., Wang, J.-X., Cai, Z.-Y., et al. 2018, ApJ, 868, 58

Kara, E., Zoghbi, A., Marinucci, A., et al. 2015, MNRAS, 446, 737

Kasliwal, V. P., Vogeley, M. S., & Richards, G. T. 2015, MNRAS, 451, 4328

—. 2017, MNRAS, 470, 3027

Kato, S., Fukue, J., & Mineshige, S. 2008, Black-Hole Accretion Disks — Towards a New Paradigm —

Kelly, B. C. 2007, ApJ, 665, 1489

Kelly, B. C., Bechtold, J., & Siemiginowska, A. 2009, ApJ, 698, 895

Kelly, B. C., Becker, A. C., Sobolewska, M., Siemiginowska, A., & Uttley, P. 2014, ApJ, 788, 33

Kelly, B. C., Treu, T., Malkan, M., Pancoast, A., & Woo, J.-H. 2013, ApJ, 779, 187

Kerr, R. P. 1963, PhRvL, 11, 237

Kim, D.-W., Protopapas, P., Byun, Y.-I., et al. 2011, ApJ, 735, 68

Kimball, A. E., & Ivezić, Ž. 2008, AJ, 136, 684

King, A. R., Pringle, J. E., West, R. G., & Livio, M. 2004, MNRAS, 348, 111

Kokubo, M., Morokuma, T., Minezaki, T., et al. 2014, ApJ, 783, 46

Korista, K. T., & Goad, M. R. 2004, ApJ, 606, 749

Kozłowski, S., Kochanek, C. S., Stern, D., et al. 2010, ApJ, 716, 530

Kriss, G. A., Peterson, B. M., Crenshaw, D. M., & Zheng, W. 2000, ApJ, 535, 58

Krolik, J. H., Horne, K., Kallman, T. R., et al. 1991, ApJ, 371, 541

Kumari, N., Pal, M., Naik, S., et al. 2021, PASA, 38, e042

Law, N. M., Kulkarni, S. R., Dekany, R. G., et al. 2009, PASP, 121, 1395

Lawrence, A., & Papadakis, I. 1993, ApJL, 414, L85

Li, Y.-R., Wang, J.-M., & Ho, L. C. 2012, ApJ, 749, 187

Li, Z., McGreer, I. D., Wu, X.-B., Fan, X., & Yang, Q. 2018, ApJ, 861, 6

Lin, D.-B., Lu, Z.-J., Mu, H.-J., et al. 2016, MNRAS, 463, 245

Lira, P., Arévalo, P., Uttley, P., McHardy, I. M. M., & Videla, L. 2015, MNRAS, 454, 368

Liu, B. F., Mineshige, S., & Shibata, K. 2002, ApJL, 572, L173

Lohfink, A. M., Reynolds, C. S., Vasudevan, R., Mushotzky, R. F., & Miller, N. A. 2014, ApJ, 788, 10

Lu, K.-X., Huang, Y.-K., Zhang, Z.-X., et al. 2019, ApJ, 877, 23. https://doi.org/10.3847/1538-4357/ab16e8

Lusso, E., Comastri, A., Vignali, C., et al. 2010, A&A, 512, A34

Lyubarskii, Y. E. 1997, MNRAS, 292, 679

MacLeod, C. L., Ivezić, Ž., Kochanek, C. S., et al. 2010, ApJ, 721, 1014

MacLeod, C. L., Brooks, K., Ivezić, Ž., et al. 2011, ApJ, 728, 26

MacLeod, C. L., Ivezić, Ž., Sesar, B., et al. 2012, ApJ, 753, 106

Marconi, A., Risaliti, G., Gilli, R., et al. 2004, MNRAS, 351, 169

Masci, F. J., Laher, R. R., Rusholme, B., et al. 2019, PASP, 131, 018003

McHardy, I., & Czerny, B. 1987, Nature, 325, 696

McHardy, I. M., Koerding, E., Knigge, C., Uttley, P., & Fender, R. P. 2006, Nature, 444, 730

McHardy, I. M., Papadakis, I. E., Uttley, P., Mason, K. O., & Page, M. J. 2004, Nuclear Physics B Proceedings Supplements, 132, 122

McHardy, I. M., Cameron, D. T., Dwelly, T., et al. 2014, MNRAS, 444, 1469

McHardy, I. M., Connolly, S. D., Peterson, B. M., et al. 2016, Astronomische Nachrichten, 337, 500

Meusinger, H., Hinze, A., & de Hoon, A. 2011, A&A, 525, A37

Miller, K. A., & Stone, J. M. 2000, ApJ, 534, 398

Morales, A. M., Miller, J. M., Cackett, E. M., Reynolds, M. T., & Zoghbi, A. 2019, ApJ, 870, 54

Morganson, E., Burgett, W. S., Chambers, K. C., et al. 2014, ApJ, 784, 92

Mushotzky, R. F., Edelson, R., Baumgartner, W., & Gandhi, P. 2011, ApJL, 743, L12

Nandra, K., Clavel, J., Edelson, R. A., et al. 1998, ApJ, 505, 594

Noble, S. C., & Krolik, J. H. 2009, ApJ, 703, 964

Nowak, M. A. 2000, MNRAS, 318, 361

Pal, M., Dewangan, G. C., Connolly, S. D., & Misra, R. 2017, MNRAS, 466, 1777

Pal, M., & Naik, S. 2018, MNRAS, 474, 5351

Paltani, S., & Courvoisier, T. J. L. 1994, A&A, 291, 74

Parker, E. N. 1966, ApJ, 143, 32

Peterson, B. M. 1997, An Introduction to Active Galactic Nuclei

Peterson, B. M. 2001, in Advanced Lectures on the Starburst-AGN, ed. I. Aretxaga, D. Kunth, & R. Mújica, 3

Peterson, B. M., Wanders, I., Horne, K., et al. 1998, PASP, 110, 660

Phillipson, R. A., Boyd, P. T., Smale, A. P., & Vogeley, M. S. 2020, MNRAS, 497, 3418

Rakshit, S., & Stalin, C. S. 2017, ApJ, 842, 96

Rakshit, S., Stalin, C. S., & Kotilainen, J. 2020, VizieR Online Data Catalog, J/ApJS/249/17

Ramos Almeida, C., & Ricci, C. 2017, Nature Astronomy, 1, 679

Rau, A., Kulkarni, S. R., Law, N. M., et al. 2009, PASP, 121, 1334

Ross, N. P., Ford, K. E. S., Graham, M., et al. 2018, MNRAS, 480, 4468

Rothstein, D. M., & Lovelace, R. V. E. 2008, ApJ, 677, 1221

RóżaŃska, A., & Czerny, B. 2000, A&A, 360, 1170

Ruan, J. J., Anderson, S. F., MacLeod, C. L., et al. 2012, ApJ, 760, 51

Sakata, Y., Morokuma, T., Minezaki, T., et al. 2011, ApJ, 731, 50

Sánchez-Sáez, P., Lira, P., Mejía-Restrepo, J., et al. 2018, ApJ, 864, 87

Schmidt, K. B., Marshall, P. J., Rix, H.-W., et al. 2010, ApJ, 714, 1194

Schmidt, K. B., Rix, H.-W., Shields, J. C., et al. 2012, ApJ, 744, 147

Sesar, B., Svilković, D., Ivezić, Ž., et al. 2006, AJ, 131, 2801

Shakura, N. I., & Sunyaev, R. A. 1973, A&A, 24, 337

Shankar, F., Salucci, P., Granato, G. L., De Zotti, G., & Danese, L. 2004, MNRAS, 354, 1020

Shapiro, S. L., & Teukolsky, S. A. 1983, Journal of the British Astronomical Association, 93, 276

Shappee, B. J., Prieto, J. L., Grupe, D., et al. 2014, ApJ, 788, 48

Simm, T., Salvato, M., Saglia, R., et al. 2016, A&A, 585, A129

Small, T. A., & Blandford, R. D. 1992, MNRAS, 259, 725

Starkey, D., Horne, K., Fausnaugh, M. M., et al. 2017, ApJ, 835, 65

Stern, D., McKernan, B., Graham, M. J., et al. 2018, ApJ, 864, 27

Stirpe, G. M., Winge, C., Altieri, B., et al. 1994, ApJ, 425, 609

Stone, Z., Shen, Y., Burke, C. J., et al. 2022, MNRAS, 514, 164

—. 2023, MNRAS, 521, 836

Strateva, I. V., Brandt, W. N., Schneider, D. P., Vanden Berk, D. G., & Vignali, C. 2005, AJ, 130, 387

Sun, M., Xue, Y., Cai, Z., & Guo, H. 2018a, The Astrophysical Journal, 857, 86

Sun, M., Xue, Y., Trump, J. R., & Gu, W.-M. 2019, MNRAS, 482, 2788

Sun, M., Xue, Y., Brandt, W. N., et al. 2020a, ApJ, 891, 178

Sun, M., Xue, Y., Guo, H., et al. 2020b, ApJ, 902, 7

Sun, Y.-H., Wang, J.-X., Chen, X.-Y., & Zheng, Z.-Y. 2014, ApJ, 792, 54

Tachibana, Y., & Miller, A. A. 2018, PASP, 130, 128001

Thanjavur, K., Ivezić, Ž., Allam, S. S., et al. 2021, MNRAS, 505, 5941

Timmer, J., & König, M. 1995, A&A, 300, 707

Troyer, J., Starkey, D., Cackett, E. M., et al. 2016, MNRAS, 456, 4040

Ueda, Y., Akiyama, M., Hasinger, G., Miyaji, T., & Watson, M. G. 2014, ApJ, 786, 104

Ulrich, M.-H., Maraschi, L., & Urry, C. M. 1997, ARA&A, 35, 445

Urry, C. M., & Padovani, P. 1995, PASP, 107, 803

Uttley, P., Cackett, E. M., Fabian, A. C., Kara, E., & Wilkins, D. R. 2014, A&A Rv, 22, 72

Uttley, P., McHardy, I. M., & Papadakis, I. E. 2002, MNRAS, 332, 231

Vanden Berk, D., Wilhite, B., Kron, R., et al. 2004a, in American Astronomical Society Meeting Abstracts, Vol. 205, American Astronomical Society Meeting Abstracts, 120.02

Vanden Berk, D. E., Wilhite, B. C., Kron, R. G., et al. 2004b, ApJ, 601, 692

Vaughan, S., Edelson, R., Warwick, R. S., & Uttley, P. 2003, MNRAS, 345, 1271

Wamsteker, W., Rodriguez-Pascual, P., Wills, B. J., et al. 1990, ApJ, 354, 446

Webb, W., & Malkan, M. 2000, ApJ, 540, 652

Wilhite, B. C., Brunner, R. J., Grier, C. J., Schneider, D. P., & vanden Berk, D. E. 2008, MNRAS, 383, 1232

Wilhite, B. C., Vanden Berk, D. E., Kron, R. G., et al. 2005, ApJ, 633, 638

Wold, M., Brotherton, M. S., & Shang, Z. 2007, MNRAS, 375, 989

Yip, C. W., Connolly, A. J., Vanden Berk, D. E., et al. 2004, AJ, 128, 2603

Yu, Q., & Tremaine, S. 2002, MNRAS, 335, 965

Yuan, F., & Narayan, R. 2014, ARA&A, 52, 529

Zhu, F.-F., Wang, J.-X., Cai, Z.-Y., et al. 2018, ApJ, 860, 29

Zhu, S. F., & Xue, Y. Q. 2016, ApJ, 825, 56

Zoghbi, A., Cackett, E. M., Reynolds, C., et al. 2014, ApJ, 789, 56

Zu, Y., Kochanek, C. S., Kozłowski, S., & Udalski, A. 2013, ApJ, 765, 106

Zuo, W., Wu, X.-B., Liu, Y.-Q., & Jiao, C.-L. 2012, ApJ, 758, 104